

FB-2013-23

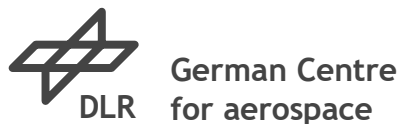
Investigations on signatures of planetary waves in the ionosphere

Dissertation for the award of the academic degree of
Doctor of Natural Sciences

Claudia Borries

German Aerospace Center Institute for
Communication and Navigation
Navigation Department, Ionospheric Effects and
Corrections Group

Neustrelitz
7 February 2014



Research Report 2013-23

Investigations on signatures of planetary waves in the ionosphere

Claudia Borries

German Aerospace Center Institute for
Communication and Navigation Neustrelitz

138 Pages
53 Images
0 Tables
137 References



German Centre
for aerospace

Investigations on signatures of planetary waves in the ionosphere

Dissertation
for the award of the academic degree of Doctor
of Natural Sciences
submitted by
Dipl.-Ing(FH) Claudia Borries

Free University of Berlin
Institute for Meteorology, Department of Earth Sciences
Berlin, 21 October 2010

Claudia Borries

German Aerospace Center (DLR) Institute of
Communications and Navigation
Kalkhorstweg 53, 17235 Neustrelitz, Federal Republic of Germany

Appraiser:

Prof. Dr. U. Langematz

Prof. Dr. Ch. Jacobi, Meteorological Institute, University of Leipzig Date

of disputation: 22 November 2010

Summary

The object of investigation are periodic variations of the electron density in the ionosphere, which are called planetary wave type oscillations (PWTO). They have periods between 2 and 30 days and a horizontal extension that can exceed 10,000 km. Due to their similarity to planetary waves (PW) of the lower and middle atmosphere, a connection with these is assumed. The present work deals with the investigation of the possible coupling between the lower atmosphere and the ionosphere by PW.

To describe the ionospheric PWTO, maps of the total electron content (TEC) of the ionosphere are used, which cover the northern hemisphere from 50° N to the polar cap and are operationally produced at DLR with an hourly resolution. The calculation of relative differences to the running 27-day median ($f_{j,T} EC_{rel}$) is used as a bandpass filter to minimise variations outside the periodic range of PW. In addition, a new filtering approach based on the wavelet transform is applied to minimise solar-driven variations in the $f_{j,T} EC_{rel}$ signal as best as possible. With the help of suitable analysis methods, the data set is spectrally decomposed into the wave components of the standing and travelling waves.

The comparison of the energy of the filtered signal $f_{j,T} EC_{rell,filter}$ and the relative TEC $f_{j,T} EC_{rel}$ shows a difference of up to 50%. This means that a large part of the energy of the PWTO in the ionosphere is generated by variations in solar radiation, the solar wind and associated geomagnetic disturbances. A significant dependence of PWTO activity on solar activity cannot be determined.

The spectral analysis of the $f_{j,T} EC_{rell,filter}$ shows both numerous similarities and clear differences in the characteristic properties of PWTO compared to PW. Particularly characteristic is the dominance of zonal mean variations and strongly pronounced PWTO with periods smaller than 10 days in the ionosphere. However, the differences shown do not exclude the connection to PW.

Some explanations for the coupling between the lower and middle atmosphere and the ionosphere are empirically examined in this paper. The results show that the non-linear interaction of atmospheric waves is a possible component of the coupling between the middle atmosphere and the ionosphere. The resulting secondary waves are assumed to reach the lower thermosphere, where they influence either the thermospheric composition or the winds and the dynamo-induced E-field, revealing their signatures in the ionosphere. In contrast, based on the results of the analysis, the influence of the modulation of atmospheric gravity waves on the coupling of the atmosphere-ionosphere system seems unlikely.

Abstract

Signatures of planetary waves in the electron density in the ionosphere (usually named planetary wave type oscillations, PWTO) are the object of investigation in this work. These PWTO are periodic variations with periods between 2 and 30 days and a horizontal extent which can exceed 10,000km. Because their properties often agree with atmospheric planetary waves (PW) in the lower and middle atmosphere, they are suggested to be related.

The PWTO are described on the basis of maps of the total electron content (TEC), which cover the northern hemisphere from 50° N to the polar cap and are operationally produced in the DLR with a temporal resolution of 1 hour. The calculation of relative differences to a running 27-day median ($f_{j,T} EC_{rel}$) is used as a band pass filter to avoid variations beyond the period range of PW. Appropriate spectral analysis methods are used to decompose the data set into the wave components of standing and propagating waves. Furthermore, a new filter method based on the wavelet transformation is used to minimize solar forced variations in the signal as good as possible.

The comparison of the power of the filtered signal $f_{j,T} EC_{rel,filter}$ and the relative TEC $f_{j,T} EC_{rel}$ shows a difference of up to 50%. Thus, a major part of the power of the PWTO in the ionosphere occur due to variations of the solar radiation, the solar wind and the corresponding geomagnetic perturbations. A significant correlation to the solar activity cycle cannot be found.

The spectral analyses of $f_{j,T} EC_{rel,filter}$ show a number of similarities as well as some differences in the characteristic properties of PWTO and PW. Quite characteristic is the dominance of the zonal mean oscillation and the strength of PWTO with periods below 10 days in the ionosphere. However, these differences do not exclude a correlation to PW.

A few suggestions for the coupling of the lower and middle atmosphere with the ionosphere mentioned in the literature are addressed empirically in this work. The achieved results indicate that the nonlinear interaction of atmospheric waves is a possible part of the mechanism coupling the atmosphere and ionosphere. It is assumed that the resulting secondary waves reach the lower thermosphere, where they influence the thermospheric composition or the winds and the dynamo induced electric field by what their signatures become visible in the ionosphere. Against this, the analysis results indicate that the modulation of atmospheric gravity waves is unlikely to take part in the coupling of the atmosphere and ionosphere.

Table of contents

1. Introduction	1
1.1. Subject of the work.....	1
1.2. Objectives of the present work.....	3
2. The Ionosphere-Thermosphere System	5
2.1. Introduction	5
2.2. The ionosphere	7
2.2.1. Origin and structure	7
2.2.2. Radio wave propagation in the ionosphere.....	8
2.2.3. The influence of the geomagnetic field.....	9
2.2.4. Influence of thermospheric dynamics.....	10
2.3. The thermosphere	11
2.3.1. Structure of the thermosphere	11
2.3.2. Thermospheric dynamics	11
2.3.3. Atmospheric waves	14
2.4. Coupling processes.....	16
2.4.1. Processes with solar origin.....	18
2.4.2. Internal coupling.....	19
2.4.3. Coupling to the lower and middle atmosphere.....	20
3. Planetary waves	23
3.1. Physics of planetary waves.....	23
3.2. Planetary waves in the stratosphere.....	25
3.3. Planetary waves in the mesosphere and lower thermosphere	28
3.4. Signatures of planetary waves in the ionosphere	29
3.5. The conditions for the propagation of planetary waves in the thermo- sphere	30
4. Data basis	33
4.1. Transitionospheric radiolin measurements	33
4.2. Global Navigation Satellite Systems (GNSS)	34
4.3. TEC calculation from GNSS measurements.....	35
4.4. TEC map creation	36
4.5. Comparison of different TEC maps.....	VII.....38

VIII Methods of analysis	43
5.1. Fourier analysis	43
5.1.1. Fourier spectrum	43
5.1.2. Correlation and cross spectrum.....	45
5.1.3. Amplitude modulation.....	46
5.1.4. Short-term Fourier analysis.....	46
5.1.5. Limitations of discrete Fourier analysis	48
5.2. Wavelet analysis.....	48
5.2.1. Continuous wavelet transform	49
5.2.2. Cross wavelet analysis and wavelet coherence	52
5.2.3. Inverse wavelet transform	52
5.2.4. Analogies and differences to short-term Fourier analysis	53
5.3. Frequency-wavenumber analysis.....	54
6. TEC variations with solar origin	57
6.1. Introduction.....	57
6.2. Parameters for describing the solar influence	57
6.3. Correlation between TEC and solar parameters	63
6.4. Estimation and filtering of the solar impact	66
6.5. Summary and discussion	71
7. Characteristic properties of planetary wave signatures in the ionosphere	73
7.1. Introduction.....	73
7.2. Properties of the signatures of planetary waves in the mid-latitudes	74
7.3. The latitudinal dependence of planetary wave signatures	81
7.4. Discussion of the influence of the geomagnetic field.....	84
7.5. Summary and discussion	87
8. Potential connections to stratospheric planetary waves	91
8.1. Introduction.....	91
8.2. Simultaneous activities in the stratosphere and ionosphere	91
8.3. Results of non-linear interaction	95
8.4. Modulating atmospheric gravity waves.....	101
8.5. Summary and discussion	110
9. Summary and outlook	115
List of figures	119

Table of contents

IX

Bibliography	123
Acknowledgement	137
A. FK spectra from stratospheric data	A
B. Analyses of the IGS-TEC maps	G

B.1. TEC variations with solar origin	G
B.2. Characteristic properties of planetary wave signatures in the ionosphere	J
B.3. Potential connections to stratospheric planetary waves ..	O

1. Introduction

1.1. Subject of the work

Although the climatology of the ionosphere is very well understood and can also be modelled successfully (*Rodger and Jarvis*, 2000), the reliable prediction of electron densities is not yet possible. In addition to the strong influence of the sun, meteorological influences from the troposphere and stratosphere also affect the variability of the ionosphere (*Forbes et al.*, 2000). Establishing a dynamic link between stratosphere and ionosphere is a difficult but also very important problem (*Rodger and Jarvis*, 2000), to which the present work is dedicated. The aim is to provide new insights into the dynamics of the ionosphere.

The present work deals with dynamic processes in the atmosphere which have a wave-like structure and global expansion, so-called planetary wave-like oscillations. The atmosphere, which can be divided into different layers based on its properties (density, temperature, pressure and charge) (see Figure 1.1), can be regarded as a large "wave carrier" (*Volland*, 1988), in which large-scale waves with different periods are generated. Some of these waves have a sufficiently large horizontal and vertical extension so that they are not destroyed by interference. These include planetary waves with periods between 2 and 30 days and wavelengths that can exceed 10,000km (*Volland*, 1988).

Planetary waves have been an interesting topic of research for some time. Their properties in the lower and middle atmosphere are widely known thanks to decades of research (e.g. *Charney and Drazin*, 1961; *Lindzen*, 1967; *Holton*, 1972; *Brown and John*, 1979; *Salby*, 1981; *Volland*, 1988; *Barnett and Labitzke*, 1990; *Labitzke and van Loon*, 1992). It is particularly interesting that the variability of the stratosphere in winter is essentially influenced by planetary waves. Descriptions of their propagation characteristics are derived from model studies (e.g. *Dickinson*, 1969; *Hunt*, 1984; *Langematz and Pawson*, 1992).

The effect of planetary waves in the upper atmosphere (from about 90km) is currently much discussed (e.g. *Meyer and Forbes*, 1997; *Laštovička and Sauli*, 1999; *Lawrence and Jarvis*, 2003; *Laštovička*, 2006). Because measured data of the neutral gas parameters are not available here, the

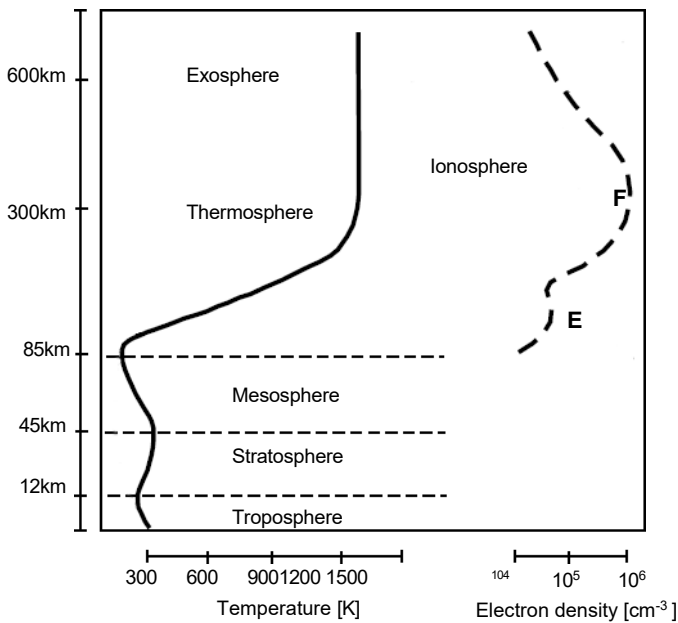


Figure 1.1: Temperature profile of the atmosphere (left) with an electron density profile of the ionosphere (right).

The dynamics of the upper atmosphere are only roughly known. However, due to its low air density, the upper atmosphere constantly contains free charge carriers that characterise the ionosphere. The state of the ionosphere can be determined very well by radiosounding. This advantage is to be used to investigate the possible influence of planetary waves on the upper atmosphere. The database of regional hemispheric TEC maps (see Chapter 4), which has been available since 2001, offers a new possibility to investigate ionospheric variability and thus to study the dynamics of the upper atmosphere.

The investigations in this work serve to improve our understanding of both the ionosphere and the neutral atmosphere. A current and important topic is the accurate prediction of the state of the ionosphere. This knowledge is particularly important for high-precision navigation and for safety-critical GNSS applications (e.g. in aviation). For the exploration of the neutral upper atmosphere, the results can be an important reference in comparison with modelling analyses. Recently, vertically coupled atmosphere-ionosphere models have been developed,

e.g. the Global Atmospheric Ionospheric Models (GAIM), one of which is operated at Logan University (USA) and one at the NASA Jet Propulsion Laboratory (JPL), or the Thermospheric Ionospheric Electrodynamics General Circulation Model (TIEG-CM) and the Thermosphere Ionosphere Mesosphere Electrodynamics General Circulation Model.

Model"(TIME-GCM), which are being developed by the National Center for Atmospheric Research High Altitude Observatory (USA).

The effect of planetary waves in the ionosphere has only recently been taken into account in the models. Systematic investigations of vertical coupling by planetary waves using the coupled atmosphere-ionosphere models are not known to date.

1.2. Objective of the present work

In the ionosphere, oscillations with horizontal and temporal scales of planetary waves (PW) are observed. Because the signatures of planetary waves are observed in a medium (electron densities) which cannot be the carrier of the waves, these oscillations are called PW-type oscillations (PWTO). The aim of this work is to contribute to the clarification of the origin of PWTO in the ionosphere.

PWTO have been detected in the past mainly by local measurements (e.g. ion probes or TEC measurements at single ground stations) (e.g. *Altadill*, 2000; *Altadill et al.*, 2001; *Pancheva et al.*, 2002; *Shalimov and Lapshin*, 2003; *Laštovička*, 2006; *Xiong et al.*, 2006). Regional ionospheric maps of DLR Neustrelitz showing the vertically integrated electron density (TEC) offer a new extended possibility for the analysis of PWTO. DLR's North Pole TEC maps, which extend from 50° N to the polar cap, should make it possible to determine characteristic properties of PWTO in the mid and high latitudes of the Northern Hemisphere. The occurring PWTO are to be broken down according to spatial scales and periodicities, and seasonal dependencies in the occurrence of PWTO are to be determined. The aim is to use the TEC maps to describe characteristic features of PWTO and to make statements about the contribution of PWTO to ionospheric variability.

It is known that the sun has a decisive influence on the variability of the upper atmosphere. Because the solar radiation arriving on Earth also varies in the time range between 2 and 30 days, it can be assumed that a large part of the ionospheric variability in the frequency range of PW can be explained by the influence of the sun. In order to understand the character and origin of the ionospheric PWTO and to estimate the influence of the atmospheric PW on the ionosphere, it is necessary to separate the ionospheric oscillations forced by the solar influence as precisely as possible. Therefore, in this work, correlations between solar variations with a periodic character and ionospheric variations are to be described and the solar-driven variations are to be separated from the other ionospheric variations in a suitable way.

variations can be separated.

The behaviour and climatology of PW are widely known from the troposphere to the stratosphere. Comparisons between observations of PW in the neutral atmosphere and PWTO in the ionosphere should show to what extent a connection between the two phenomena may exist. Looking at modelling studies that deal with the vertical propagation of PW, no direct correlation is to be expected. Therefore, possibilities for the indirect transport of PW energy into the ionosphere will be discussed in the further course of the work.

This paper is structured as follows: First, a general overview of the properties of the thermosphere-ionosphere system is given (Chapter 2), with a special focus on the variability of the upper atmosphere. Then, in chapter 3, the PW are described in their properties and their formation. The behaviour of PW is explained especially for the middle atmosphere and the transition to the thermosphere. Furthermore, the external conditions for PW in the thermosphere are explained and observations of PWTO in the ionosphere are compiled.

In chapter 4, the underlying database of the Total Electron Content (TEC) maps is explained in detail. First the calculation of the TEC from GNSS measurements and then the creation of the TEC maps is described. In the last section of the chapter, the special preparation of the data for the analysis of PW-like oscillations is explained. The methods of spectral analysis, which are widely used in signal decomposition and reconstruction in this thesis, are presented in chapter 5.

The results of the analysis are presented and discussed in chapters 6 to 8. First, the influence of the sun on the formation of PWTO is discussed and the solar-driven variations are separated from the PWTO (chapter 6). Then the typical occurrence of PWTO (excluding PWTO of solar origin) and their contribution to ionospheric variability is described (chap. 7). In comparison with neutral gas data, possible parallels between PW in the middle neutral atmosphere and PWTO in the ionosphere are sought. In addition, the difficult topic of coupling mechanisms and trans- port mechanisms for the transfer of PW energy into the ionosphere is addressed in Chap. 8. Current publications of PWTO observations and results from model studies are included in the discussion.

In the concluding chapter of the thesis (chapter 9), the results are summarised and an outlook on possible follow-up work is given.

2. The system Ionosphere-Thermosphere

2.1. Introduction

As shown in Fig. 2.1, the basic atmospheric variables density and pressure decrease exponentially with altitude. Up to an altitude of about 50km, 99.9% of the total mass of the atmosphere is already enclosed, and above 100km there is only about one millionth of the total atmospheric mass. Due to the low density, the particles rarely collide. The electrons and ions released by photoionisation at these altitudes do not immediately combine, allowing the number of free charge carriers to accumulate. While the thermosphere describes the behaviour of neutral particles, the ionosphere characterises the behaviour of charged particles.

The physical properties of the thermosphere and ionosphere are closely coupled, which is why we often speak of the ionosphere-thermosphere system. Phenomena observed in the ionosphere can often be attributed to processes in the thermosphere. In special situations, however, the plasma can also act on the neutral gas dynamics through ion friction, which means that iono-spherical phenomena can be reflected in thermospheric parameters. Ionospheric data are often used to gain information about neutral gas variability in the upper atmosphere. The reason is that the electron content of the ionosphere can be determined continuously and with global coverage using satellite measurement techniques (especially radiosondes with GNSS), whereas measurements of thermospheric state variables such as pressure, wind and temperature are only possible sporadically.

In this chapter, the properties of the ionosphere and the thermosphere are explained (sections 2.2 and 2.3) and the processes relevant for the coupling between ionosphere and thermosphere are described (section 2.4).

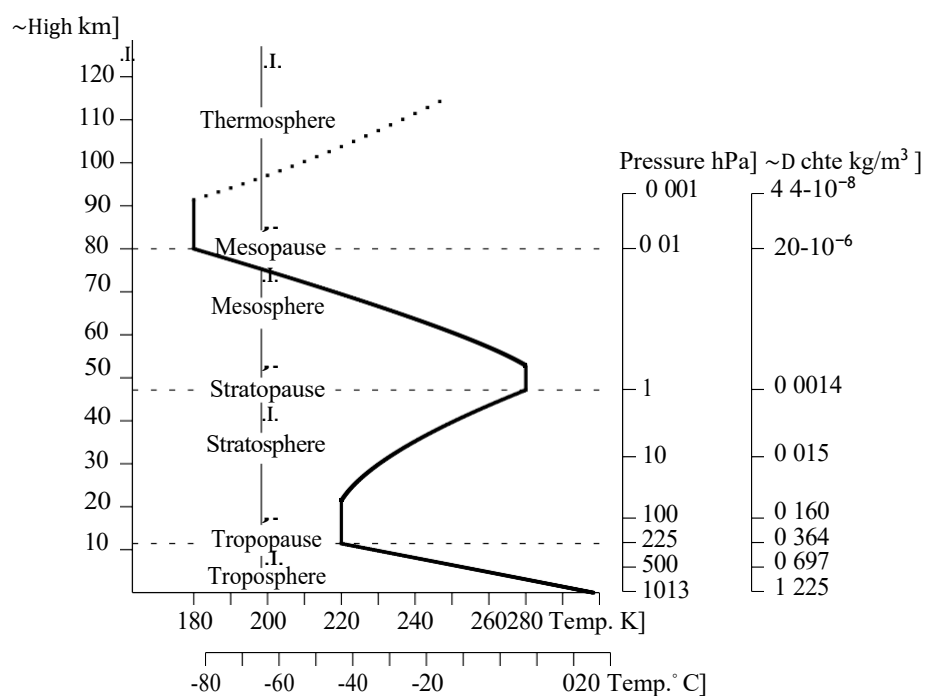


Figure 2.1: Temperature profile of the lower and middle atmosphere

2.2. The ionosphere

2.2.1. Origin and structure

The terms ionosphere and plasmasphere refer to the charged or ionised part of the atmosphere that is corotating with the earth. While in the ionosphere the proportion of plasma (charged particles) is greater than that of neutral gas, plasma predominates in the plasmasphere. The boundary layer between the ionosphere and the plasmasphere at a height of 1000km is fluid and varies greatly (depending on width and local time). The lower limit of the ionosphere results from the increased occurrence of ionised particles, which occurs at about 60km.

The charged particles characteristic of the ionosphere are produced by ionisation, i.e. the release of electrons from neutral molecules and atoms. This is mainly triggered by solar radiation influences, predominantly in electromagnetic form (extreme ultraviolet radiation, EUV, and X-rays) and as particle radiation. In addition, cosmic background radiation, charge exchange, secondary ionisation processes and meteorite flows also contribute to ionisation.

In general, the denser the atmosphere, the more energy is released into the surrounding matter and the greater the ionisation there. However, various factors prevent the total ionisation of the atmosphere: On the one hand, the energy release reduces the amount of energy available for ionisation in deeper layers, and on the other hand, various loss processes (dissociative recombination, radiation recombination and charge exchange) lead to a reduction in the electron density. Eq. 2.1 describes the *density balance equation* for a gas species s.

$$\frac{Bn_s}{Bt} = q_s - I_s + d_s \quad (2.1)$$

The temporal change of the electron density prevailing in a stationary volume element is not only determined by the production q_s and the loss I_s of the charged particles, but also by transport processes d_s , which can lead to both an increase and a decrease of the electron density (the sign of d_s can be positive or negative). With increasing altitude, the gas composition changes and

-density and thus the relationship between the production, loss and transport rates. Layers with different electron densities are created. The highest electron concentration is in the region between 200 and 400km, which is called the F-layer. Below the F-layer, between 60 and 90km altitude, there is the D-layer and between 90 and 120km altitude there is the E-layer. Although both layers are by far not as pronounced as the F layer, their effect on the total electron content (TEC) is nevertheless not negligible.

2.2.2. Radio wave propagation in the ionosphere

In principle, every electromagnetic wave undergoes changes in the direction of propagation, amplitude and speed when it passes through the ionosphere. The alternating effect between the radio wave and the ionosphere has an impact on the application of radio systems (interference or interruption of the signal), but it can also be used to obtain information. Conclusions about the properties of the ionosphere can be drawn from the type of changes observed, which is why radio waves are used as a diagnostic tool for researching the ionosphere. The type of interaction between the radio wave and the ionosphere depends on the frequency. The ionosphere causes the refraction of the radio signal on one occasion and the reflection of it on another. Two measurement methods make use of this property of the ionosphere. These are transionospheric radiolink measurement (see chapter 4.1 for further details) and echo sounding (radiosounding).

An essential parameter describing the influence of the ionosphere on radio signals is its refractive index n_{fon} , which in a first approximation is given by

$$n_{\text{fon}}(s) = 1 - \frac{K}{f_r^2} N_e(s) \quad (2.2)$$

can be described. Here f_r is the frequency of the radio signal, N_e the electron density and $K = 40.3 \text{ m}^3 \text{ s}^{-2}$ a constant that is composed of the charge of an electron, the dielectric permittivity in the vacuum and the electron mass. The refractive index varies with the electron density in the ionosphere and is therefore location-dependent. (s is the location vector). Because K , N_e , and f^2 are positive quantities, it can be deduced from Eq. 2.2.

The ionospheric refractive index is always less than 1. The refractive index smaller than 1 means that the phase velocity of the radio wave in the ionosphere $c_p = c/n_{\text{fon}}$ is greater than the velocity of light c . This frequency-dependent change in the phase velocity is used for transionospheric radiolink measurements, with which the total electron content along the beam path can be determined (see section 4.1). The group velocity $c_g = cn_{\text{fon}}$ is smaller than c .

Furthermore, according to the Snellius law, $n_{\text{fon}} < 1$ means that a radio wave incident obliquely on the ionosphere is refracted away from the perpendicular. If $KN_e(s)$ is 2: f^2 , then

$n_{\text{fon}}(s)$ is 0, and the wave is totally reflected. This principle is used for echo sounding, with which electron density profiles can be determined.

2.2.3. The influence of the geomagnetic field

The geomagnetic field, which is generated by electric currents inside the Earth (*Hargreaves*, 1992), has great significance for the movement of charged particles in the atmosphere. The simplest approximation for the geomagnetic field is an "axially centred dipole" (*Schunk and Nagy*, 2000), for which the magnetic axis coincides with the axis of rotation. In fact, however, the dipole axis is somewhat inclined and the magnetic poles are thus offset from the geographic poles. Because the air density decreases exponentially with altitude, the importance of the earth's magnetic field in the ionosphere increases. The region above 1000km altitude, where the degree of ionisation is high and the magnetic field dominates, is therefore called the magnetosphere.

The basic parameter for describing a magnetic field is the magnetic flux density a . It indicates at each location the magnitude and direction of the magnetic force exerted on a charge q moving at the velocity v

$$\mathbf{F}_L = q(\mathbf{v} \times \mathbf{B}) \quad (2.3)$$

The force F_L , generally referred to as the Lorenz force, thus causes a deflection of moving charge carriers in the magnetic field. In the ionosphere, it causes the charged particles to move preferably along the magnetic field lines as long as the frictional forces are small. In the lower ionosphere (E layer), where the particle density is relatively high, ion friction has a stronger effect than the Lorenz force. The electrons, which are much lighter than the ions, orient themselves to the magnetic field from an altitude of about 90 km. In contrast, the ions move with the neutral wind due to friction up to an altitude of 160km and only then orient themselves to the magnetic field. With a neutral wind perpendicular to the magnetic field, the electrons and ions move almost perpendicular to each other between 75 and 120km altitude. The relative movement generates an electric current and the separation of the charge an electric field E . The emergence of wind-induced currents can be understood as a *dynamo effect*.

During solar quiet times, the variations of the geomagnetic field are mainly determined by the solar (Sq) and lunar (L) flow systems of the dynamo region. The solar EUV radiation, which not only produces ionisation, heats the atmosphere and generates winds, also drives the Sq current. The main wind component contributing to this is the daily tide. Because the Sq current is generated by the diurnal variation of the sun, the associated geomagnetic variation moves westward (*Schunk and Nagy*, 2000). Naturally, solar variations are reflected in the Sq current, which shows strong seasonal variations and the typical 11-year solar cycle. The L-current is produced in a similar way to the Sq-current. The difference is that in this case the driving winds are determined by the semi-diurnal lunar tide. The L-current is an order of magnitude weaker than the Sq-current.

In addition to these regular variations, the geomagnetic field can also be disturbed by magnetospheric processes. The characteristic time scales associated with the perturbations range from minutes to days. Almost all of these perturbations can be attributed to the effects of solar wind variations on the magnetosphere. The strongest disturbances are called magnetic storms. The storm time variations are described by the Dst index (D(isturbance) st(orm)), which describes magnetic disturbances at low latitudes and is also a global measure of their intensity (Prölss, 2004). At high latitudes, the indices AE, AL and AU are used, which mainly describe the intensity of the polar jet stream. A measure of the variability of the magnetic field compared to the regular daily variation of the geomagnetic field is the Kp index. It is the most widely used geomagnetic index (Prölss, 2004).

2.2.4. Influence of thermospheric dynamics

The thermospheric parameters wind, density and temperature have a considerable influence on the electron density in the ionosphere. In summer, the thermosphere is heated significantly more than in winter. The rising temperature causes the gas to expand, which leads to a change in the molecular composition of the air in the thermosphere. The ratio of atomic to molecular oxygen ($[o/o_2]$), which essentially affects the ratio of production and loss processes in the F2 region, is lowered in summer, which leads to a reduction in electro-density through increased recombination. The increase in $[o/o_2]$ in winter increases the sensitivity of the ionosphere to solar radiation, resulting in the so-called winter anomaly. At the time of a winter anomaly, greater radio absorption (greater electron density) is found than would be predicted by simple interpolation of summer values (Jakowski and Paasch, 1984; Prölss, 2004; Hargreaves, 1992). In addition, the winter anomaly is characterised by very large variability in electron density. Over several days, the electron content can be abnormally high or low. On many days, the electron density is even higher in winter than in summer at midday. In the northern hemisphere, the winter anomaly typically occurs between November and February.

The difference in temperature between the summer and winter hemispheres, and the considered

Due to the resulting pressure differences, the thermospheric meridional winds are directed equatorward in summer and poleward in winter. Because the Coriolis force does not have such a dominant influence in the thermosphere as in the regions below, the zonal deflection of the winds is low. As already mentioned, meridional winds move the plasma along the magnetic field lines. Thus, the plasma rises in the summer hemisphere and sinks in the winter hemisphere. Because in larger

heights, the recombination is smaller due to the lower density, the total electron content of the ionosphere is increased in summer by the meridional winds and decreased in winter (*Forbes*, 2007).

2.3. The thermosphere

2.3.1. Structure of the thermosphere

Above the mesopause (from about 90km altitude), where the temperature rises extremely, the thermosphere begins. The temperature rises exponentially until it reaches an absolute maximum at about 300km and remains constant above this. The isothermal region, or the region in which the temperature asymptotically approaches the limit temperature, is usually called the thermopause. Unlike the plasma pause, for example, the thermopause cannot be related to a specific altitude. The thermosphere gets its name from its extremely high temperatures (700-1100K). At the solar maximum, up to 1300K can be reached in summer. These high temperatures are caused by the absorption of EUV and X-rays. This makes the lower thermosphere the layer of the atmosphere in which the temperature varies most with altitude.

The thermosphere is also the atmospheric layer where the greatest changes in gas composition occur. In the area between 110 and 500km (and beyond in the exosphere), a separation of gases by mass/density takes place, which is why this area is also called the heterosphere. At the bottom, the heavy gases predominate, while the lightest gases (such as hydrogen) dominate at the top. From 500km altitude, the density becomes so low that the collision becomes negligible and the upper atmosphere can no longer be considered a fluid. From there, the transition to the exosphere begins. The height of the transition varies with the activity cycle of the sun.

2.3.2. The thermospheric dynamics

Unlike in the lower regions of the atmosphere, there is no turbulence in the thermosphere because here the free path length is greater than the turbulent scale (*Hargreaves*, 1992). During geomagnetically quiet conditions, the dynamics of the upper atmosphere is mainly influenced by the Sun. On the dayside, there is a significant warming, which causes considerable differences in temperature and density between the

daytime and nighttime thermosphere (Prölss, 2004). The pressure gradients generate horizontal winds (thermospheric winds), which are often called "tidal winds" because of their 24-hour period (Prölss, 2004). The thermospheric wind blows horizontally from the warmed subpolar regions (day side) around the Earth to the coldest regions on the night side. Typically, the speed of the horizontal wind at 90-100km altitude averages 10m/s (Davies, 1996), with a larger tidal amplitude. At higher altitudes it is between 100 and 300m/s. However, the neutral wind in the thermosphere can also be caused by the energy input from particle infall in the aurora zone and Joule heating. During geomagnetically active periods, horizontal wind speeds of about 900m/s can be reached at the pole as a result.

According to Newton's first axiom, the speed of moving particles in the atmosphere remains constant as long as no force is acting on them. However, in a geocentric space-fixed coordinate system, no part of the atmosphere is at rest or in uniform motion due to the Earth's rotation. Acceleration must be taken into account. Newton's second axiom states that acceleration is described by the sum of all acting mass-specific forces.

$$\frac{d\mathbf{v}}{dt} = \frac{\mathbf{F}_J}{m} \quad (2.4)$$

An atmospheric particle in the inertial system is acted upon by the pressure gradient force $\frac{\partial p}{\partial r}$, the Earth's gravitational force $\mathbf{F}_g = m\mathbf{g}$, the viscosity¹ $\eta = \frac{C}{V}$ (vertical wind shear of a purely horizontal flow; v_h is the horizontal wind speed) and frictional forces (Prölss, 2004; Holton, 1972). Unlike in the middle atmosphere, where frictional forces can be neglected in a first approximation, the in the upper atmosphere, the ion friction $\frac{1}{2}C_{nlf}V^2$ (ion drag, V^* is the friction frequency between neutral gas particles and ions, v is the wind speed and v_f is the speed of the ions) must be taken into account as a friction force. In the inertial system, this results in the equation of motion:

$$\frac{d\mathbf{v}}{dt} = -\frac{1}{m}\mathbf{p} + \frac{1}{m}\frac{\mathbf{B}^2\mathbf{v}}{V^*} - C_{nlf}V^*(\mathbf{v} - \mathbf{v}_f) \quad (2.5)$$

In a system rotating with the earth (angular velocity \mathbf{Q}) additional inertial forces (apparent forces) act on moving particles. These are the coriolis force $\mathbf{F}_c = 2\mathbf{m}\mathbf{Q} \times \mathbf{v}$ and the centrifugal force $\mathbf{F}_z = m\mathbf{Q}^2\mathbf{r}$ ($\mathbf{Q} = m\mathbf{Q}^2\mathbf{R}$ is the vector of the distance to the axis of rotation). The acceleration due to change of the

Earth rotation $\frac{d\mathbf{v}}{dt}$ is very small and will be neglected here. The equation of motion

¹Coefficient of viscosity: $\eta = 1.7 \times 10^{-5}$ kgm⁻¹s⁻¹ (for 300km altitude)

in the rotating system is therefore

$$\frac{d\mathbf{v}}{dt} = \frac{d\mathbf{v}}{dt} - \mathbf{Q} - \frac{\mathbf{Q}^2 \mathbf{R}}{dt} \quad (2.6)$$

The centrifugal acceleration is usually combined with the mass acceleration to form an effective acceleration $= \mathbf{m} + \mathbf{Q}^2 \mathbf{R}$

A scale analysis shows that the horizontal movement is essentially determined by the pressure gradient force and the ion friction. Therefore, the wind flow at 300km altitude follows the respective pressure gradients in a good approximation, which is why we speak of so-called "barospheric" winds (Prölss, 2004). Ion friction has a great effect on the thermospheric winds. During the day, when ion friction is high, the wind speed is reduced to about 50m/s, while at night, when ion friction is low, wind speeds of about 300m/s are reached (Davies, 1996). However, ion friction can also act as an acceleration force. This case occurs in the polar high atmosphere, where intense electric fields can accelerate the ions to high speeds. Part of this kinetic energy is transferred to the neutral gas via impact friction, which can result in considerable wind speeds ($> 1000\text{m/s}$) (Prölss, 2004).

In the thermosphere, the pressure gradient force and the ion friction are almost equally weighted. The Coriolis force, which deflects the wind in the lower regions, is small here compared to the ion friction and thus plays a subordinate role in the dynamics of the thermosphere (Forbes, 2007).

The observation of the scale analysis shows that the vertical movement is dominated by the vertically acting forces pressure gradient force and gravity. This also allows in the thermosphere, the basic hydrostatic equation $\frac{dp}{dz} = -\rho g$ is valid-be taken.

Atmospheric movements are determined by three basic laws: conservation of momentum, conservation of mass and conservation of energy. The conservation of momentum has already been described with the equation of motion (Eq. 2.6). The mathematical relationship describing the conservation of mass is the continuity equation

$$\frac{\partial p}{\partial t} + \mathbf{V} \cdot (\mathbf{p} \cdot \mathbf{v}) = 0. \quad (2.7)$$

The first law of thermodynamics², which describes the change in internal energy as the sum of the added heat and the work done, leads to the third basic law, the thermodynamic law of conservation of energy (Schunk and Nagy, 2000; Prölss, 2004) for adiabatic flows:

$$\frac{dp}{dt} + p \cdot \mathbf{V} \cdot \mathbf{v} = 0. \quad (2.8)$$

²The first law of thermodynamics applies in a system that is inertially at rest and returns to rest after exchanging heat with the environment and performing work.

is the ratio of the specific heat capacities at constant pressure c_p and constant volume c_v . Inserting the continuity equation $\frac{1}{V} \frac{dp}{dt}$ gives the law of conservation of energy becomes

$$\frac{1}{p} \frac{dp}{dt} - \frac{1}{V} \frac{dp}{dt} = 0.$$

$\frac{dp}{dt}$

2.3.3. Atmospheric waves

Waves are a common phenomenon in the atmosphere. They are of great importance in meteorology because they are carriers of physical properties such as energy and momentum. In the high atmosphere, waves can cause significant interactions between the neutral atmosphere and the ionosphere (Hargreaves, 1992).

In general, a wave is described by the following wave equation for plane harmonic waves.

$$x(t) = A \cos(\omega t + \phi) \quad (2.9)$$

Here x is the location vector, t the time and A the amplitude of the wave, which describes the maximum deviation of a quantity x from its background value caused by the wave. From the angular frequency ω , which determines the period T , and the wave vector

k , which describes the wavelength and the direction of propagation, the phase relationship can be calculated.

$$c = \omega / k \approx Aw / 1r.$$

There are two possible causes for atmospheric waves. Firstly, periodically varying forces can excite oscillations (forced oscillations, e.g. tides). The period of these oscillations is determined by the periods of the exciting force. Secondly, aperiodic forces (e.g. a single impulse) can trigger the natural oscillation of a system capable of oscillation. The occurring periods are then characteristics of the oscillating system.

The triggers of the natural oscillations of the atmosphere are often regarded as disturbances of the atmospheric state variables (Laplace's disturbance theory). Depending on the horizontal extent of the disturbance, other restoring forces dominate. The basic three restoring forces in the Earth's atmosphere are gravity, the compression force and the "B" effect³. Based on the forces at work, different types of waves can be distinguished (see Figure 2.2). The three basic forms of atmospheric waves are gravity waves, planetary waves (also called Rossby waves) and sound waves. In each case, only one of the three repulsive forces is effective.

³Apparent force caused by the variation of the Coriolis force with latitude.

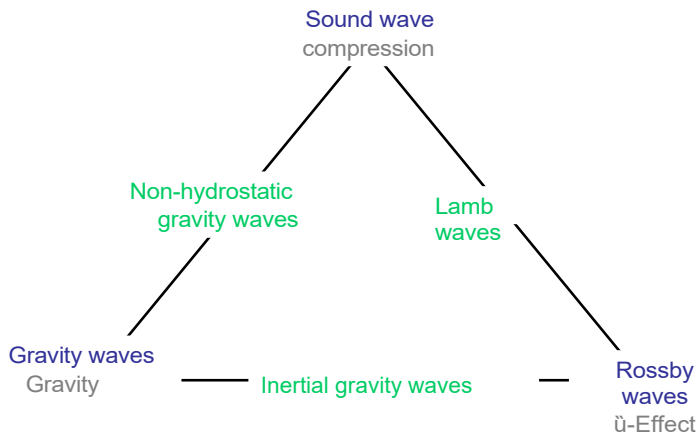


Figure 2.2: This wave triangle shows the three basic types of atmospheric waves and their mixed forms.

The wave type with the largest scales, both in the space and time dimensions, are the planetary waves. Due to their large scales, the Coriolis force acts, which can be neglected for smaller scales. Since the Coriolis force is an apparent force caused by the Earth's rotation, it is clear that planetary waves can only arise in a rotating system. They are excited, for example, by orography (large mountain ranges) or thermal differences (land-sea distribution).

On a smaller scale are the atmospheric gravity waves (AGW), which are caused by the buoyancy forces of the atmosphere. They can be divided into external and internal AGW, whereby the external AGW, which can only propagate horizontally along a boundary layer, play a minor role in the atmosphere. In contrast, internal gravity waves, which propagate within a medium, are a common phenomenon in the atmosphere. Their phase propagation points obliquely upwards (Prölss, 2004). AGW usually have a localisable source and move in a limited range of wavelength. Triggers are often in-stabilities at the flanks of jet streams (e.g. due to the overflow of mountains), fronts, convection, mesoscale eddies and geostrophic adjustment. Volcanic eruptions and earthquakes can also stimulate AGW. In the upper atmosphere, AGW can result from variations in Joule and particle heating rates, the Lorenz force at high latitudes, the breaking of upwelling tides and the movement of the solar terminator (Schunk and Nagy, 2000).

As the third basic form of atmospheric waves, sound waves have the smallest spatial scale. Sound waves are only of secondary importance for the dynamics or energy of the upper atmosphere (Schunk and Nagy, 2000) and are therefore not explained in detail here. In addition to the three fundamental wave types, mixed

forms, such as the non-hydrostatic gravity waves, the Lamb waves and the inertial gravity waves, if two of the repulsive forces dominate in each case (see Fig. 2.2). The tides as forced atmospheric oscillations can be triggered either by the gravitational and centrifugal forces (lunar tides), or by thermal changes (solar tides) (Schunk and Nagy, 2000). Tidal disturbances that move westward on the rotating Earth in a stationary system (sun-synchronous) are called migratory tides. The migrating tides include the diurnal tide (DT) with wave number 1 (its wavelength corresponds to the circumference of the earth) and a period length of one day, the semi-diurnal tide (DT) with wave number 2 (its wavelength corresponds to the circumference of the earth) and a period length of one day, semi-diurnal tide (SDT) with a 12-hour period and wavenumber 2 (its wavelength is half the circumference of the Earth) and the 8-hour tide (TDT) with wavenumber 3. Non-migratory tides have the same periods but different wavenumbers. The amplitude of the lunar tide is small compared to the solar tides (about one fifth).

Tides in the thermosphere either originate from tides rising from the mesosphere/lower thermosphere or arise in situ from the absorption of UV and EUV radiation (Schunk and Nagy, 2000). In general, the daily tide dominates in the thermosphere. An exception is the region between 90 and 100km altitude, where the semi-diurnal tide dominates at mid-latitudes (Laštovička, 1997). Between 100 and 250km altitude, both the daily and the semi-diurnal tide are present. Above that, from an altitude of 250km, only the diurnal tide is present.

2.4. Coupling processes

The electrodynamic coupling between the thermosphere, ionosphere and magnetosphere plays a decisive role in the behaviour of the entire system. The most important coupling processes have already been mentioned in the previous two sections (2.2 and 2.3) and will be described in more detail in this chapter. An overview of the extensive coupling processes is shown in Fig.2.3. It shows how the various ionospheric/thermospheric phenomena and their driving forces, winds, waves and electric fields are related to geomagnetically quiet and disturbed conditions (based on Fig. 2 in Abdu *et al.*, 2006). Basically, three types of coupling processes (Laštovička, 1997) can be distinguished. These are firstly processes with solar origin, secondly the interaction between ionised and neutral components and thirdly the influence of atmospheric waves such as PW, AGW and tides. These three types of coupling are described in the eng-

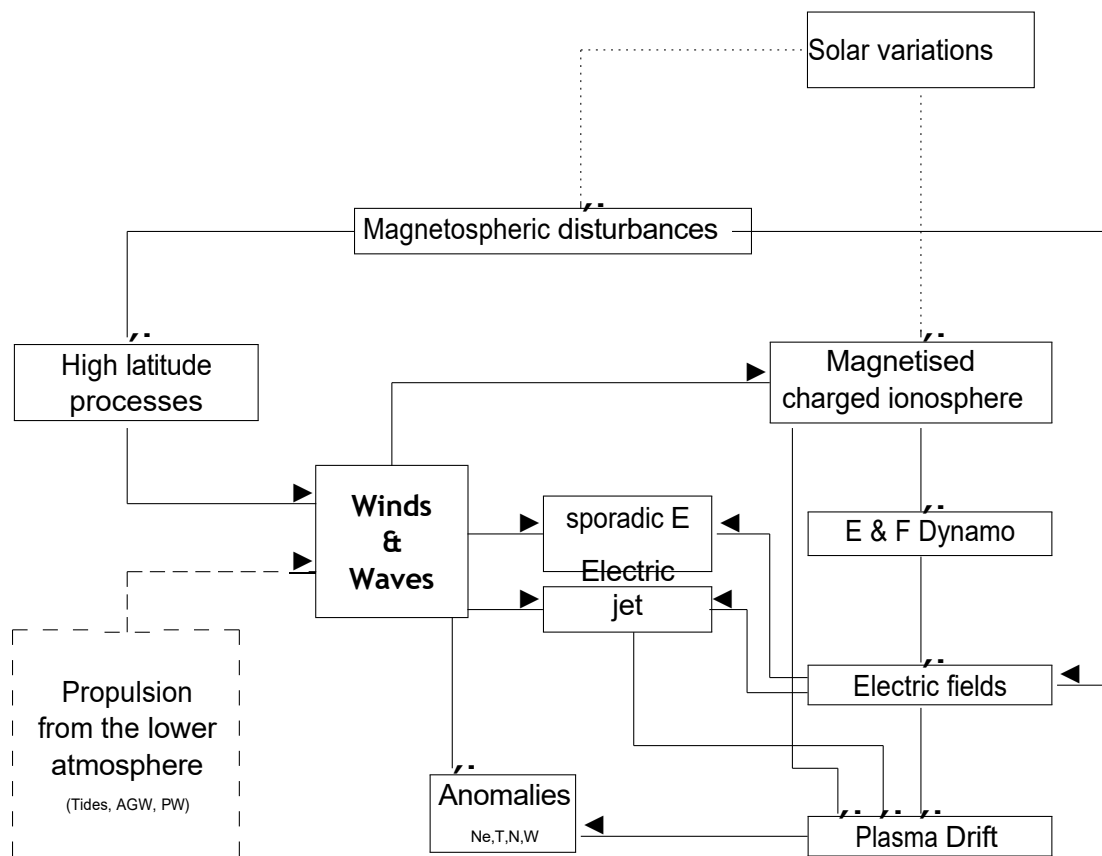


Figure 2.3: Block diagram of the coupling processes in the ionosphere-thermosphere system (based on Fig. 2 in *Abdu et al.*, 2006). Dotted lines: "Coupling from above"; solid lines: "Internal coupling"; dashed lines: "Coupling from below".

The three types of coupling are often referred to as "coupling from above", "internal coupling" and "coupling from below". The three different types of coupling are marked by different lines in Fig. 2.3.

2.4.1. Processes with solar origin

In contrast to the lower atmosphere, the ionosphere-thermosphere system is an externally controlled deterministic system in which dynamic structures are strongly suppressed by molecular diffusion (Forbes, 2007). The decisive influence of solar radiation on the electron densities in the ionosphere has already been discussed in Sect.

2.2.1 described above. The varying radiation intensity of the sun and the earth's movement cause variations in the upper atmosphere on different time scales. The rotation of the Earth leads to local changes in the radiation intensity, which create a daily tide in the electron densities. A significant quasi 27-day period arises from solar rotation and a different length distribution of the emission centres of EUV, X-ray and radio radiation (activity centres) on the Sun. The radiation intensity reaching the Earth thus varies quasi-periodically and produces a variation of the electron density with the same period (27 days). Depending on the position of the activity centres, different partial oscillations (harmonics) of the 27-day period can arise, such as the 13.5-day or the 9-day period. Furthermore, a seasonal cycle is formed by the eccentricity of the Earth's orbit and the inclination of the ecliptic. A common parameter for the quantitative description of the solar activity is the 10.7cm radio flux index (called F10.7 in the further course of the work). The observation of the F10.7 shows a clearly pronounced variation of the solar activity in an 11-year rhythm, which is called the "Schwabe cycle" or "solar activity cycle". There are times when the Sun's activity centres occur only rarely or in a weakly pronounced form. Under these conditions, the sun is called quiet. An active sun, on the other hand, is characterised by numerous, intensive and extensive activity centres (Prölss, 2004).

Because photoionisation depends on the angle of incidence of the solar radiation, there is a latitudinal dependence of ionisation. Consequently, the electron density is significantly higher near the equator than in the polar regions.

Not to be neglected is the influence of the solar wind, which is particularly strong at high latitudes, where the ionosphere is electrically connected to the nightside magnetosphere (about 10-100 Earth radii) by strongly conducting magnetic field lines. When the Bz component (northward component) of the interplanetary magnetic field (IMF) in the solar wind is negative, the magnetic field lines of the IMF and the geomagnetic field connect and energy from the solar wind is carried into the magnetosphere along the magnetic field lines. A plasma is formed in the magnetosphere.

Convection system that maps along the field lines into the ionosphere (at high latitudes). The internal coupling (Airdrag see section 2.4.2) sets the neutral atmosphere in motion (Forbes, 2007).

With a negative B_z component of the IMF, energetic particles can reach the thermosphere along the field lines in the high latitudes, where they cause changes in the electron density. On the one hand, the loss term I_s is changed by the heating of the thermosphere and the associated changes in composition (see section 2.2.4) and, on the other hand, the production term q_s (Eq. 2.1) is increased by particle precipitation.

Particularly strong effects can be observed during geomagnetic storms, which are associated with a strong particle incidence. Due to the strong heating of the thermosphere, significant compositional changes take place, which lead to a reduction of the electron densities. As a result, the ionisation remains reduced for several days after a geomagnetic storm.

During geomagnetic storms there are also strong changes in the thermospheric wind, which in turn drives the S_q current (see section 2.2.3). By changing the S_q current, solar variations can be reflected in the variation of the geomagnetic field. The geomagnetic field modulated by the solar signal acts as a mediator on ionisation by influencing the movement of ionised particles (see section 2.2.3). It thus modifies the electric currents and the overall motion of the plasma (Hargreaves, 1992). The strong correlation between the solar variation and the variation of the geomagnetic field can be seen in the high correlation of the 27-day period in $F_{10.7}$ and in the geomagnetic perturbations (e.g. visible in the A_p index). The solar activity cycle can also be observed in the geomagnetic activity. However, the correlation is not as high as is often assumed (Hargreaves, 1992).

2.4.2. Internal coupling

In principle, the motion of the charged and neutral particles is dominated by different forces. Nevertheless, both interact by collision. In the lower region of the ionosphere (D, E, F1 layer, 70-160km), the air density $p = n_n m$ and collision frequency V_{fn} are so great that, due to ion friction, the plasma motion is determined by the neutral gas motion. The ion friction force is represented as follows:

$$F_{nf} = n_n m V_{nf} (u_f - u_m). \quad (2.10)$$

In addition to the air density and collision frequency, the ionic frictional force F_{nf} per unit volume is also determined by the difference between the velocities of ions and neutral particles.

(u_f and u_n) (*Volland*, 1988). The indices n and i belong to neutral gas particles and ions. The mass m is assumed to be the same for both types.

Due to the much smaller surface area of the electrons, the ionic friction force does not act as strongly on them as on the ions. This results in a separation of the charge carriers, which creates electric fields and currents in the dynamo region. The interaction between plasma and neutral gas and the additional effect of the net field leads to more complicated width-dependent processes in the dynamo region. This includes, for example, the fountain effect near the equator.

In the F2 layer (from 200km), the collision frequency is lower (but still significant), so that the neutral wind cannot move the ions across the magnetic field lines. The ions stick to the magnetic field lines like rings on a stick. They can easily move along them but cannot cross them. The vertical angle between the neutral wind, which blows mostly horizontally, and the magnetic field lines, which are nearly horizontal at the equator and nearly vertical at the pole, determines that at mid-latitudes an equatorward wind raises the plasma, while a poleward wind lowers it. Because the recombination rate decreases with altitude, the equatorward winds increase the electron density, while the poleward winds reduce it.

The ions can also transfer motion to the neutral gas (Airdrag). The air-drag force is correspondingly (*Volland*, 1988):

$$F_{fn} = n_f m V_{fn} (u_n - u_f) \quad (2.11)$$

However, the transfer of the plasma motion to the neutral gas is more difficult and takes longer (than vice versa) because of the low density of the plasma. The collision between electrons and neutral particles can be neglected when considering the thermosphere dynamics because of the low mass of the electrons.

2.4.3. Coupling to the lower and middle atmosphere

As explained in section 2.2.4, the thermospheric parameters of temperature, wind and pressure affect the degree of ionisation. Because the dynamics of the thermosphere are partly related to the lower and middle atmosphere, it is not surprising that changes in ionospheric parameters are correlated with changes in the lower atmosphere (*Hargreaves*, 1992). Coupling mechanisms between the middle atmosphere and the thermosphere-ionosphere system can be atmospheric waves, such as the tides, AGW and PW. Upward-moving waves can affect the thermospheric wind, resulting in their properties being reflected in electric fields and currents, or they can cause changes in thermospheric density or composition, which are reflected in the electron density of the thermosphere.

reflect.

Atmospheric tides are mainly thermal tides that result from the periodic heating of the sun. In the thermosphere up to approx. 160km altitude, where the semi-diurnal tide dominates in mid-latitudes, the phase and amplitude of the tide are altitude-dependent in winter. Above about 200km, however, the phase and amplitude of the daily tide dominating there are quasi-constant with altitude (*Laštovička*, 1997). The variability of the amplitude of this wave is significantly lower than that of the daily tide in the mesosphere/lower thermosphere, suggesting that the two waves have little in common.

AGW can also propagate into the thermosphere. Their detection in the thermosphere is mostly done via their ionospheric signature, which is called "Travelling Ionospheric Disturbances" (TID).

PWs mainly originate in the troposphere. In winter, they can rise directly up to about 110 km. Their effects have been detected in the lower ionosphere (e.g., *Laštovička*, 2001) and the E layer (e.g., *Brown and John*, 1979). Periods of PW can also be observed in the geomagnetic S_q flow (*Laštovička*, 1997, references therein).

Due to changes in the thermospheric composition, the electro- nal content of the ionosphere varies more in winter than in summer (winter anomaly, see section 2.2.4). The disturbances observed during the winter anomaly have an extension of several thousand kilometres and do not repeat from one year to the next. These characteristics of the anomaly suggest meteorological components such as the influence of PW as its cause. To date, however, no evidence has been found either for or against the ionosphere winter anomaly being related to the mesosphere and stratosphere (and their dynamics).

Knowledge of the effect of rising waves is not only very important for understanding the vertical coupling of the atmosphere, but also for the energy budget of the ionosphere, the ionospheric dynamics and the prediction of the ionospheric state.

3. Planetary waves

3.1. Physics of planetary waves

It is known that planetary waves (PW) are large-scale (global) oscillations of the atmosphere. Their periods last several days and their wavelengths are several 1000km. As early as 1939, Carl Gustav Rossby mathematically proved the existence and displacement of PW, which is why PW in the mid-latitudes are also called Rossby waves.

PW are horizontal-transverse waves that originate primarily in the troposphere. They are often triggered by thermal contrasts caused by land-sea differences, the orography or the thermal activity of the tropics (e.g. Salby, 1984). Different types of PW occur due to different geographical and climatic conditions (e.g. the Kelvin and Rossby gravity waves near the equator and the Rossby waves in the mid-latitudes). The decisive factor for the development of PW is a disturbance of the wind system in meridional direction, on which the ,B-effect, i.e. the latitude-dependent variation of the Coriolis force acts as a restoring force. The dispersion equation of PW can be derived from the linearised barotropic vorticity equation under the assumption of a frictionless, incompressible medium, a purely horizontal shear-free flow and a disturbance in the N-S direction.

$$\frac{dq}{dt} = \left(\frac{B}{Bt} + u \frac{B}{Bx} + v \frac{B}{By} \right) (+, Bv = 0) \quad (3.1)$$

The barotropic vorticity equation (Eq. 3.1) states that the vertical component of the absolute vorticity q is maintained during horizontal movement. The absolute vorticity $q = (+ f$ is composed of the relative vorticity $(= B_x v - B_y u$, with the zonal and meridional wind components u and v , and the Coriolis parameter f (=planetary vorticity, depending on the latitude). x and y describe the zonal and meridional direction. $B = df / dy$ is the planetary vorticity gradient at the corresponding latitude.

Now it is assumed that each movement consists of an equilibrium value, a deflection of magnitude a and a small disturbance $E = a(a^2)$, where a

is small. I.e. that $u = u_- + u^I + E$, $v = v^I + E$ and $(= B_x v^I - B_y u^I + E = C^I + E$. Following a current function of the disturbance is defined with $u^I = B_y -^I$ and $v^I = B_x -^I$, so that $(^I = ^I \nabla$. The linearised perturbation approach of 3.1, where all terms of magnitude a^2 are neglected, is thus

$$\left(\frac{B}{B_0} + u_- - \frac{B}{B_0} \right) V^2 + ,B \frac{B -^I}{B_0} = 0 \quad (3.2)$$

If we now assume that the Brunt-Väisälä frequency N , the Coriolis parameter f and the planetary vorticity gradient $,B$ are constant (approximation on the $,B$ plane) and the solution is periodic with $p = A^{f.. x+iy-t}$, then the following dispersion relation for PW can be derived:

$$(k^2 + I^2)(w - k u_-) + k, B = 0. \quad (3.3)$$

Here k and I are the wave numbers in the zonal and meridional direction, and w is the angular velocity of the wave. The dispersion relation can be transformed so that the phase velocity $c = w/k$ can easily be read off.

$$c = \frac{w}{k} = u_- - \frac{,B}{k^2 + I^2} \quad (3.4)$$

This equation, generally referred to as the Rossby formula, can only roughly or approximately reflect the real atmospheric conditions because of the extensive simplification in the derivation. Nevertheless, it shows that the jet streams of the stratosphere are of great importance for the formation of PW (Holton, 1972). They reach their maximum wind speed at an altitude of about 60km. Rossby's equation (Eq. 3.4) shows that stationary PW with $c = 0$ arise when $u_- = u_s = \frac{f^2}{,B}$. PW propagate eastwards for $u_- < u_s$ and westwards for $u_- > u_s$.

Charney and Drazin (1961) have established a criterion for the vertical ascent of PW:

$$0 \leq u_- - c \leq u_c = ,B / (k^2 + I^2) + (f^2 / 4H^2 N^2) \quad (3.5)$$

This so-called Charney-Drazin criterion states that vertical propagation of PW is only possible if the phase velocity relative to the zonal base flow ($c - u_- = ,B / (k^2 + I^2)$) is westward and smaller than a critical value u_c (for $u_- = \text{const}(z, y)$, with scale height H). Forced stationary waves ($c = 0$) can therefore only propagate vertically with eastward flow. East winds thus hinder the development and rise of PW, whereas west winds support the rise of PW. However, excessively strong winds can also prevent ascent if $u_- - c$ becomes greater than u_c . Equation 3.5 also shows that the "window" for vertical propagation of waves becomes smaller with shorter wavelengths. Since easterly winds prevail in summer and westerly winds only in winter, PW ascent is only possible in winter and especially for particularly large waves (with small wavenumbers).

The migrating PW are large-scale, very slowly moving waves that can often be observed in the meteorological maps as meanders in the jet streams. In section 2.3.3 it was described that the PW belong to the natural oscillations of the atmosphere. Primarily, their period lengths are approx. 2, 5, 10 and 16 days, due to the natural frequencies of the atmosphere. The periods mentioned are all quasi-periods because the periods of the PW actually vary around these values. They therefore develop period bands (*Laštovička*, 1997). Since the PWs depend on the mean zonal wind (see Eq. 3.4), which changes with the seasons, the periods of the PWs have to be considered differentiated by seasons. The periods are also influenced by spatial variations of the zonal wind (*Salby*, 1981).

A good description of the global activity of PW can be found in *Barnett and Labitzke* (1990). According to this, the largest wave amplitudes occur in winter between 60-70° N or S, while they are small all year round in the tropics. On climatological average, the amplitudes of the forced stationary waves are larger than the free travelling waves. While migrating waves in the tropics (e.g. Kelvin waves) are excited all year round, they mainly occur in winter in the mid-latitudes. The high activity of PW in the mid-latitudes is of great importance for the overall weather development there, because ultimately the circulation in the mid-latitudes is the result of a superposition of numerous different PW. Figure 3.1 shows a schematic of PW activity in the Earth's atmosphere. Observations and analysis results on PW in the stratosphere, the mesosphere/lower thermosphere and the ionosphere-thermosphere system are discussed in the following sections.

3.2. Planetary waves in the stratosphere

Charney and Drazin were the first to identify upwardly rising PW as an important component of stratospheric dynamics (*Lindzen*, 1990). In the vertical propagation of PW from the troposphere into the stratosphere, their amplitudes grow approximately inversely proportional to the square of the air density. The amplitudes of PW are generally greatest in the stratosphere and lower mesosphere (*Barnett and Labitzke*, 1990).

PWs predominant in the stratosphere are vertically moving quasi-stationary PWs (SPW). The SPW usually signify a displacement or deformation of the polar vortex. In the previous section it was shown that the vertical motion of SPW depends not only on the zonal wind but also on the horizontal extension of the wave. Of the SPW, therefore, only those with small wave numbers ($k = 1$ and $k = \lambda$) can rise significantly from the troposphere into the stratosphere.

The SPW tend to move upwards and towards the equator. Move zonally

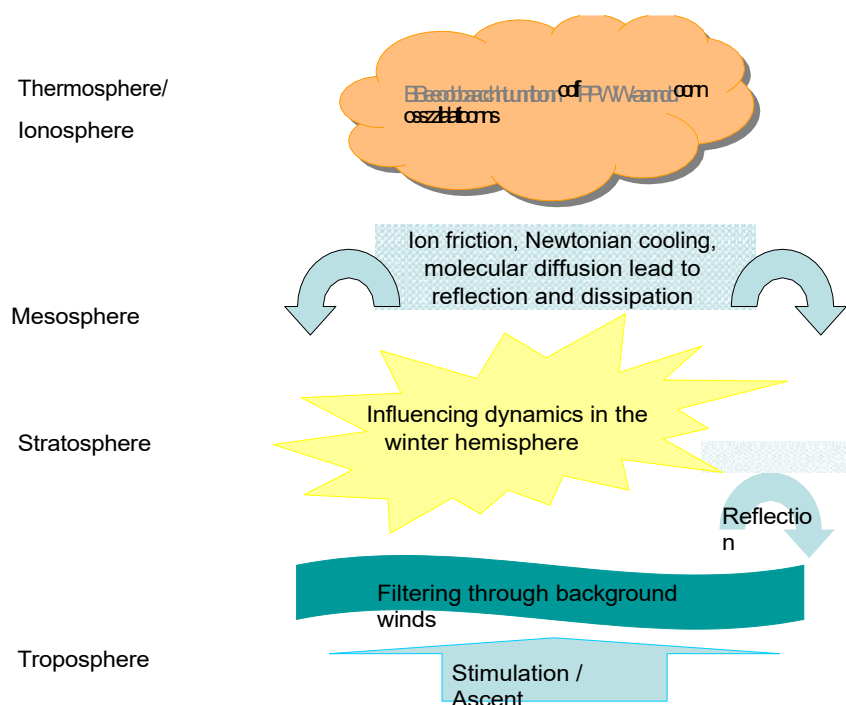


Figure 3.1: Simplified overview of planetary wave (PW) activity in the atmosphere.

The phases of the SPW normally move westwards with increasing altitude. As already mentioned, their amplitude increases exponentially with altitude if the zonal wind is constant. At a certain height, the amplitudes become so large that the waves break. The decisive factor for the breaking of the waves is the zonal wind, which in the real atmosphere varies with altitude and latitude. Although the SPW mostly decays at the height of the middle mesosphere, the amplitudes remain relatively large until then (Barnett and Labitzke, 1990).

Like SPW, the travelling PW in the stratosphere occur mainly in winter (in the mid-latitudes), but their amplitudes are significantly smaller than those of SPW. From observations, the travelling waves can be described as follows (Yun, 1996, references therein):

- ↗ The travelling waves of zonal wavenumber 1 occur primarily in two period ranges at 5 and 16 days and are known as the 5-day wave and 16-day wave (e.g. Rodgers, 1976; Madden and Labitzke, 1981; Hirooka and Hirota, 1985; Pendlebury et al., 2007). These two so-called normal modes mostly move westwards (Madden, 1979; Volland, 1988). On climatological average, their amplitude increases from the equator to the mid-latitudes and decreases again towards the poles. In addition, westward-moving 10-day waves with wave number 1 are also observed (Hirooka and Hirota, 1985).
- ↗ The travelling waves of zonal wave number 2 generally propagate westwards. The observed periods are concentrated in the period ranges of 3 to 7 days (Hirota and Hirooka, 1984), and between 10 and 18 days. At the same meridional wave number, the waves of zonal wave number 2 move slightly slower than those of zonal wave number 1.
- ↗ The travelling waves of zonal wavenumber 3 propagate about equally frequently both to the west and to the east, although no characteristic frequencies have been known. Even shorter waves travel predominantly from west to east (Speth and Madden, 1983).
- ↗ The vertical structure of the amplitude of the propagating waves is different in the stratosphere.

The PWs in the stratosphere in the northern hemisphere are particularly important because they are associated with the stratospheric warming discovered by R. Scherhag in 1952 on the basis of radiosonde data (Lindzen, 1990, and references therein). Stratospheric warming is a characteristic warming of the stratosphere in winter, where temperatures are normally very low. Stratospheric warming usually occurs after a strengthening of the quasi-stationary wave 1

by their interaction with the base flow or sometimes also by the alternating effect of transient waves with the SPW. According to the reflection criterion of *Perl-witz and Harnik* (2003), PW are refracted or reflected when a critical value of vertical wind shear is reached. The negative wind shear during a stratospheric warming prevents the vertical propagation of PW. Either they break and dissipate at the critical layer, weakening the zonal base flow (the wind is weakened from top to bottom in a time sequence), or they are reflected and thrown back into the troposphere. The rise of PW, on the other hand, is only possible when the vertical wind shear is positive, i.e. when the vertical gradient of the zonal wind is positive between 2 and 10hPa.

3.3. Planetary waves in the mesosphere and lower thermosphere

Measurements in the mesosphere/lower thermosphere (MLT) are usually only available locally (radar, airglow, etc.) or with relatively low temporal resolution (satellite-based measurements). The activity of PW in this region is therefore not yet known to the same extent as in the stratosphere. However, there are indications that PW activity in the mesosphere may differ from PW activity in the stratosphere. For example, three- to six-day periods (*Wüst*, 2008, references therein) and quasi-2-day waves (*Fröhlich*, 2005), which develop at the edges of unstable summer jets, can be observed frequently in the mesosphere in summer. Stratospheric PW are not typical during the summer months. The quasi 5-day waves have their maximum amplitude at the equinoxes, and they are stronger in summer than in winter. PW that propagate beyond the stratosphere usually break in the mesosphere. In individual cases, they can also rise further. However, dissipation processes prevent further vertical propagation of the waves in the upper MLT region at the latest. Essentially, three processes or properties contribute to the damping of PW in the MLT region: Newtonian cooling, molecular viscosity or ion friction (*Meyer and Forbes*, 1997). As modelling runs have shown, ion friction is the strongest of these three processes.

PW can also enter the mesosphere indirectly, e.g. by affecting AGW, the breaking of which is crucial for the dynamics in the mesosphere. If PW cause a zonally varying critical wind speed in the lower and middle atmosphere, a change in the frequency or a modulation of the amplitudes of vertically propagating AGW can be caused so that they transport the energy of PW into the mesosphere (*Meyer*, 1999). A modulation of gravity wave fluxes

by 2-day and 16-day PW has been observed in mesospheric winds (*Manson et al.*, 2003) and demonstrated in a modelling study (*Jacobi et al.*, 2006). In the lower thermosphere, AGW are attenuated. This process is associated with convective instability and viscous dissipation (*Forbes*, 1996). PW signatures occur where AGW break (depending on the wind and temperature profile), i.e. either in the mesosphere or E-region, but not in both regions simultaneously. For this reason, PW in the mesosphere and E-region are usually not correlated, although there is a close physical connection (*Lawrence and Jarvis*, 2003).

In *Hunt* (1984), the rapid weakening of PW with large wave numbers above the tropopause and their re-emergence in the MLT region (above 60km altitude) is observed in analyses of a general circulation model (GCM). The energy of large-scale PW, on the other hand, is maximum in the stratosphere in winter and decreases rapidly above it. *Hunt* (1984) suggests that the energy source of the smaller-scale PW is, among other things, the wave-wave interaction, which transfers the energy of large-scale PW to smaller-scale secondary waves (at least in winter), or the influence of vertically propagating AGW.

3.4. Signatures of planetary waves in the ionosphere

Signatures with the properties of PW are also observed in ionospheric parameters (the critical frequency f_{oF} or the proportional maximum electron density of the F2 layer NmF , the magnitude of the maximum electron density hmF or the total electron content T EC) (*Laštovička and Sauli*, 1999; *Altadill*, 2000; *Pancheva et al.*, 2002; *Lawrence and Jarvis*, 2003; *Laštovička et al.*, 2003; *Shalimov and Lapshin*, 2003; *Altadill et al.*, 2004; *Aushev et al.*, 2006; *Laštovička et al.*, 2006; *Rishbeth*, 2006; *Mukhtarov et al.*, 2010, and many more). Because the medium in which PWs propagate is not the ionosphere, but only the thermosphere (neutral gas) if necessary, the signatures of PWs in the ionosphere are called PW-type oscillations (PWTO).

PWTO are described in the f_{oF} with different wavenumbers ($k = 0, 1, \dots$), both westward and eastward moving. A dominant structure in the variations of the f_{oF} is the oscillation of the zonal mean ($k = 0$, *Altadill*, 2000). Subsequently, the PWTO with wavenumber $k = 1$ westward is described as the strongest PWTO in the f_{oF} (*Altadill*, 2000; *Altadill and Apostolov*, 2003; *Forbes and Zhang*, 1997). Typical periods at mid-latitudes are 2, 5, 10, 13.5 and 16 days. The typical relative amplitude of PWTO in f_{oF} is observed to be 5% and up to 15% at extreme events (*Laštovička*, 2006). The

PWTO amplitudes are maximum in winter, whereas the frequency of PWTO occurrence is greatest in summer (*Laštovička*, 2006).

The origin of most PWTO observed in the F2 layer has not been clarified to date. It is often assumed to be the influence of PW originating in the troposphere or stratosphere. The influence of upwelling atmospheric waves on the variability of the ionospheric electron content is estimated to be 15-20% (*Forbes et al.*, 2000; *Rishbeth*, 2006). However, it should be noted that a large part of the PWTO in the F2 region is also caused by periodic variations of the geomagnetic perturbations (e.g. *Forbes et al.*, 2000; *Pancheva et al.*, 2002; *Altadill and Apostolov*, 2003; *Laštovička*, 2006). PWTOs of geomagnetic origin are most frequent in summer, while PWTOs thought to originate in the MLT region are most frequently observed in f oF winter (with the exception of the quasi-2-day wave, *Altadill and Apostolov*, 2003).

3.5. The conditions for the propagation of planetary waves in the thermosphere

As described in sections 3.1 and 2.3.3, the PWs arise from the B effect, i.e. through the influence of the Coriolis force. In chapter 2.3.2 it was pointed out that the Coriolis force only plays a minor role in the thermosphere and that dissipation dampens the PW. It can therefore be assumed that PW cannot exist in the upper atmosphere. Nevertheless, signatures of PW are measured in the ionosphere, i.e. in the region of the thermosphere (see section 3.4), assuming that there is an influence of PW from the troposphere and stratosphere. Several mechanisms have been proposed in the literature for how PW can influence the ionosphere-thermosphere region. Among the suggestions are:

1. The variation of the thermospheric composition: Vertical motions or variations of temperature and diffusion at the turbopause related to PW can cause a periodic change of the thermospheric composition at an altitude of about 100km (ratio $[O/O_2]$), which in turn affects the recombination rate and thus the electron density in the F region (*Mikhailov*, 1983; *Pancheva and Lysenko*, 1988; *Forbes*, 1996).
2. The influence of the ionospheric dynamo: The neutral wind influenced by PW (with corresponding amplitude) can cause PW modulation of the dynamo-induced E-field at altitudes between 100-160km, which in turn leads to peri-

odic changes in the vertical plasma drift. Thus, variations in the height and plasma density of the F region are induced, which are related to PW (*Ito et al.*, 1986; *Pancheva and Lysenko*, 1988; *Forbes*, 1996; *Mukhtarov et al.*, 2010; *Liu et al.*, 2010b).

3. The interaction with tides: The non-linear interaction between PW and tides leads, among other things, to a modulation of the tidal amplitude. The tide modulated with the periods of the PW can rise to greater heights in the thermosphere than the PW itself. Dissipation of the tides (e.g. the semi-diurnal westward moving tide) can cause a significant change in the base current in the lower thermosphere. Thus, modulation of tidal amplitude with PW periods leads to PW variations in the base current, which are transferred to the dynamo-induced E-field and have effects down to the F-region (*Mitchell et al.*, 1996; *Palo et al.*, 1999; *Pancheva et al.*, 2000; *Mayr et al.*, 2004; *Pancheva et al.*, 2006; *Forbes et al.*, 2009; *Immel et al.*, 2009; *Liu et al.*, 2010b).
4. Interaction with AGW: Vertically propagating AGW provide an in situ source of periodic excitation in the mesosphere and E region. If the momentum flux of AGW at this altitude level is modulated by PW, this can serve as a secondary source of PW in the mesosphere or E region (*Hunt*, 1984; *Forbes*, 1996; *Meyer*, 1999; *Manson et al.*, 2003). See also section 3.3.
5. Nonlinear interaction between PWs: The nonlinear interaction between PWs can lead to the generation of secondary PWs that are capable of ascending into the mesosphere and lower thermosphere (*Hunt*, 1984; *Pancheva et al.*, 2007, 2008a), where they influence either the thermospheric composition (coupling like mechanism 1) or the wind system (coupling like mechanism 2).

The coupling mechanisms presented are schematically captured in Fig. 3.2. For the The amplitudes of the PW variations in the E region are decisive for the 1st and 2nd coupling processes. The significant influence of the 5- and 10-day wave with zonal wavenumber 1 on the lower thermosphere and dynamo region was demonstrated by *Meyer and Forbes* (1997) using analyses with numerical models. Recently, simulations with the numerical model MUAM (Middle and Upper Atmosphere Model) have shown the propagation of the migrating 10-day and 16-day wave into the lower thermosphere (*Pogoreltsev et al.*, 2007). Complementarily, some case studies show coexistence of PW in the middle atmosphere and PWTO in the ionosphere (e.g. *Lawrence and Jarvis*, 2003; *Borries et al.*, 2007; *Pancheva et al.*, 2008b; *Mukhtarov et al.*, 2010). The PW that can penetrate farthest into the thermosphere are particularly fast equatorial waves (normal modes and ultra fast Kelvin waves) with a period of 33 hours and 3.5 days. They are only transmitted above 160km altitude by ionic friction and molecular viscosity.

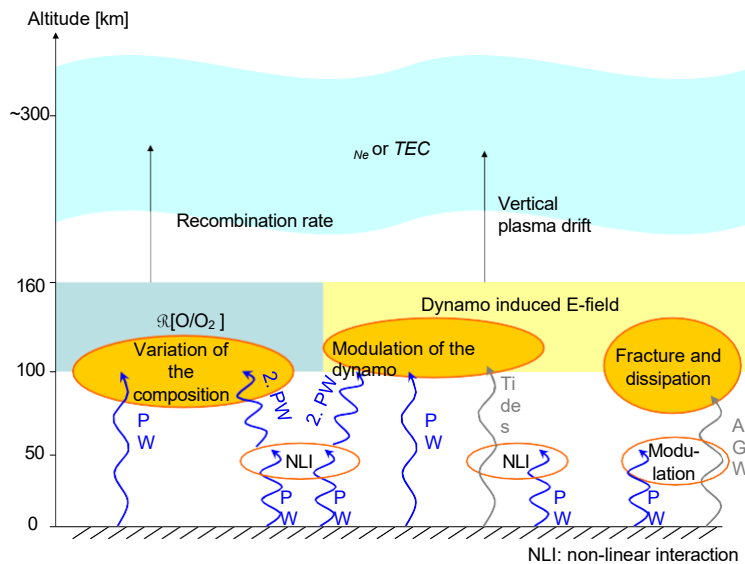


Figure 3.2: Schematic representation of some possible coupling mechanisms for the transfer of energy from PW to the ionosphere.

suppressed (results of simulations with MUAM in *Pogoreltsev et al.*, 2007).

However, not all vertically propagating PW have a correspondingly large amplitude in the E region for the 2nd coupling mechanism. Studies with numerical models could neither show a significant influence of SPW (*Pogoreltsev et al.*, 2007) nor the significant influence of the quasi-2-day wave and quasi-16-day wave on the thermo-sphere and ionosphere (*Hagan et al.*, 1993; *Forbes et al.*, 1995). For these PW, indirect mechanisms such as tidal or AGW modulation in conjunction with the 1st and 2nd coupling process are often proposed to produce corresponding PWTO in the F region. As the listed variations of coupling mechanisms show, the relationship between PW activities in the different atmospheric layers is complex (*Forbes*, 1996; *Lawrence and Jarvis*, 2003). At some times, strong PW can be observed in the stratosphere, while no PW is found in the higher levels. At other times, PW can be observed in the mesosphere, the E region or the F region, while no corresponding significant PW activities occur in the stratosphere. Further physical and numerical analyses and better coverage with observations (especially in the altitude range between 100 and 300km) are needed to understand the primary mechanisms.

4. Data basis

After the basics of PW in the upper atmosphere have been described in the previous chapters, the data set to be analysed is presented in this chapter. These are maps that show the vertically integrated electron content T EC (Total Electron Content) of the atmosphere.

The T EC is calculated from measurements of the total electron content along a beam path. (s T EC) is derived.

$$s \text{ T EC} = \int N_e(x) dx \quad (4.1)$$

$N_e(x)$ is the electron density at a location x . To determine the s T EC, transionospheric radiolink measurements are used, which are explained in chapter 4.1. Various global navigation satellite systems (GNSS), such as GPS, GLONASS and in future also GALILEO, both ground-based and satellite-based, can be used for the s T EC calculation. The operation of GNSS is explained in section 4.2. The principles of TEC computation can be found in Chap. 4.3. At DLR Neustrelitz, bo- den-based s T EC measurements are used to compute regional T EC maps, which are the main data basis of this work. Their creation is described in chapter 4.4. Chapter 4.5 compares the TEC maps produced at DLR with those of other institutes.

4.1. Transionospheric radiolin measurements

According to Fermat's principle, an electromagnetic signal always propagates along the ray path with the lowest refractive index. The optical path length L , which denotes the integral of the refractive index n_{fon} (see Eq. 2.2) along a beam path (distance between transmitter T and receiver R), is therefore minimal.

$$L = \int_T^R n_{fon}(x) dx \quad (4.2)$$

The optical path length is the crucial link between the GNSS measurements and the integral electron density (Eq. 4.1).

$$L = \int_T^R dx + \int_T^R (n_{\text{fon}}(x) - 1) dx = p + f_{j,p} + \int_T^R (n_{\text{fon}}(x) - 1) dx \quad (4.3)$$

As Eq. 4.3 shows, the optical path length L can be considered as the sum of the geometrically shortest connection p between T and R , a term $f_{j,p}$ caused by the curvature of the beam (in a first approximation this term can be neglected) and a refraction-dependent part $f_{j,fon}$. Eq. 4.3 shows that L deviates from the geometrically shortest link p as soon as the refractive index along the beam path is different from 1. This condition is fulfilled in the ionosphere (see chapter 2.2.2). The difference between p and L is the ionospheric propagation error $f_{j,fon}$ (in first approximation). By substituting Eq. 2.2 into Eq. 4.3, the correlation with the electron density N_e is established.

$$f_{j,fon} = - \int_r^R \frac{K}{2} N_e(x) dx \quad (4.4)$$

The integral over the electron density can now be replaced by $s T \text{ EC}$ (Eq. 4.1):

$$f_{j,fon} = - \int_r^R \frac{K}{2} s T \text{ EC} \quad (4.5)$$

4.2. Global Navigation Satellite Systems (GNSS)

Global navigation satellite systems (GNSS) enable a user on Earth or in near-Earth space to determine his or her three-dimensional position, speed and time permanently and with high accuracy, regardless of weather conditions. This is done by receiving and evaluating the electromagnetic signals transmitted by the satellites. At a flight altitude of around 20,000km above the earth's surface, a constellation of 24 to 30 satellites is used so that the receiver has visual contact with at least four satellites at all times.

For location determination via satellites, the transit times of the transmitted radio signals from at least four satellites are measured. Each of these (pseudo) distances defines a spherical area around the corresponding satellite on which the receiver is located. The spherical areas around three satellites result in a maximum of two points as an intersection. One of these is located a few thousand kilometres from the Earth's surface and can be

are therefore discarded. The other represents the searched position of the receiver. A fourth satellite is needed to determine the deviation between the clocks of the GNSS satellites (highly accurate atomic clocks) and those of the receiver (less accurate quartz clocks) and to calculate it from the measured travel times, i.e. to convert the pseudo-distances into actual distances.

The distance between the satellite and the observer is calculated from the signal propagation time. Each satellite permanently transmits its specific code and its orbit data (ephemeris). The receiver generates the same satellite codes and adjusts them to the received satellite signals via a time and frequency shift. If the clocks in the satellite and receiver are exactly synchronised (which cannot be assumed), the measured time shift corresponds to the time of flight of the satellite signals. Ultimately, the distance between the satellite and the receiver results from multiplying the signal propagation time by the signal speed (approximately the speed of light).

The structure of the data signal is explained below using the example of GPS (Global Positioning System, developed and operated by the US Department of Defense). With GPS, the data signal is transmitted in parallel on two coherent carrier frequencies. The carrier frequencies L_1 and L_2 are derived from the fundamental frequency of the satellite oscillator $f_{00} = 10.3\text{MHz}$ ($A_{00} = 9.3\text{m}$):

$$L_1 = 154f_{00} = 1575.4 \text{ MHz} \quad (4.6)$$

$$L_2 = 10f_{00} = 17.60\text{MHz} \quad (4.7)$$

On the L1 frequency, the C/A code ("Coarse/Acquisition") is used for civilian use and, orthogonally, the P/Y code ("Precision/encrypted"), which is not publicly known, for military use. The second frequency L2 transmits only the P/Y code. Optionally, the C/A code can also be transmitted on the second frequency. In addition to the C/A and P code, the navigation message is modulated on both carrier frequencies. In total, each of the two signals consists of three parts: Carrier wave, code and navigation data.

4.3. TEC calculation from GNSS measurements

The (pseudo) distance P_r between the satellite and the receiver contains, in addition to the geometric distance p and the ionospheric propagation error $f_{j,\text{fon}}$ (Eq. 4.5) further propagation errors:

$$\begin{aligned} P_r &= c(t_r - t_T) \\ &= p + c(f_j t_r - f_j t_T) + f_{j,\text{trop}} + f_{j,\text{fon}} + c(b_T + b_r) + E_p. \end{aligned} \quad (4.8)$$

These are the clock error at transmitter and receiver $f_{j,T}$ and $f_{j,R}$, the propagation error caused by refraction in the troposphere $f_{j,trop}$, satellite and receiver biases b_T and b_R and the code noise E_P . Of the summands in Eq. 4.8, p , $f_{j,trop}$, $f_{j,T}$ and $f_{j,R}$ are frequency independent. They can therefore be eliminated by the difference of the measurements on both carrier frequencies. The code phase difference of the P-codes on L_1 and L_2 is called the "pseudorange ionospheric combination" (P^P).

$$\begin{aligned} P^P &= P_2 - P_1 = f_{j,fon}^P \cdot f_{j,T}^P - (f_{j,b}^P + f_{j,E}^P) \\ f_{j,b}^P &= b_T^P - b_R^P : \text{differential bias of the transmitter} \\ f_{j,E}^P &= b_R^P - b_T^P : \text{Differential bias of the receiver} \\ f_{j,E}^P &= E_{P_2} - E_{P_1} : \text{Difference of the code noise of } L_2 \text{ and } L_1 \end{aligned} \quad (4.9)$$

By substituting Eq. 4.5 and converting to sTEC, we obtain:

$$sTEC = \frac{\frac{1}{K} \frac{L_1^2 L_2^2}{L_1 - L_2} (P + f_{j,b}^P + f_{j,b}^P - f_{j,E}^P)}{K \frac{L_1^2 L_2^2}{L_1 - L_2}} = \frac{P}{K} \frac{L_1^2 L_2^2}{L_1 - L_2} + sTEC_{cal} \quad (4.10)$$

The calculation of $sTEC_{cal}$, which contains the random errors and the differential code biases, is described in more detail in *Sardón et al.* (1994).

Alternatively, s T EC can also be calculated from the carrier phase difference of L_1 and L_2 . Instead of Eq. 4.8, Eq. 4.11 is to be applied.

$$L_T^r = p + c(f_{j,T} - f_{j,R}) + f_{j,trop} - f_{j,fon} + c(b_T + b_R) + NA + E_L \quad (4.11)$$

The advantage of the s T EC calculation from phase differences is the significantly smaller phase noise E_L . However, due to the ambiguity NA (N is the wavelength of the carrier frequency), the s T EC calculated from carrier phases is only a relative TEC measure, with an unknown deviation from the absolute s T EC. The relative accuracy of this s T EC measurement is with 0.01 TECU (1TECU=10¹⁶ electrons per m²) much better than that of the code phases. For this reason, the s T EC determination from carrier phases has various important applications. On the one hand, the carrier phase s T EC is used to significantly improve the determined absolute s T EC by fitting the carrier phase s T EC into the noisy code phase s T EC using the least square method (*Jakowski*, 1996). On the other hand, the carrier phase s T EC can be used very well for the investigation of small-scale disturbances, such as the signatures of AGW (*Borries et al.*, 2009).

4.4. TEC map creation

The routine for creating the TEC maps (vertical TEC) in DLR is described in detail in *Jakowski* (1996). The procedure is summarised briefly here.

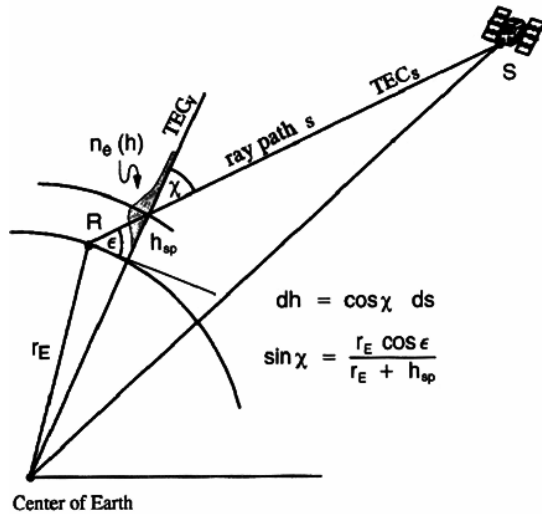


Figure 4.1: Mapping function to convert the s T EC into a vertical TEC (taken from Jakowski, 1996).

To create the TEC maps, the s T EC measurements described in Chapter 4.3 are converted into a vertical T EC along an inclined measurement beam between transmitter and receiver (so-called slant TEC). DLR currently uses a mapping function based on a "single-layer approximation" of the ionosphere (see Fig. 4.1). For this purpose, it is assumed that all electrons are located in a layer with a height of $h_f = 400\text{km}$. The height of the layer was chosen slightly above the F2 layer in order to take into account the overall larger number of electrons above the F2 layer up to the satellite at an altitude of about $20,000\text{km}$. With the help of simple geometry relations, the vertical T EC is calculated from the slant TEC (s T EC), taking into account the elevation E and the Earth's radius R_e . The vertical T EC is calculated from the slant TEC (s T EC).

$$T EC = \frac{1}{1 - \frac{R_e \cos E}{R_e + h_f}} s.T EC \quad (4.12)$$

Typical vertical TEC values range from a few TECU at night in high latitudes to 200TECU during the day near the equator and at times of geomagnetic storms.

The TEC maps are created by assimilating the vertical T EC data into a suitable TEC model. For this purpose, DLR has developed empirical regional TEC models (NTCM2 for the European region and NTCMP for the polar regions). The T EC values are compared with a

The Gaussian function is weighted depending on the distance of the measurement to the map grid point. The half-width of the Gaussian function indicates the main area of influence of the measurement (see Fig. 4.2). Even with a small number of measurements, this technique provides useful ionospheric corrections.

The signatures of PW in the ionosphere are periodic deviations of the TEC from its climatology (regular or long-term variations given by the sun, e.g. the daily, seasonal and solar cycle). A large part of its climatology can be described by a running median¹ (depending on location and time of day). The relative difference between observation and median implements a very simple bandpass filter by which variations in TEC in the period range of PW are separated from the climatology. For this reason, maps of the relative differential TEC (f_j, TEC_{rel}), which is calculated according to Eq. 4.13, are used for the analyses of PWTO.

$$f_j, TEC_{rel} = \frac{T EC - T EC_{med}}{T EC_{med}} \quad (4.13)$$

$T EC$ symbolises the TEC value of a map grid point. $T EC_{med}$ is the median value of a running window with a width of 27 days corresponding to the grid point and the time of day. In this way, periods smaller than one day as well as periods larger than 27 days are largely suppressed in the f_j, TEC_{rel} .

4.5. Comparison of different TEC maps

Internationally, TEC maps are produced by various facilities and institutes. DLR Neustrelitz has been producing regional TEC maps since 1995. Initially, TEC maps were only produced for the European region (-20-40° E, 32.5-70° N). Since 2002, hemispherical TEC maps have also been available for the North Pole region (50° N-North Pole), and since 2003 for the South Pole region (50° S-South Pole). Because of their hemispheric coverage and the high PW activity in the northern hemisphere, the analyses in this paper are limited to the north pole TEC maps. The DLR TEC maps are produced with an hourly resolution and 2.5° meridional and 7.5° zonal grid spacing. The data coverage is shown in Fig. 4.2 using the North Pole TEC map for 6 April 2000 18:00UT as an example. Around each TEC measurement the main area of influence is marked by blue rings. However, assimilation causes the influence of the measurements to continue beyond the circles in a weakened form. Fig. 4.2 shows that there is particularly high data coverage over Scandinavia and the USA. In contrast, the density of measurement data over the oceans is small. The absolute error of the DLR

¹The median suppresses a distortion of the mean behaviour by extreme events.

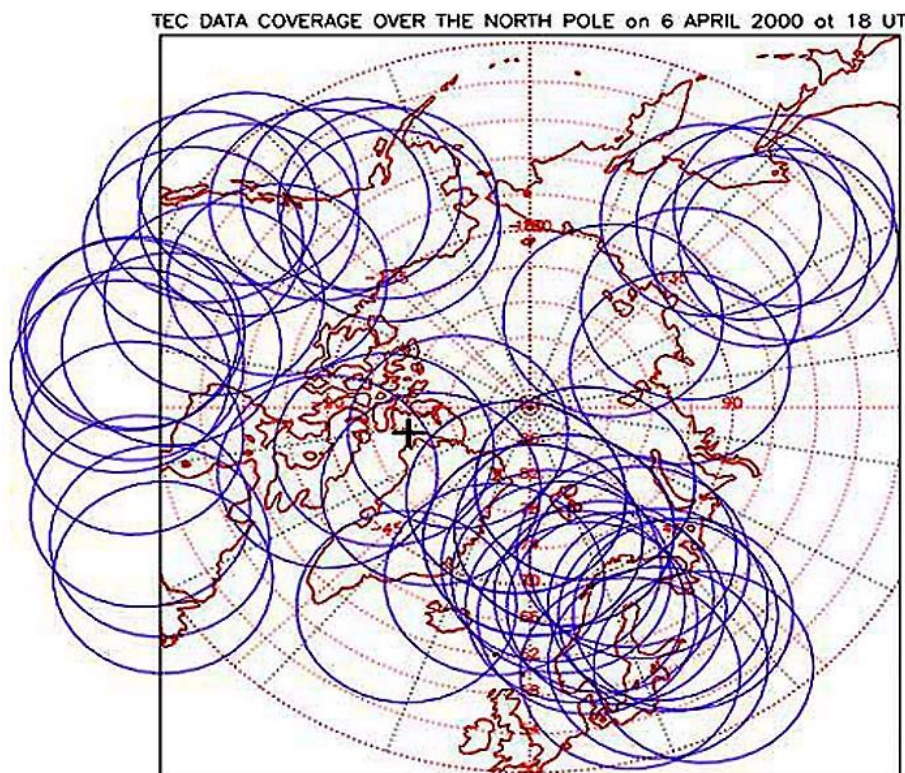


Figure 4.2.: Data coverage of the DLR North Pole TEC map on 6 April 2000 18:00UT. The blue circles mark the main area of influence of the TEC measurements.

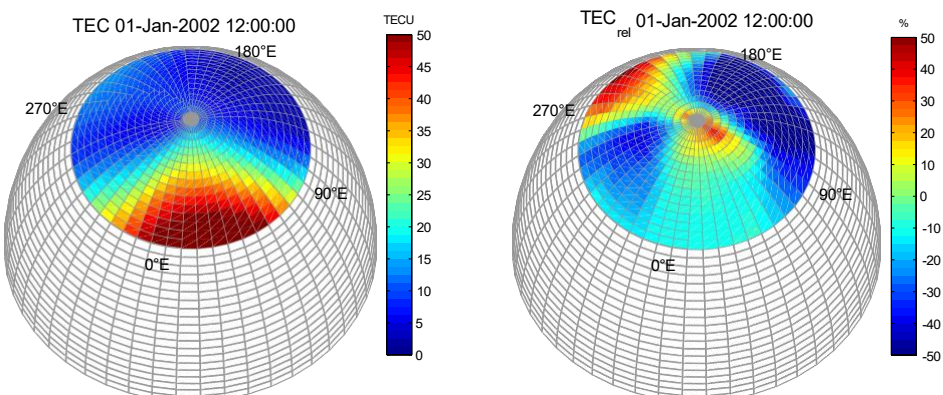


Figure 4.3.: Example of a DLR North Pole TEC map and the corresponding $f_j, \text{TEC}_{\text{rel}}$ -card

North Pole TEC maps is 1-3TECU and the relative error is about 0.5TECU.

An example of a DLR North Pole TEC map and the corresponding $f_j, \text{TEC}_{\text{rel}}$ map is shown in Fig. 4.3. While in the TEC map only the daily tide with zonal wave number 1 can be seen, in the $f_j, \text{TEC}_{\text{rel}}$ map a structure with wave number 2 comes to the fore.

Recently, global TEC maps have been made available online² by the IGS (International GNSS Service). The IGS TEC maps are the weighted average of TEC maps produced at four different institutions: The Center for Orbit Determination in Europe (CODE) at the University of Bern in Switzerland, the European Space Operations Centre Ionosphere Monitoring Facility at ESA in Darmstadt, Germany, the Ionospheric and Atmospheric Remote Sensing Group at the Jet Propulsion Laboratory (JPL) in Pasadena, California, USA, and the Research Group of Astronomy and Geomatics at the Technical University of Catalonia (UPC) in Barcelona, Spain. The weighting is based on the comparison of the slant TEC of a small number of IGS stations and on the result of an external self-consistency validation. The IGS TEC maps have been routinely validated with TOPEX altimeter measurements since 2001. They are produced with a temporal resolution of 2 hours and a grid size of 2.5° in width and 5° in length.

The mean of the absolute differences of both maps is 0-3 TECU. As expected, the greatest differences are where the greatest data density is. If one compares directly

²<http://cdaweb.gsfc.nasa.gov>

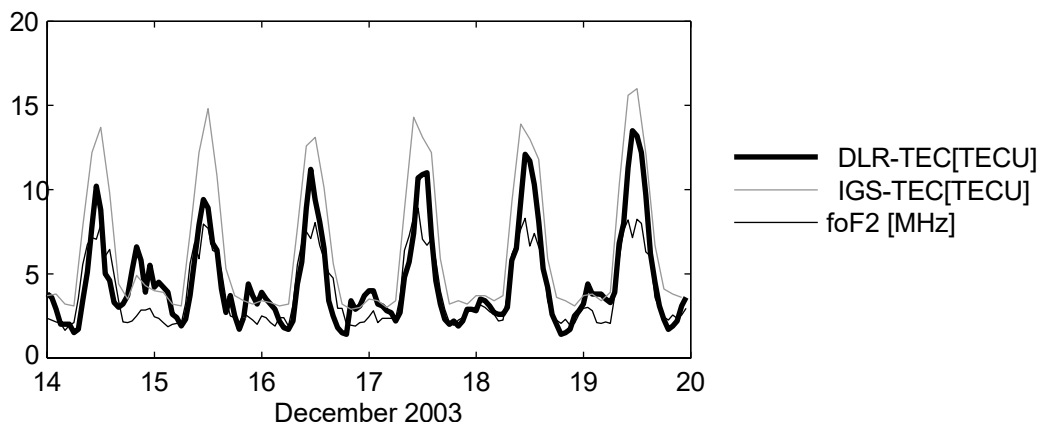


Figure 4.4: Comparison between the DLR North Pole TEC maps, the IGS TEC maps (at grid point 15° E/ 55° N) and f_{OF} measurements of the ionosonde Juliusruh from 14 to 19 December 2003. This choice of location and time is random.

the time series of the different TEC maps (an example can be found in Fig. 4.4), it can be seen that the DLR maps contain much more detail than the IGS maps. On the one hand, details can be lost when creating the IGS maps due to the averaging of different TEC maps. On the other hand, different reconstruction techniques can lead to the differences.

The correlation with the critical frequency f_{OF} measured by the Juliusruh ionosonde (also in Fig. 4.4), which is proportional to the maximum electron density of the F2 layer, yields a correlation coefficient of 0.84 for the DLR North Pole TEC maps and 0.96 for the IGS TEC maps. Without knowledge of the layer thickness, however, it is impossible to assess which TEC maps better represent the state of the ionosphere. In the course of this work, primarily the DLR TEC maps are analysed and the results of the IGS TEC maps are validated in the appendix.

5. Methods of analysis

Spectral analysis refers to the decomposition of a function/signal into its spectral components, i.e. its frequency components. It gives the possibility to identify periodic as well as stochastic features. In this work, spectral analysis will be used to identify periodic signals. A large selection of methods for spectral analysis helps to make accurate statements about the frequency components contained in the signal in many different applications. According to *Buttkus* (1991), the methods for the spectral decomposition of signals can be divided into three classes¹. Firstly, the classical methods, i.e. linear operations such as Fourier and wavelet analyses, secondly, the model fitting methods in which the power spectra are estimated, such as autoregressive methods and the use of singular value decomposition, and thirdly, information-theoretical approaches. Of the three groups, various methods were tested² with the result that the classical methods were considered to be the most reliable because the fewest assumptions are made about the signal. The Fourier and wavelet analyses are briefly described in the following two sections. From both analyses a method for the detection of PW was compiled, which is explained in section 5.3. The use of wavelet analysis for signal filtering and downsampling is described in section 5.2.3.

5.1. Fourier analysis

5.1.1. Fourier spectrum

According to Fourier's theorem, each signal f can be described by the sum of infinitely many partial oscillations

$$f(t) = \frac{1}{2\pi} \int_{-\infty}^{\infty} f^*(w) e^{wt} dw \quad (5.1)$$

¹Other classifications are also possible.

²These preliminary studies are not presented here because of their complexity.

This applies to continuous functions in the Hilbert space of square-integrable functions. In Eq. 5.1 $\hat{f}(w) = 0.5(C(w) + iS(w))$ are the Fourier coefficients describing the amplitudes $A(w) = S(w)^2 + C(w)^2$ and the phase $\phi = \arctan(C(w)/S(w))$ of the partial signals with the angular frequency w . The Fourier coefficients are calculated by

$$\hat{f}(w) = f(w) = \frac{1}{\pi} \int_{-\infty}^{\infty} f(t) e^{-iwt} dt. \quad (5.2)$$

Equation 5.2 describes the Fourier transform that decomposes the signal $f(t)$ into its spectral components $\hat{f}(w)$, while equation 5.1 represents the inverse Fourier transform. The w -plane is called the frequency or phase space. Parseval's theorem describes the conservation of energy, i.e. the energy of $\hat{f}(w)$ corresponds to the energy of $f(t)$:

$$\int |f(t)|^2 dt = \left(\int f(t) \overline{f(t)} dt \right) = \left(\int \hat{f}(w) \overline{\hat{f}(w)} dw \right) = \int |\hat{f}(w)|^2 dw. \quad (5.3)$$

Das Fourierspektrum $P(w) = \hat{f}(w) \hat{f}^*(w)$, das oft auch als Leistungsdichtespektrum bezeichnet wird, ist das komplexe Produkt der Fouriertransformierten. Der Betrag von $\hat{f}(w)$, oder die Wurzel des Fourierspektrums, beschreibt die Amplituden der Teilsignale und wird als Amplitudenspektrum bezeichnet.

The definitions of the continuous Fourier transform in Eq. 5.1 and Eq. 5.2 do not apply in the case of a discrete signal. For a discrete signal x_t , which is sampled uniformly on the interval $[0, Nf_j t]$ and continues periodically at infinity, the finite discrete Fourier transform (DFT, Eq. 5.5) and its inverse (Eq. 5.4) apply.

$$x_n = \sum_{n=-N/2}^{N/2} x_t e^{-i2\pi n t / N} \quad t = 0, 1, \dots, N-1 \quad (5.4)$$

$$x_n = \frac{1}{N} \sum_{t=0}^{N-1} x_t e^{-i2\pi n t / N} \quad n = -N/2, \dots, N/2 \quad (5.5)$$

Here N is the number of discrete points and $f_j t$ is the sampling rate. The Nyquist theorem applies to the DFT, which states that no frequencies greater than $w_d = (f_j t)^{-1}$ (Nyquist frequency) can be sampled. The smallest frequency that can be sampled is $(Nf_j t)^{-1}$. If the data are normally distributed, both the real part and the imaginary part of the Fourier spectrum are normally distributed. Because the square of a normally distributed variable x^2 ver-

is distributed with one degree of freedom, \hat{x}_n^2 is distributed with 2 degrees of freedom.

$$\frac{N \hat{x}_n^2}{u^2} = \frac{1}{2} P_{x2}$$

$N \hat{x}_n^2 / u^2$ ist das mit der Varianz von u^2 normierte Fourierspektrum von x_t . Die 95% signifikanten Amplituden eines normalverteilten Signals werden durch die Multiplikation

of the Fourier spectrum of its background noise P with the 95% value for x^2 (Tozeren and Compo, 1998). The description of the background noise is therefore essential for the determination of the significances. The background noise of the data used is approximately white noise. With white background noise, $P = 1$.

5.1.2. Correlation and cross spectrum

One of the most important laws for the Fourier transform is the convolution theorem. The convolution of two functions $f(t)$ and $g(t)$ is introduced as:

$$c_{fg}(T) = f * g(T) = \int_{-\infty}^{\infty} f(t) g(T-t) dt. \quad (5.6)$$

T is the shift of the two signals. The convolution theorem states that the Fourier transform of a convolution is equal to the product of the Fourier transforms of the two signals

$$\hat{c}_{fg}(w) = \text{irff}(\hat{f}_w \hat{g}_w) = \hat{f}_w \hat{g}_w.$$

The use of the convolution theorem thus provides a quick way to calculate the correlation and autocorrelation of signals. The correlation coefficients are given by:

$$c_{fg}(T) = \frac{1}{\sqrt{N}} \sum_{n=1}^{N-1} f(n) g(n-T)$$

$$c_{ff}(T) = \frac{1}{\sqrt{N}} \sum_{n=1}^{N-1} f(n) f(n-T).$$

The complex product of 2 Fourier transforms is called a cross spectrum.

$$P_{fg}(w) = \hat{f}_w \hat{g}_w^* = L(w) - i Q(w) = P_{fg}(w)^{\text{fft}} \quad (5.7)$$

It should be noted that the cross spectrum is complex. The real component L is called the cospectrum or effective spectrum and the imaginary component Q is called the square spectrum or blind spectrum. The cospectrum measures the correlation of the two series that are in phase, while the square spectrum measures the correlation of the two components that are shifted by 90° .

According to Eq. 5.7, the co- and square spectrum together form the so-called cross amplitude $P_{fg} = \sqrt{L^2 + Q^2}$, i.e. that part of the variance of both processes which can be described by a fixed phase difference $\phi = \arctan(-Q/L)$.

5.1.3. Amplitude modulation

If a periodic carrier signal $c(t)$ is multiplied by any signal (t) , this is called amplitude modulation.

$$f(t) = c(t)(t)$$

The frequency of the carrier signal w_c is called the carrier frequency. A distinction must be made between the modulation of real and complex carrier signals. With the modulation of complex signals $c(t) = e^{jw_c t}$, a shift of the spectrum by w_c takes place.

$$\begin{aligned} f'(w) &= \frac{1}{\text{ir}} \int_{-\infty}^{\infty} e^{-jw_c t} c(t) e^{-jwt} dt \\ &= \frac{1}{\text{ir}} \int_{-\infty}^{\infty} c(t) e^{-(w-w_c)t} dt \\ &= f(w + w_c) \end{aligned} \quad (5.8)$$

whereas in the modulation of real carrier signals $c(t) = \cos w_c t = 0.5(e^{jw_c t} + e^{-jw_c t})$ the spectrum of (t) is mirrored on both sides of the carrier frequency.

$$\begin{aligned} f'(w) &= \frac{1}{\text{ir}} \int_{-\infty}^{\infty} 0.5(e^{jw_c t} + e^{-jw_c t})(t) e^{-jwt} dt \\ &= \frac{1}{\text{ir}} \left(\int_{-\infty}^{\infty} (t) e^{-(w-w_c)t} dt + \int_{-\infty}^{\infty} (t) e^{-(w+w_c)t} dt \right) \\ &= \frac{1}{\text{ir}} (-f(w - w_c) + f(w + w_c)) \end{aligned} \quad (5.9)$$

The energy of the frequency components is divided equally between the sidebands in the Fourier spectrum of f .

Since natural carrier signals are generally real, the following investigations are based on Eq. 5.9. The sidebands can be calculated back to the modelling frequency by slight transformations.

5.1.4. Short-term Fourier analysis

Fourier analysis does not provide time-local information about the frequencies of a signal. In many cases, however, it is of interest to investigate the temporal variability of the signal and its frequencies. One possibility is short-time Fourier analysis (or windowed Fourier transform), which is established as a standard technique for time-frequency localisation (Daubechies, 1992). An alternative method is the wavelet transform, which is discussed in the following section (5.2). The Short-Time Fourier Analysis

can be regarded as a preliminary stage to the wavelet transformation.

For the short-term Fourier analysis, a window function w is chosen that has a maximum of 1 at $t = 0$ and approaches zero from $\pm W$ (Bäni, 2002). The signal $f(t)$ is calculated with

is multiplied by a version of the window function $w(t-T)$ shifted by T , whereby a better temporal localisation of the frequency components is achieved. The Fourier transform is applied to the "windowed" signal f_w . The Gaussian bell curve

$(t) := e^{-\frac{t^2}{w^2}}$, which is used in this work, is an often-used window function.

It has the advantages that its Fourier transform is again a Gaussian bell and that it optimally minimises the Heisenberg uncertainty relation. The accuracy of the temporal localisation depends on the window width w . Because the Gaussian curve is infinitely wide, the variance applies here as the window width.

The short-time Fourier transform is defined by

$$f'(Tw) = \int_{-oc}^{+oc} f(t)w(t-T) e^{-\frac{t^2}{w^2}} dt. \quad (5.10)$$

Figure 5.1 shows the spectrum of the short-time Fourier transform of an exemplary si-

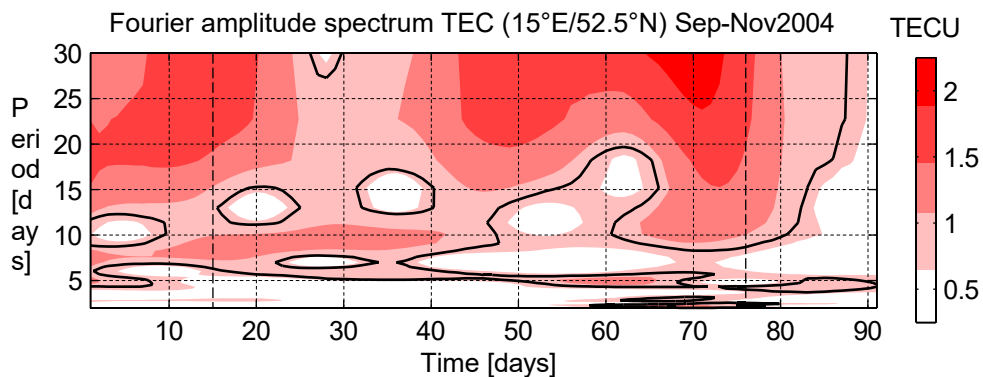


Figure 5.1: Amplitude spectrum calculated with the short-term Fourier analysis with the Gaussian function as window function (window width 30 days). The black solid line encloses the areas with 95% significance. The dashed lines delimit the reliable range of the analysis.

gnal taken from the TEC maps. The Gaussian bell curve with a window width of 30 days serves as the window function. The period-time representation was chosen because the periods of the PW, which are very close together in the phase space, can generally be better represented in this type of representation.

Since only little signal information is included in the analysis at the edges, the outer 15 days of the spectrum are not representative. They are delimited by dashed lines. Significant oscillations of the TEC are mainly found with periods of 8 to 10 days.

days, 5 days and after the 60th day between 2 and 3 days can be read in the spectrum. The oscillations with periods greater than 15 days are difficult to separate in the Fourier spectrum. The reason for this is that the Fourier frequencies in this range are far apart and that the so-called leakage effect (described in more detail in section 5.1.5) distributes the energy of a signal that has a frequency between two Fourier frequencies over several Fourier coefficients.

In Fig. 5.1 it can be seen that the smaller periods are clearly more sharply mapped in the phase space than the larger periods. This difference is mainly caused by the Fourier frequencies in the lower part of the spectrum, which are closer together in this representation. However, the Heisenberg uncertainty principle, which describes the relationship between the resolution of a spectrum in time and phase, states that as the sharpness of the phase increases, the sharpness in time decreases. Therefore, it can be assumed that in the higher frequency range of the spectrum, the oscillations cannot be localised exactly with this method.

5.1.5. Limitations of discrete Fourier analysis

Although discrete Fourier analysis is a very accurate variant of the spectral decomposition of discrete signals, two weaknesses should nevertheless be noted.

Firstly, the signal is reproduced very well exclusively at the Fourier frequencies. If the frequency of a partial signal does not exactly meet a Fourier frequency, but lies between two Fourier frequencies, the energy of the signal is distributed (leakage effect). It should be noted that not all of the energy is distributed to the two neighbouring Fourier frequencies, but also to the second and third neighbour. About 9% of the energy is two Fourier frequencies and 3% four Fourier frequencies away from the original signal. The leakage effect can be reduced by increasing the sampling rate.

Secondly, it should be noted that the sampled signal only contains frequencies below the Nyquist frequency. Signals above the Nyquist frequency produce a distortion of the original signal. This effect, called aliasing, must be taken into account in any spectral analysis with discretely sampled signals. Due to the discrete sampling of a time series, short-wave (i.e. high-frequency) periodic components are detected as long-wave (low-frequency) components. To avoid the associated difficulties, the Nyquist theorem must be observed.

5.2. Wavelet analysis

5.2.1. Continuous wavelet transform

The wavelet transform is a tool that splits data, functions or operators into components of different frequencies and then examines each component with a resolution that matches its scale. Similar to short-time Fourier analysis, signal analysis with the wavelet transform is called a time-frequency method because the result depends on two variables, the scale s (or frequency) and the time shift T (Daubechies, 1992).

The continuous wavelet transform $\langle x \rangle_{\text{wavelet}}$ of a time series $x(t)$ is defined as the convolution of the time series with a family of translated and dilated functions $\langle J \rangle_{s,T}(t)$. The wavelet coefficients $\langle x \rangle_{\text{wavelet}}$ are given by

$$\langle x \rangle_{\text{wavelet}} = \langle x \rangle_{\text{wavelet}} = \frac{1}{c_w} \int_{-\infty}^{\infty} x(t) \langle J \rangle_{s,T}^*(t) dt \quad (5.11)$$

is calculated. The angle brackets describe the inner product (scalar product) of both functions.

Here the wavelet function is

$$\langle J \rangle_{s,T}(t) = s^{-p} \langle J \rangle_0 \left(\frac{t - T}{s} \right) \quad (5.12)$$

das mit T verschobene und mit s skalierte Mutterwavelet $\langle J \rangle_0$. Der Parameter s ist $s = 0$ wird aus diesem Grund als Skalenfaktor und T als Translationsparameter bezeichnet. Im Term s^{-p} bewirkt s eine vertikale Streckung oder Kompression, abhängig von p . In der Literatur wird gewöhnlich $p = 0.5$ gesetzt (bspw. Torrence und Compo, 1998), damit die Norm von $\langle J \rangle_{s,T}(t)$ gleich der Norm des Mutterwavelets ist.

$$\begin{aligned} \|\langle J \rangle_{s,T}\|^2 &= \int_{-\infty}^{\infty} |\langle J \rangle_{s,T}(t)|^2 dt \\ &= s^{1-2p} \int_{-\infty}^{\infty} |\langle J \rangle_0(u)|^2 du \end{aligned} \quad (5.13)$$

If the mother wavelet $\langle J \rangle_0$ is normalised to 1, it follows from equation 5.13 that the wavelet coefficients $\langle x \rangle_{\text{wavelet}}$ are normalised for $p = 0.5$ (Kaiser, 1994). Therefore, $p = 0.5$ is used in this work.

If the signal is to be reconstructed, the energy of the wavelet transformed radio tion must be equal to the energy of the function. This results in the admissibility condition for wavelets

$$0 < c_w := \int_{-\infty}^{\infty} |\langle J \rangle_0(u)|^2 du < \infty. \quad (5.14)$$

Only functions that fulfil this condition are wavelets.

The next step is to apply Parseval's identity. According to this, the inner product of two vectors is equal to the inner product of their two Fourier transforms.

$$\langle x \rangle_{\text{wavelet}} = \langle x \rangle_{\text{wavelet}} = \langle x f \rangle_{\text{Fourier}} = \langle x f \rangle_{\text{Fourier}} \quad (5.15)$$

The Fourier transform of $\langle JJJ_{sIT} \rangle$ is

$$\begin{aligned}\langle JJJ_{sIT} \rangle(w) &= \frac{1}{\sqrt{1r}} \int_{-\infty}^{\infty} \langle JJJ_{sIT} \rangle(t) e^{-jw t} dt \\ &= S^{1-p} e^{-f_s T} \langle JJJ_0 \rangle(sw)\end{aligned}\quad (5.16)$$

Substituting Eq. 5.16 into Eq. 5.15 gives another way to calculate the wavelet coefficients:

$$\langle JJJ_{sIT} \rangle(w) = \frac{\sqrt{1r}}{c} S^{1-p} \cdot \langle JJJ_0 \rangle(w) \langle JJJ_f \rangle^*(sw) \quad (5.17)$$

Thus it is shown that the wavelet coefficients can also be calculated by the inverse Fourier transform from the complex product of the two Fourier transforms. The speed of the algorithm can be significantly improved with this method.

The wavelet analysis described here provides the energy of the partial signals as a function of time, but not the exact amplitude. Only under the condition that

$$\langle JJJ \rangle(w) = \frac{cW}{\sqrt{1r}} \quad (5.18)$$

the absolute values of the wavelet coefficients give the actual amplitudes of the partial signals.

The Morlet wavelet is chosen in this work as the mother wavelet $\langle JJJ_0 \rangle$. Because of its shape (a cosine multiplied by a Gaussian function), this wavelet type is particularly well suited for the analysis of wave phenomena. The Morlet wavelet is defined as follows (*Torrence and Compo, 1998*):

$$\langle JJJ_0 \rangle(\zeta) = \frac{1}{\sqrt{\pi}} \frac{e^{-f_s \zeta}}{1r} e^{-\frac{\zeta^2}{N^2}} \quad (5.19)$$

This is a dimensionless time parameter. The Morlet wavelet is normalised to 1 by the factor $1/\sqrt{\pi}$. Strictly speaking, the Morlet wavelet is not a true wavelet, because the admissibility condition (Eq. 5.14) of a wavelet is not fulfilled. In Eq. 5.18, however, it was shown that for the pure spectral decomposition of a signal, the wavelet does not have to be normalised and thus the admissibility condition does not have to be fulfilled. The factor cW from the wavelet analysis disappears. The dimensionless frequency w_0 is set to 6 in order to approximate the admissibility condition as closely as possible.

The Fourier-transformed $\langle JJJ_0 \rangle$ for the Morlet wavelet results as follows

$$\langle JJJ_0 \rangle(\zeta) = \frac{1}{\sqrt{\pi}} \frac{e^{-f_s \zeta}}{1r} e^{-\frac{\zeta^2}{N^2}} \quad (5.20)$$

The maximum of the Fourier transformed wavelet determines the Fourier frequency associated with the scale factor s . It is localised by the central frequency w . It is localised by the central frequency w_0 . Thus the scale s is related to the frequency via its reciprocal value.

Similar to the Fourier transform, the probability distribution of the wavelet spectrum of a normally distributed random variable corresponds to an χ^2 distribution with 2 Frei-degrees of fitness.

$$\frac{1/f(sT)}{2} = ? \quad P_{\chi^2_2} \quad (5.21)$$

P is again the mean Fourier spectrum. The 95% confidence interval is calculated by multiplying $0.5P$ by the 95% value of the χ^2 distribution.

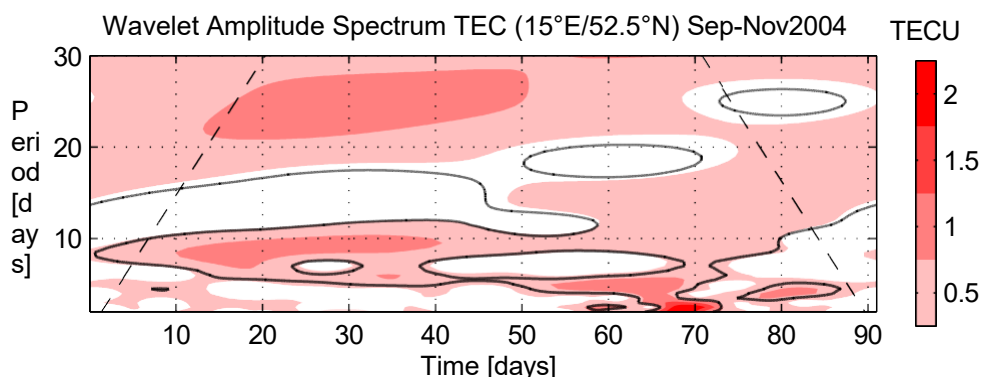


Figure 5.2: Wavelet amplitude spectrum calculated with the Morlet wavelet with $w_0 = 6$. The black solid line encloses the areas with 95% significance. The dashed lines limit the reliable range of the analysis.

Figure (5.2) shows the wavelet amplitude spectrum of the example signal for which the short-term Fourier spectrum was already shown in Fig. 5.1. In the period range between 5 and 10 days, the Fourier and wavelet spectra are almost identical. In the lower range of the spectrum, the wavelet analysis shows a clearly finer temporal resolution than the Fourier analysis. A short-term disturbance with a large amplitude, as can be caused by geomagnetic storms, can be observed in the wavelet spectrum on day 70. Also in the upper part of the wavelet spectrum, unlike the Fourier spectrum, an oscillation with a period of about 25 days can be identified, which is close to the solar rotation period.

With this example, 2 advantages of wavelet analysis over Fourier analysis could be demonstrated: the fine temporal localisation of high-frequency signal components and the better frequency determination of low-frequency signal components. A more detailed comparison of both methods is presented in section 5.2.4.

5.2.2. Cross wavelet analysis and wavelet coherence

It is also possible to perform cross-wavelet analyses of 2 time series and thus extend the idea of cross-correlation to the time-frequency representation or time-scale representation. With two time series f and their wavelet transformation $1/w f$ and $1/w a$ a cross wavelet spectrum $1/w f$ can be defined:

$$1/w f = 1/w f 1/w^*. \quad (5.22)$$

If the mother wavelet is complex, the cross spectrum can be divided into real and imaginary parts, or into amplitude and phase:

$$1/w f = L - i Q = 1/w f^{(ft)}. \quad (5.23)$$

Here $1/w f = L_2 + Q^2$ is the cross amplitude spectrum and $\angle D = \arctan(Q/L)$ is the cross phase spectrum.

In analogy to the Fourier analysis, a wavelet coherence function exists.

$$1/C_w f = \frac{\langle 1/w f \rangle}{\sqrt{\langle 1/w f 1/w f^* \rangle \langle 1/w f^* \rangle}} \quad (5.24)$$

The square brackets in this case mean to form an expected value. The expectation value is often determined in practice by smoothing in time and scale (Maraun and Kurths, 2004). A linear relationship between f and time T on the scale s is indicated in the wavelet coherence spectrum by $1/C_w f(sT) = 1$.

5.2.3. Inverse wavelet transform

In this work, wavelet analysis is not only used for spectral representation, but also for filtering localised partial signals or entire frequency bands in time and frequency and for downsampling the data. For this purpose, the filtered signal is reconstructed from the reduced spectrum with the inverse wavelet transformation.

Like the Fourier transform, the wavelet transform is an isometry on L_2 because of the Parseval relation.

$$\int f^2 = \int 1/w f^2 \quad (5.25)$$

The energy of the output signal f is equal to the energy of the wavelet transformed signal $1/w f$. The wavelet transform is therefore inverted by the adjoint operator. Thus the inverse of $1/w f$ is equal to the adjoint.

$$\langle f f \rangle = \langle 1/w f 1/w f \rangle = \langle 1/W^*(1/w f) f \rangle \quad (5.26)$$

The signal f can be reconstructed from its wavelet transform with the following equation

$$f(x) = (c_{cp})^{-1} \int_{IR}^* \frac{1}{\phi} f'(\frac{x-T}{s}) ds dT. \quad (5.27)$$

$c_{cp} := \int_{IR \setminus \{0\}} f'(\frac{x}{s}) \phi(\frac{x-T}{s}) ds$ is a wavelet dependent on the wavelets '-' and cp used.

Reconstruction factor, which must be finite and non-zero.

As the previous equation shows, the reconstructing wavelet cp does not have to be identical with the decomposing wavelet '-'. In the case of the decomposition with the Morlet wavelet, a different wavelet must even be used because the Morlet wavelet does not fulfil the admissibility condition. With the help of a slightly modified form of the Morlet wavelet

$$\phi(w) = \frac{1}{\sqrt{4\pi}} e^{-\frac{|w|}{2}}$$

however, the reconstruction can be carried out without loss. The reconstruction factor in this case is $c_{cp} = 1$.

The wavelet transform thus offers a good possibility for filtering signals. In this work, it is used to avoid the aliasing effect when downsampling the data and to filter temporally and spectrally localised partial signals. For this purpose, certain coefficients in the wavelet spectrum are set to zero and then the filtered signal is reconstructed from the modified spectrum. The filter method used can be found in *Borries and Hoffmann (2010)*.

5.2.4. Analogies and differences to short-term Fourier analysis

A striking similarity between Fourier and wavelet analysis can already be seen in their formulae. Both form the inner product of the signal and a family of analysis functions. In the case of wavelet analysis, the analysis function is a family of wavelets and in the case of Fourier analysis, a window function.

The difference between the two methods lies in the form of the analysis functions. The window function of the Fourier analysis always has the same size, independent of the frequency under investigation. In contrast, the wavelet function has time spans that are adapted to the frequency. High-frequency wavelets are narrow and low-frequency wavelets are wider. This makes wavelet analysis more suitable for resolving short-term high-frequency phenomena (*Daubechies, 1992; Barthlott, 2003*).

Another important difference between the two methods is that, in contrast to Fourier analysis, wavelet analysis uses non-stationary signals that differ in frequency and amplitude with

change over time. Because stationary signals cannot be assumed in this work, wavelet analysis is mainly used. Also, the leakage effect, which is a problem of Fourier analysis, does not occur with wavelet analysis. The advantages of wavelet analysis become clear in the comparison of the two example spectra in Fig. 5.1 and Fig. 5.2.

5.3. Frequency-wavenumber analysis

PW are known to move mainly in a zonal direction. If data such as reanalyses concerning PW are analysed, the meridional movement of the PW is neglected in most cases. For the analysis of PWTO in the TEC it is true that the direction of movement must be fully investigated, but the small meridional extent of the TEC maps does not allow reliable statements about the meridional movement of PWTO. For this reason, a 2-dimensional problem can also be assumed for this investigation. One model for the waves we are looking for is the equation for plane waves.

$$f(x, t) = A \cos(kx + wt) \quad (5.28)$$

The wave is described by the three quantities amplitude A , wave number k and frequency w . Given is a data set f with the spatial extension x and the temporal extension t . The aim is to characterise the waves by their zonal extent (wavenumber), their direction of motion and their frequency.

The method used is generally called frequency-wavenumber analysis, or FK analysis for short, because it breaks down signals according to frequency and wavenumber. It is a 2-dimensional spectral decomposition for which different methods of spectral analysis can be used. In this work, the Fourier and wavelet analyses already presented are used.

The FK analysis was already described in detail in the work of *Hayashi* (1971). The method will be briefly summarised here.

First, the data set is spectrally decomposed along the spatial dimension. The Fourier analysis yields Fourier coefficients that carry the information about amplitude and phase for each wavenumber k for each time t .

$$ff'(k, t) = ff'(k, t)^{fft} = C(k, t) - iS(k, t) \quad (5.29)$$

The cosine ($C(k, t)$) and sine components ($S(k, t)$) of the Fourier coefficients carry the information about the temporal development of the wave amplitude, except that they are spatially offset by $\pi/2$. C and S are Fourier transformed in the temporal dimension. From

the Fourier transforms \hat{C} and \hat{S} , the power spectra P_c and P_s and the cross spectrum P_{sc} are calculated.

$$P_c(k w) = \hat{C}(k w) \hat{C}(k w)^* \quad (5.30)$$

$$P_s(k w) = \hat{S}(k w) \hat{S}(k w)^* \quad (5.31)$$

$$P_{sc}(k w) = \hat{S}(k w) \hat{C}(k w)^* = L_{sc}(k w) - i Q_{sc}(k w) \quad (5.32)$$

P_c and P_s already contain the information about the wave number and the frequency of the occurring waves. The effective spectrum Q contains the decisive information about the direction of movement of the waves. For waves travelling eastwards (westwards) the effective spectrum is *positive* (*negative*) and for standing waves, which mathematically consist of 2 waves of equal strength travelling in opposite directions, $Q = 0$. The power spectrum of the wave components separated according to the direction of movement is (derived by *Hayashi*, 1971):

$$4P(k \pm W) = P_c(k w) + P_s(k w) \pm Q_{sc}(k w) \quad (5.33)$$

Eastward (westward) wave components are characterised by a positive (negative) sign. Since the standing wave is analytically created by the sum of two opposing wave components of equal size, the power spectrum of the standing wave is

$$P_{stand}(k w) = \min(P(k +w) P(k -W)) \quad (5.34)$$

The spectra of the actual eastward (westward) moving waves result from the difference of the eastward (westward) wave component (Eq. 5.33) and the standing wave component.

$$P_e(k w) = P(k +w) - 0.5P_{stand}(k w) \quad (5.35)$$

$$P_w(k w) = P(k -W) - 0.5P_{stand}(k w) \quad (5.36)$$

Stationary waves are defined by a constant amplitude and constant phase. They are described in the FK analysis by the mean values of C and S .

$$P_{stat}(k) = \overline{C(k t)}^2 + \overline{S(k t)}^2 \quad (5.37)$$

The advantages of wavelet analysis can be used in FK analysis by replacing the second Fourier analysis with wavelet analysis. Thus, the temporal occurrence of certain waves can be precisely localised.

6. TEC variations with solar origin

6.1. Introduction

While solar variation in the range of days and weeks has only a very small effect on the climatic variability of the middle and lower atmosphere, the effects in the upper atmosphere are very large and rapid. Most of the solar radiation hitting the Earth is absorbed in the upper atmosphere, causing it to heat up strongly. The upper atmosphere is generally very sensitive to variations in solar radiation. It is therefore to be expected that some PWTO observed in the ionosphere are caused by variations in solar radiation. This aspect will now be addressed.

In this chapter, solar variations with periodic occurrence and period lengths between 2 and 30 days are identified in the second section using spectral analyses of suitable measured variables. The effects on the ionosphere are presented with correlation analyses in the third section. In the fourth section, the proportion of the variability of the $f_j, \text{TEC}_{\text{rel}}$ caused by solar variation is determined and the spectra of the $f_j, \text{TEC}_{\text{rel}}$ time series are adjusted for these variations. A summary and discussion of the results is given in the fifth section.

6.2. Parameters for describing the solar influence

The radiation emitted by the sun is distributed over a wide spectral range. The short wavelengths (UV, EUV and X-rays) are important for the ionosphere (Hargreaves, 1992). They are emitted by the chromosphere and corona.

Almost continuous direct measurements of solar irradiance have only been available since the TIMED-SEE (Thermosphere Ionosphere Mesosphere Energetics and Dynamics - Solar EUV Experiment) mission, which started in 2002. As long as these measurements were not available, thermal radio emission measurements were usually used, which still serve as efficient proxies of solar radiation intensity.

Different types of radio emissions reflect different aspects of solar activity. Thermal emissions (thermal radiation, infrared radiation) are present all the time. They correspond to the temperatures of the emitting regions. Ra-diowaves with a wavelength of centimetres, which escape in the upper chromosphere, are used as a measure of the EUV radiation entering the Earth's atmosphere. The 10.7cm radio flux index (hereafter F10.7) corresponds to the spectral energy flux density averaged over the solar disk at a frequency of 2.8GHz or at a wavelength of 10.7cm (Prölss, 2004). It is an established proxy (applied e.g. in Jakowski *et al.*, 1991; Bouwer, 1992; Kane *et al.*, 1995; de Adler *et al.*, 1997; Rodger and Jarvis, 2000; Bachmann *et al.*, 2004; Floyd *et al.*, 2005; Vellante *et al.*, 2007; Oinats *et al.*, 2008; Dudok de Wit *et al.*, 2008; Hathaway, 2010), but it should be noted that the accuracy of the F10.7 is limited. The studies by Dudok de Wit *et al.* (2008) found that different indices represent variations in EUV differently. But no single index is able to satisfactorily approximate both the variability of EUV on time scales above 27 days and the relative changes in radiation on shorter time scales. They explain that no significant improvement is expected from the combination of different EUV proxies either.

The investigations in this paper use the F10.7 proxy for the analysis of the variability of solar radiation. The F10.7 is shown for the study period (2002- 2008) in Fig. 6.1 (above). In 2002, which is at solar maximum, the F10.7 values are maximum, while in 2008 the values are very low. Sunspots, which characterise solar activity, are clustered in the solar activity maximum and are rare in the solar activity minimum. 2008 is in the absolute minimum between two 11-year solar cycles (23 and 24). Hardly any sunspots occurred in this year.

To investigate solar variations with periods of several days and weeks, $f_j, F10.7_{rel}$ is introduced (calculated like f_j, TEC_{rel} in Eq. 4.13). The trend caused by the 11-year solar cycle is reduced by calculating relative differences to a running mean (mean over 27 days, black line, Fig. 6.1, above). The calculation of the $f_j, F10.7_{rel}$ serves to improve comparability with variations in the f_j, TEC_{rel} . The wavelet spectrum of $f_j, F10.7_{rel}$ clearly reflects the rotation period of the sun, which is 27 days on average. It is strongest in the years 2002-2005. The half rotation period with 13 days, e.g. in spring 2005, also appears infrequently. Significant variations with periods of less than 10 days do not occur in the $f_j, F10.7_{rel}$.

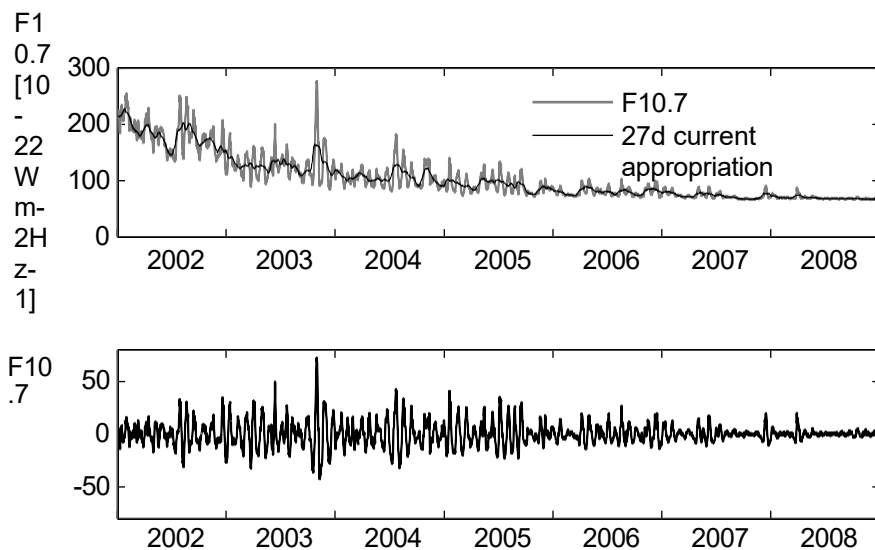


Figure 6.1: Top: 10.7cm radio flux index ($F_{10.7}$, grey line) and the 27-day running mean (black line); bottom: relative differences between $F_{10.7}$ and running mean. The lines on the time axis indicate the 01 January of the year.

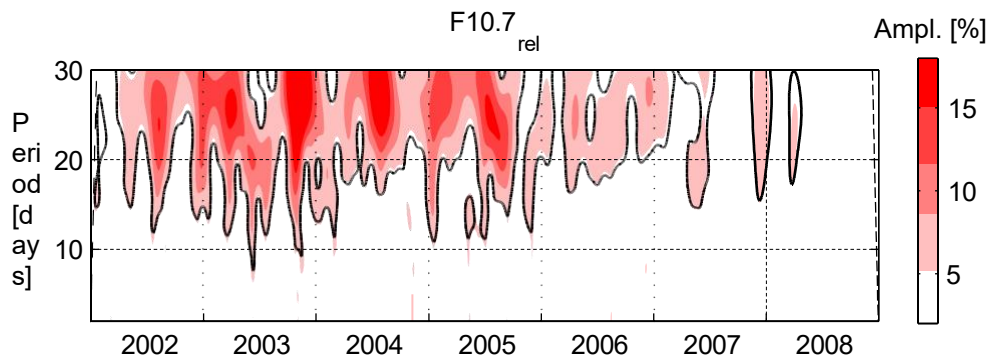


Figure 6.2: Wavelet amplitude spectrum of $f_j F_{10.7}_{\text{rel}}$. The vertical grid lines indicate the change of year (1 January).

The sun is constantly losing mass (matter). This strom of mass is called solar wind. The source of the solar wind is the hot corona of the Sun. The plasma of the corona is so hot that the sun's gravity cannot hold it. Although the origin of the solar wind is understood in principle, details about how and where the coronal gases are accelerated are not yet clear. The average speed of the solar wind is about 400km/s, but it is subject to strong fluctuations. Both the wind speed and composition change, and the solar wind carries magnetic clouds¹ and interacting regions. The wind speed is high (about 800km/s) over coronal holes and low (about 300km/s) over so-called streamers. Depending on the constellation of coronal holes, different quasi-periods of solar wind can occur near the Sun (*Song et al.*, 2009).

The solar wind is the second most important form of solar influence on the Earth's atmosphere besides radiation (*Hargreaves*, 1992). Although the solar wind does not reach the ground, its influence in the upper atmosphere is significant (*Prölss*, 2004; *Habarulema et al.*, 2009; *Juusola et al.*, 2009; *Palmroth et al.*, 2009). The solar wind couples via reconnection of the interplanetary magnetic field (IMF) with the geomagnetic field and thus into the magnetosphere. Variations in the field strength of the IMF, the wind velocity, the particle density and the dynamic pressure of the solar wind are transmitted into the magnetosphere (*Palmroth et al.*, 2009). However, the reaction of the magnetosphere to the variation of the solar wind parameters is still only partially known. Various instruments measure the solar wind, e.g. the "Solar Wind Experiment" (SWE), which is carried out on board the WIND satellite. However, as with almost every solar wind measurement, the data are not entirely complete. Mostly at extreme events, such as flares (solar flares), there are data gaps. Hourly means of the absolute wind speed are formed in preparation for the spectral analyses. With this homogeneous sampling rate, 94% of the data are available during the investigation period. To avoid edge effects in the spectral analyses, the gaps are linearly interpolated. However, the analysis results at the interpolation points are not taken into account.

The wavelet amplitude spectrum of the absolute wind speeds of the solar wind of the measured by the SWE is shown in Fig. 6.3. The times when no data are available are marked in grey.

The spectrum in Fig. 6.3 shows that the solar wind is significantly more variable than the $f_{\text{J},\text{F}10.7_{\text{rel}}}$ in the periods between 2 and 30 days. The periods of most frequent and strongest variations are harmonics of the solar rotation period with 27, 13, 9 and 7 days. For example, in 2005 a very dominant 9-day period is clearly observed. The 13-day half rotation period is also repeatedly present. In the years 2003

¹Magnetic clouds form in the solar wind when solar flares and coronal mass ejections carry material from the Sun embedded in the interplanetary magnetic field (IMF).

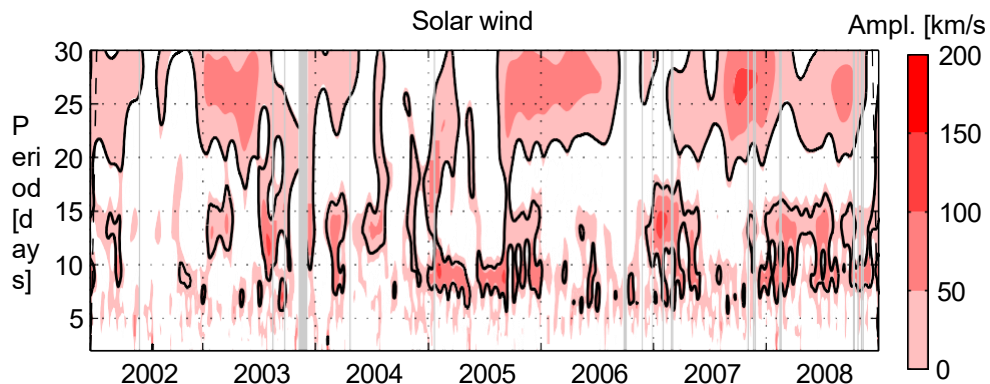


Figure 6.3: Wavelet amplitude spectrum of the solar wind (SWE absolute wind speed). Data gaps are greyed out. The vertical grid lines indicate the change of year (1 January).

and 2006, more 7-day periods can also be observed. The cause of the harmonic variations of the solar wind are corotating interactive regions (CIR) in the solar wind. CIRs are regions in which mass flows with different velocities interact. The speed of the solar wind varies depending on the conditions in the corona. As mentioned earlier, high solar wind speeds come from coronal holes and low ones from streamers. As the Sun rotates, these regions corotate and produce patterns like a rotating lawn sprinkler. When a slow stream is caught up by a fast stream, the two streams interact and can produce a shock wave. This accelerates the particles to very high speeds.

The upper atmosphere reacts to the variations of the solar wind. Various measurements (e.g. infrared energy budget of the thermosphere) were able to detect a 9-day period in the upper atmosphere in 2005 (Mlynczak *et al.*, 2008). The origin of this 9-day variation can be traced back to a quasi-periodic variation of the solar wind, which was caused by 3 sunspots (at that time offset by exactly 120°).

The solar wind has an indirect effect on the ionosphere via coupling with the geomagnetic field. In the magnetopause region, energy from the solar wind is transferred to the magnetosphere. This region determines much of the behaviour of the magnetosphere and the ionosphere at high latitudes (Hargreaves, 1992), because, as described in Chap. 2.2.3, the geomagnetic field influences the movement of ionised particles and thus modifies the electric currents of the ionosphere and the movement of the plasma.

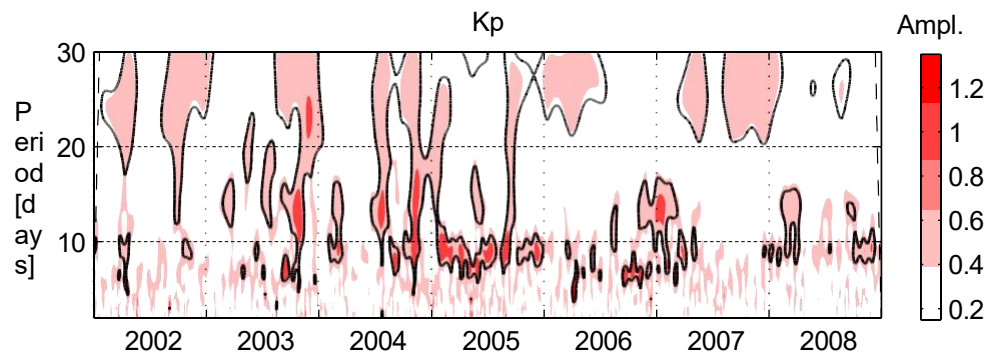


Figure 6.4: Wavelet amplitude spectrum of the Kp index. The vertical grid lines indicate the change of year (1 January).

The disturbance state of the geomagnetic field is indicated by various indices (see chapter 2.2.3). One of these is the Kp index. The Kp index describes the deviation of the magnetic field strength from the mean within 3-hour intervals measured by approx. 12 selected magnetic observatories. After local weighting and averaging, the Kp value is determined for each 3 hours of a day on a scale from 0 (very quiet) to 9 (very disturbed) (Hargreaves, 1992). The scale is quasi-logarithmic and the numerical values are further subdivided by the symbols + and .

The influence of the solar wind on the variations of the geomagnetic field can be clearly seen when comparing the wavelet amplitude spectrum of Kp (Fig. 6.4) with that of the solar wind (Fig. 6.3). Both spectra show very similar features. For example, the dominant 9-day period in 2005 appears clearly in both the solar wind and Kp.

The correlation study in Fig. 6.5 shows that the correlation coefficient between Kp and the absolute solar wind speed is 0.59 on average. The correlation is higher in the solar minimum (approx. 2006 to 2008) than in the solar maximum (approx. 2002 and 2003).

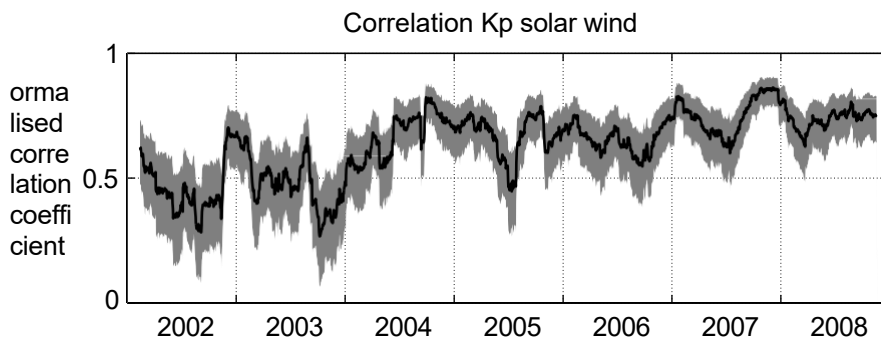


Figure 6.5: Correlation between K_p and solar wind. The correlation was calculated under a sliding window with a width of 90 days. The grey shading indicates the 95% confidence interval. The vertical grid lines indicate the change of year (1 January).

6.3. Correlation between TEC and solar parameters

The connection between TEC and the three quantities F10.7, solar wind and K_p described in the previous chapter is examined in this section. The zonal mean of $f_{j,TEC_{rel}}$ at $60^\circ N$ (here the data coverage is comparatively high) is chosen as the measure of TEC. The results of the correlation analyses are shown in Fig. 6.6. In contrast to the correlation between K_p and the solar wind, the results of which generally show high correlation values, the correlation values between $f_{j,TEC_{rel}}$ and the three variables F10.7, solar wind and K_p vary considerably.

The coefficients of the cross-correlation between $f_{j,TEC_{rel}}$ and the differential $f_{j,F10.7_{rel}}$ (Fig. 6.6, top) vary between -0.4 and 0.8 and are on average 0.3. As expected, the highest values occur during the study period in summer when solar irradiance is highest. Secondary maxima in the correlation coefficients often occur in winter (especially in the solar activity minimum). Near the equinoxes, when the TEC is climatologically greatest, the correlation with the differential F10.7 is usually low. Using the method of least squares, a model of the correlation values has been approximated (red curve in Fig. 6.6, top), which reflects the described semi-annual periodic variation of the correlation between $f_{j,TEC_{rel}}$ and F10.7. Consideration of the model of the correlation values suggests a connection to variations in neutral gas density. Due to neutral gas dynamics

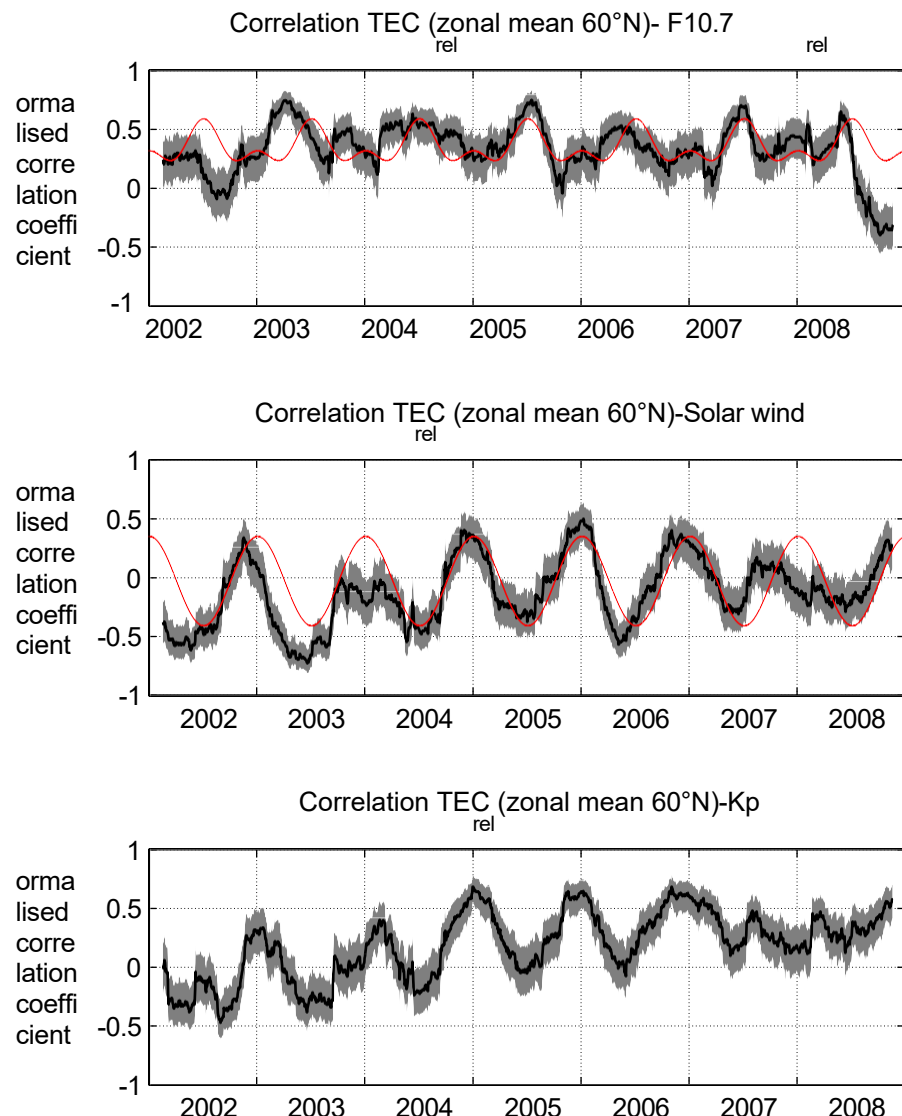


Figure 6.6.: Correlation of $f_{j,TEC_{rel}}$ (zonal mean 60° N) with $f_{j,F10.7_{rel}}$ (top), $f_{j,TEC_{rel}}$ with absolute solar wind speed (middle) and $f_{j,TEC_{rel}}$ with K_p (bottom). The correlation was calculated under the same window with a window length of 90 days. The grey shading indicates the 95% confidence interval. Red curves show the models of the correlation values determined with the method of least squares. The vertical grid lines indicate the change of year (1 January).

the neutral gas density has a similar but anti-correlated semi-annual cycle. The neutral gas density in the thermosphere is maximum at the equinoxes and minimum at the solstices. The primary maximum is in October and the primary minimum in June (e.g. Sehnal, 1987; Tawadrous, 1989). The recombination rate changes with density. The greater the density, the smaller the free path length and the greater the recombination rate, which leads to lower ionisation. In addition, the ratio [O/O₂] is small in summer (lower ionisation) and the sun is at its highest zenith at 60° N (greatest efficiency). Thus, only during a low neutral gas density in June is the variation of the TEC significantly influenced by solar radiation. The deviation of the correlation values from the model/neutral gas density observed in 2003 and 2004 could have its cause in a high number of geomagnetic storms. They cause strong changes in ionisation in the short term, while the thermosphere reacts only slowly. The connection to the thermospheric density is thus superimposed by other processes. The negative correlation in the second half of 2008 cannot be explained at present, but clarifying this observation goes beyond the aim of this work.

The cross-correlation between f_j , TEC_{rel} and the absolute wind speed of the solar wind (Fig. 6.6, centre) clearly shows an annual cycle with negative correlation in summer and positive in winter. A model of the climatological course of the correlation curve determined with the method of least squares is drawn in red in Fig. 6.6. The seasonal cycle of correlation values is most pronounced in the transition phase from solar maximum to solar minimum (2004-2006). The largest absolute correlation values are measured in 2005 and 2006. The maximum absolute correlation coefficient is 0.7. During the period of maximum correlation, greater variability of the solar wind due to CIRs is also observed (Zhang *et al.*, 2008). In the solar maximum, the correlation is low in winter and almost zero in the solar minimum. Because the solar wind couples into the magnetosphere in the polar regions, its influence becomes greater with increasing latitude. The seasonal cycle is much more pronounced near the poles and the maximum correlation values are greater than at mid-latitudes. At 80° N, a correlation coefficient of at least -0.5 is measured in each summer (no figure). Similar seasonal dependencies have been observed for electron density changes during geomagnetic storms (Förster and Jakowski, 2000). The observed seasonal cycle can be explained by the changing solar irradiance. Incoming particles of the solar wind lead to a heating of the lower thermosphere in summer. The increased temperature causes the diffusion of molecular components to higher altitudes and thus greater recombination, which explains the negative correlation values in summer. In winter, when the ratio [O/O₂] is large, the particles carried in by the solar wind can lead to an increase in ionisation. Detailed investigations are necessary to determine the actual correlations between the TEC and solar wind variations. However, these analyses are beyond the scope of this work.

Due to the high correlation between solar wind and Kp index, it is expected that the correlation between Kp and $f_{j,TEC_{rel}}$ is similar to the correlation between solar wind and $f_{j,TEC_{rel}}$. In fact, the same seasonal cycle can be observed (Fig. 6.6, below). Looking at the values more closely, it can be seen that $f_{j,TEC_{rel}}$ and Kp do not correlate in summer. The effect of the heating of the thermosphere by the particle incidence in summer thus has hardly any effect as a geomagnetic disturbance. In winter, the correlation values are positive and usually greater than the correlation values between solar wind and $f_{j,TEC_{rel}}$. This indicates that in winter the solar wind acts mainly indirectly on the ionosphere via the coupling in the geomagnetic field. However, the coupling between the geomagnetic activity and the ionosphere is very complex, which is why the correlation between $f_{j,TEC_{rel}}$ and Kp must be considered in a differentiated manner. On the one hand, geomagnetic activity is influenced by the solar wind. On the other hand, there are also interactions with the ionosphere and the neutral gas, through which atmospheric parameters can be transferred to the geomagnetic field. These interactions and the fact that the energy of the solar wind reaches the ionosphere via the magnetosphere explain the partly higher correlation values between Kp and $f_{j,TEC_{rel}}$ compared to those between the solar wind and $f_{j,TEC_{rel}}$. However, because a very strong correlation between Kp and the solar wind was shown in Fig. 6.5, the variations of Kp are attributed to the variation of the solar wind in this work.

The results shown here indicate the dominant influence of the sun on the TEC. These are confirmed by the correlation of the solar parameters mentioned with the IGS TEC data (see Fig. B.1). The solar EUV radiation is responsible for most of the TEC variations. However, the solar wind also has a considerable influence via coupling with the magnetosphere, which cannot be neglected, especially in the time scale range of 2 to 30 days. In winter, the solar wind correlates positively with TEC and negatively in summer. Besides the solar influences, there are other processes that affect the TEC in such a way that the correlation to the solar variables is reduced. One possibility for such processes could be atmospheric waves. The lower correlation values of F10.7 and solar wind in winter indicate meteorological influences.

6.4. Estimation and filtering of the solar impact

Eliminating the solar influence from the TEC signal is a complex task. On the one hand, the sun generates quasi-periodic, discontinuous variations with quite ver-

The first case is the periodic excitation of AGW by the sun (forced oscillation). The second case is the excitation of AGW by the sun (forced oscillation), which is not correlated with any solar signal (e.g. the excitation of AGW by a solar storm). For the first case, the periodic excitation by the sun (forced oscillation), the share of $f_{j,TEC_{rel}}$ - variations that correlate with solar variations will be determined and eliminated in this chapter. The second case, which can only be investigated by means of modelling, is a current and complex topic. Its investigation is beyond the scope of this paper. The effects of such events cannot be determined with the necessary accuracy at the present time.

Periodic variations in the $f_{j,F10.7_{rel}}$, solar wind and K_p are localised in time and phase using the continuous wavelet transform (CWT). The wavelet coefficients in the spectrum of the $f_{j,TEC_{rel}}$, which are located at the positions of the 95% significant wavelet coefficients of the $f_{j,F10.7_{rel}}$, solar wind and K_p , are set to zero. The wavelet spectrum of the $f_{j,TEC_{rel}}$ reduced in this way is transformed back with the inverse CWT, resulting in a filtered version of the signal ($f_{j,TEC_{rel\,filter}}$). In this way, very precisely localised signals can be eliminated from the $f_{j,TEC_{rel}}$.

For the determination of the significant oscillations in the filtered signal, white noise can no longer be assumed as the background signal. With the help of a Monte Carlo simulation, in which the described filter is applied to white noise, the new background spectrum of the filtered signal is determined. By using the adjusted background spectrum in the determination of the significance level (Eq. 5.21), significant oscillations with small amplitude are also displayed in the wavelet spectrum (see Fig. 6.7 below).

An example of a wavelet amplitude spectrum of $f_{j,TEC_{rel}}$ for the grid point 15° E/55° N is shown in Fig. 6.7 above. The spectrum clearly shows the typical 27-day solar rotation period. In January/February and November/December 2005, the 9-day period known from the solar wind is also visible. These variations no longer appear in the wavelet spectrum of the filtered $f_{j,TEC_{rel}}$ (Fig. 6.7, bottom). In the spectrum, especially the oscillations in winter and the short periods remain.

The comparison of the energy of $f_{j,TEC_{rel}}$ and $f_{j,TEC_{rel\,filter}}$ shows that on average about 50% of the energy of $f_{j,TEC_{rel}}$ is attributed to solar variations (see Fig. 6.8, above). The same analyses with the IGS-TEC maps even show an energy share of the solar oscillations that exceeds 60% (see Fig. B.2, top). However, the standard deviation of these results is larger than that of the DLR TEC map analyses). There is no significant difference between solar maximum and minimum. The separate analysis for filtering $f_{j,F10.7_{rel}}$ oscillations shows a stronger influence of the EUV during the solar maximum (Fig. 6.8, bottom left). The greater the solar activity, the stronger oscillations in the period range of PW are caused in the ionosphere by variations of the EUV radiation. The zenith angle of the sun plays an important role in the effect of EUV radiation on ionisation. The lower the zenith angle, the stronger the ionisation.

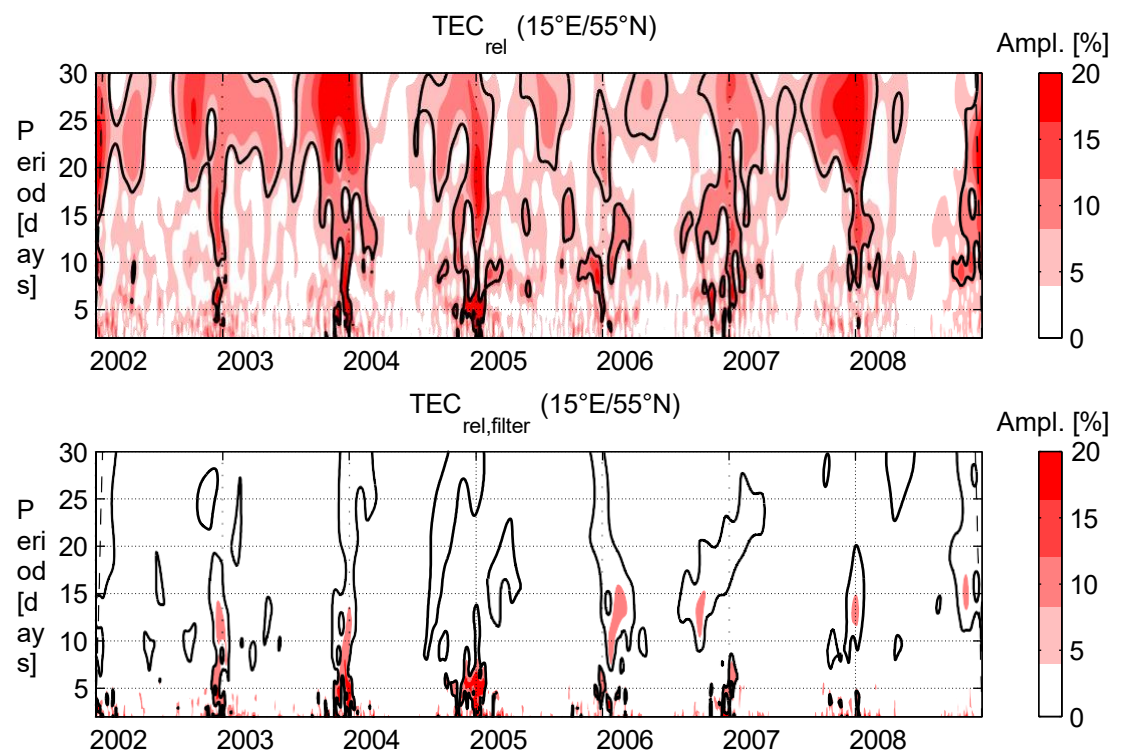


Figure 6.7.: Top: Wavelet amplitude spectrum of $f_j, \text{TEC}_{\text{rel}}$. Bottom: Wavelet spectrum of $f_j, \text{TEC}_{\text{rel}}$ adjusted for solar variations. 95% significant amplitudes are outlined with black lines. The vertical grid lines indicate the change of year (1 January).

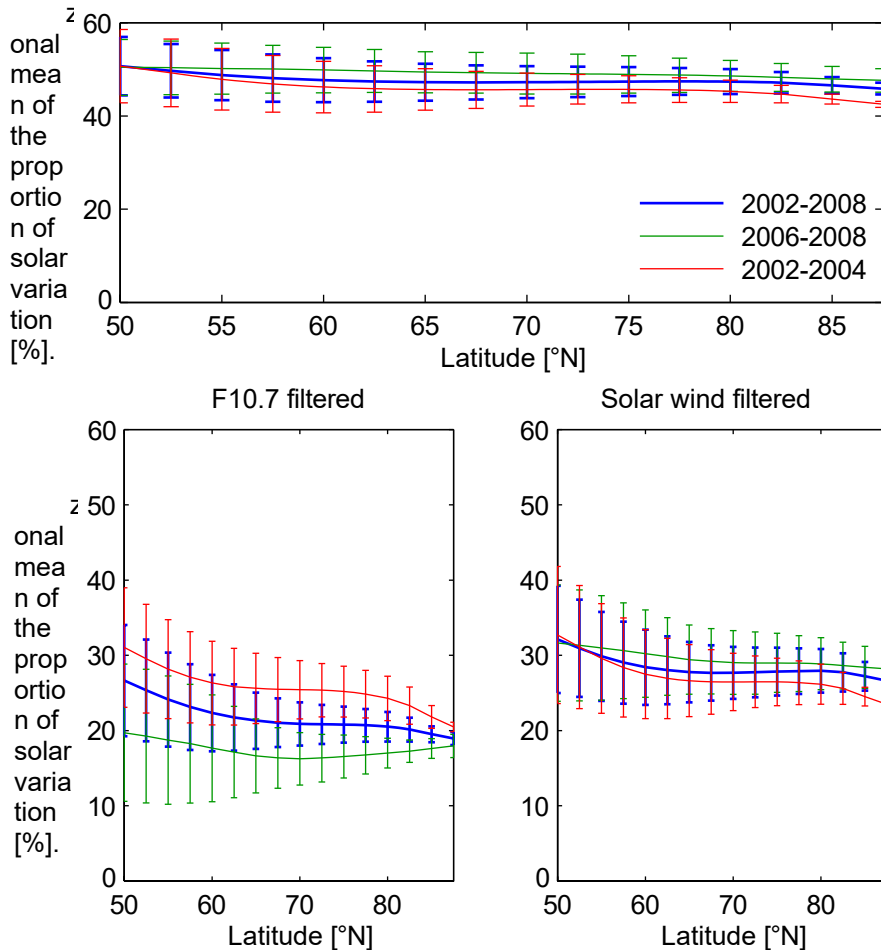


Figure 6.8: Estimation of the proportion of solar-driven variations in the $f_j, \text{TEC}_{\text{rel}}$ as a function of latitude. The zonally averaged share is shown in each case. Top: Filtering of $f_j, \text{F10.7}_{\text{rel}}$, solar wind and K_p , mean of the years 2002-2008 (blue), mean in the solar minimum 2006-2008 (green); mean in the solar maximum 2002-2004 (red); Bottom left: the filtering of the $f_j, \text{F10.7}_{\text{rel}}$ alone; Bottom right: the filtering of the solar wind alone. The standard softening is shown with bars.

ker ionising effect of EUV radiation. Accordingly, it can be seen in Fig. 6.8 (bottom left) that the proportion of EUV-controlled variations in $f_{j,TEC_{rel}}$ increases with decreasing latitude.

If only the solar wind oscillations are filtered, no significant difference between solar maximum and minimum can be seen (Fig. 6.8, bottom right). At high latitudes, the influence of the solar wind is stronger due to the incident particles in the cuspregion entering the ionosphere along the field lines. It is therefore to be expected that at high latitudes, from 60° N to the pole, a higher proportion of PWTO is excited by the solar wind. However, because the solar wind contains the 27-day period just like the F10.7, the proportion of solar wind variations in the $f_{j,TEC_{rel}}$ cannot be precisely determined. When filtering the solar wind signal, both the variations excited by the solar wind and those of the EUV are filtered. For this reason, contrary to expectations, higher values occur at mid-latitudes than at the pole when determining the proportion of solar wind variations in the $f_{j,TEC_{rel}}$ (see Fig. 6.8, bottom right). The investigation shows that, in addition to the variability of the EUV, the variation of the solar wind is also responsible for a considerable proportion of the PWTO observed in the $f_{j,TEC_{rel}}$. Both influencing variables together cause approximately the solar wind variation. Both influencing variables together cause about half (up to 40-60%) of the energy of the PWTO in the $f_{j,TEC_{rel}}$.

Finally, it is pointed out once again that $f_{j,TEC_{rel}}$ is already a filtered signal. The values determined here only describe the proportion of solar-controlled PWTO, not the proportion of solar-controlled TEC variation. With simple means, such as multiple regression, more than 98% of the TEC can be represented as a function of the solar flux (e.g. F10.7) and the solar wind. This shows that the share of PWTO without solar origin in the total variation of the TEC is very small.

Furthermore, it must be taken into account that the filter method used is "greedy". I.e. all variations of the $f_{j,TEC_{rel}}$, which occur at the same time and with the same properties as solar variations, are eliminated, although it cannot be determined with certainty whether they are the trigger for the $f_{j,TEC_{rel}}$ variation. For this reason, it must be emphasised that up to 60% of the $f_{j,TEC_{rel}}$ variations have a solar origin.

Another weakness of the method is the data used. Since the solar wind data are not complete and the F10.7 is only a relatively rough proxy of the solar EUV radiation, it is possible that solar-driven variations are still included in the filtered signal. This error influence is assumed to be small.

6.5 Summary and discussion

In this chapter, the clear correlation of TEC with solar variability has been demonstrated. The strong influence of the variation of the EUV on the variability of the TEC in the period range of approx. 27 days has been known for a long time (e.g. *Smith and Gottlieb*, 1975; *Jakowski et al.*, 1991; *Kane et al.*, 1995) and is still often a topic of discussion today (*Oinats et al.*, 2008). In the present work, the influence of EUV radiation on the ionosphere in the peri-ode range of 2-30 days was investigated by means of a correlation study between differential TEC and differential F10.7. A high correlation is confirmed by the cross correlation (correlation coefficient up to 0.8).

The influence of the solar wind with a time scale greater than 1 day has not received much attention until recently. It was not until 2008 that the first measurements were published describing a 9-day period in the upper atmosphere induced by the solar wind (*Mlynczak et al.*, 2008). Shortly afterwards, the first correlations between solar wind measurements and TEC appeared (*Lei et al.*, 2008).

Examining the correlations with a running window reveals a seasonal dependence of the influence of solar wind and EUV on the TEC. The solar influence is greatest in summer and least at the equinoxes. This seasonal correlation is attributed to the variation of the thermospheric density, which affects the recombination rate. In winter, the correlation to the differential F10.7 and solar wind is lower than in summer. Meteorological influences, which are examined in more detail in the following chapters, may be the cause of the reduced correlation in winter. Investigation of the correlation of TEC and EUV radiation during a longer period is suggested for future work to statistically substantiate the results obtained here. An improvement is also expected by using EUV measurements instead of the F10.7 proxy.

The oscillations of the $f_{\text{J}}\text{TEC}_{\text{rel}}$ in the periodic range of PW, which are caused by quasi-periodic variations of the solar wind or quasi-periodic occurrence of geomagnetic disturbances (which are mostly directly related to the solar wind variations) or by the variation of the incident EUV radiation, could be separated, estimated and minimised. For this purpose, wavelet transforms were used to localise the solar-driven PWTO in the spectra of solar wind, K_p and $f_{\text{J}}\text{F10.7}_{\text{rel}}$ and to eliminate them in the spectra of the relative differential TEC. This approach, which is new in the context of PWTO analysis, is mathematically motivated but ignores physical relationships and may delete more signal components than necessary. Because no mature physical method could be developed with the current state of research, this method was chosen as the best variant.

The comparison between the relative differential TEC and its filtered signal has shown that on average up to 50% of PWTO are sun-driven. A large part of the iono-

spherical PWTO are thus caused by variations in the incident EUV radiation or by variations in the solar wind (e.g. in wind strength or pressure). While the variations of the EUV radiation have a direct impact on the production rate, the solar wind variations are transmitted indirectly through the coupling of the IMF with the geomagnetic field and the magnetosphere or the heating of the lower thermosphere up to the ionosphere. Similar estimates of the influence of geomagnetic activity were also obtained in Xiong *et al.* (2006) and Forbes *et al.* (2000). Based on a case study, it was determined in Xiong *et al.* (2006) that 30-50% of the 5-, 10- and 13.5-day periods observed in the critical frequency of the F2 layer f_{oF} are due to variations in geomagnetic intensity. In Forbes *et al.* (2000), a variability of the maximum electron density $N_{\text{m}}(\text{F})$ (in the period range of 2 to 30 days) at geomagnetically disturbed times of about 45% was found.

When evaluating the results obtained here and also for the further analyses, it should be noted that the filter method used only eliminates periodic signals and does not take into account non-periodic signals, such as those caused by geomagnetic storms. In order to filter these TEC variations, they would first have to be modelled. This is a great challenge because of the different effects of different storms in the ionosphere. A breadth of observations and descriptions of geomagnetic storms exists (Buonsanto, 1999; Förster and Jakowski, 2000; Afraimovich *et al.*, 2001; Baran *et al.*, 2001; Cander and Mihajlovic, 2005), but adequate models are not yet available for the application presented here. Since this work focuses on periodic effects, the aperiodic influence of the sun should remain untouched.

7. Characteristic properties of planetary wave signatures in the ionosphere

7.1. Introduction

After the solar influence was largely eliminated from the f_j, TEC_{rel} signal in the previous chapter, ionospheric PWTO are to be characterised in this chapter on the basis of their wavenumber, direction of movement, period duration and strength (amplitude). These parameters are derived from the f_j, TEC_{rell} filter maps. Due to their spatial and temporal data coverage, the TEC maps are currently the only data set that allows such an analysis. Other data sets, such as measurements from ionosondes and magnetometers, do not offer comparable spatial coverage and consistency. However, it is not yet possible to explain a valid climatology of the PWTO even on the basis of the available DLR TEC maps. The investigation period of 7 years (2002 to 2008) is relatively short in order to be able to precisely record the occurring spectrum of the PWTO. Nevertheless, a first impression of the PWTO's climatology can be given.

In the following, the seasonal dependence of the PWTO occurrence in the mid-latitudes (section 7.2), the latitudinal dependence of the PWTO in the Northern Hemisphere between 50° N and the North Pole (section 7.3) and the binding to the geomagnetic field are investigated (section 7.4). The results are based on the wavelet FK analysis performed for all standing and travelling waves with wavenumbers 1 to 5 and the zonal mean. A summary and discussion of the results is given in section 7.5.

7.2. Properties of the signatures of planetary waves in the mid-latitudes

In this section, the filtered $f_{j,\text{TEC}_{\text{rell}}}$ filter data (see Chapter 6) of the mid-latitudes are systematically examined after the appearance of the PWTO in order to detect its typical properties. The data on the latitude circle 55° N serve as a reference for the investigation. The 95% significant amplitudes in the wavelet spectrum mark the PWTO.

In order to statistically record the PWTO, the wavelet spectrum is divided into different period classes: 2-4, 5-7, 8-12, 13-18, 19-25, 26-35 days. For each day, it is checked whether significant PWTO occur in the individual period classes. If a significant PWTO occurs, the day is marked with 1, otherwise with 0. Related days marked with 1 within a class are counted as one PWTO. In the entire study period 2002-2008, a total of 383 PWTO occur in the mid-latitudes. A differentiated examination of the frequency of occurrence of PWTOs (Fig. 7.1) separated according to their wave number makes it clear that by far the most PWTOs occur in the zonal mean (143 in total). This observation contrasts with the PW activity in the middle atmosphere, where the oscillations of the zonal mean are not as frequent (see Fig. A.1). With a wave number greater than or equal to one, between 72 and 13 observed PWTOs occur during the study period, depending on the wave number. The differentiation according to the period bands shows that PWTO with periods between 5 and 25 days occur more frequently than the quasi 2-day and quasi 30-day waves. The quasi 5-day wave (period between 5 and 7 days) and the quasi 10-day wave (period between 8 and 12 days) are the most frequent. Overall, they describe almost half (number 182 PWTO) of the PWTO occurring in the $f_{j,\text{TEC}_{\text{rell}}}$ filter.

In the following, we aim to identify the dominant PWTOs by their mean amplitudes. und saisonale Auftrittsabhängigkeit zu charakterisieren. Um die saisonale Abhängigkeit des Auftritts der PWTO abzubilden, werden die Ergebnisse der Wavelet-FK-Analyse für jede Jahreszeit (Winter (W): Dez-Feb; Frühjahr (F): Mär-Mai; Sommer (S): Jun-Aug; Herbst (H): Sep-Nov) separat betrachtet. Die 95% signifikanten Amplituden ($f^{..95}$) werden quadriert und über der Translation T integriert. Die Wurzel des nur noch von der Skala s abhängigen Ergebnisses wird als RMS bezeichnet.

/-

$$\text{RMS}(s) = \sqrt{\int f(s, T)^2 dT} \quad (7.1)$$

For the signal f , the $f_{j,\text{TEC}_{\text{rell}}}$ filter is used. Standing and travelling waves are analysed separately. Stationary waves are not considered in this work for two reasons. Firstly, in the case that stationary PWTO are observed in the TEC, in the first instance they are

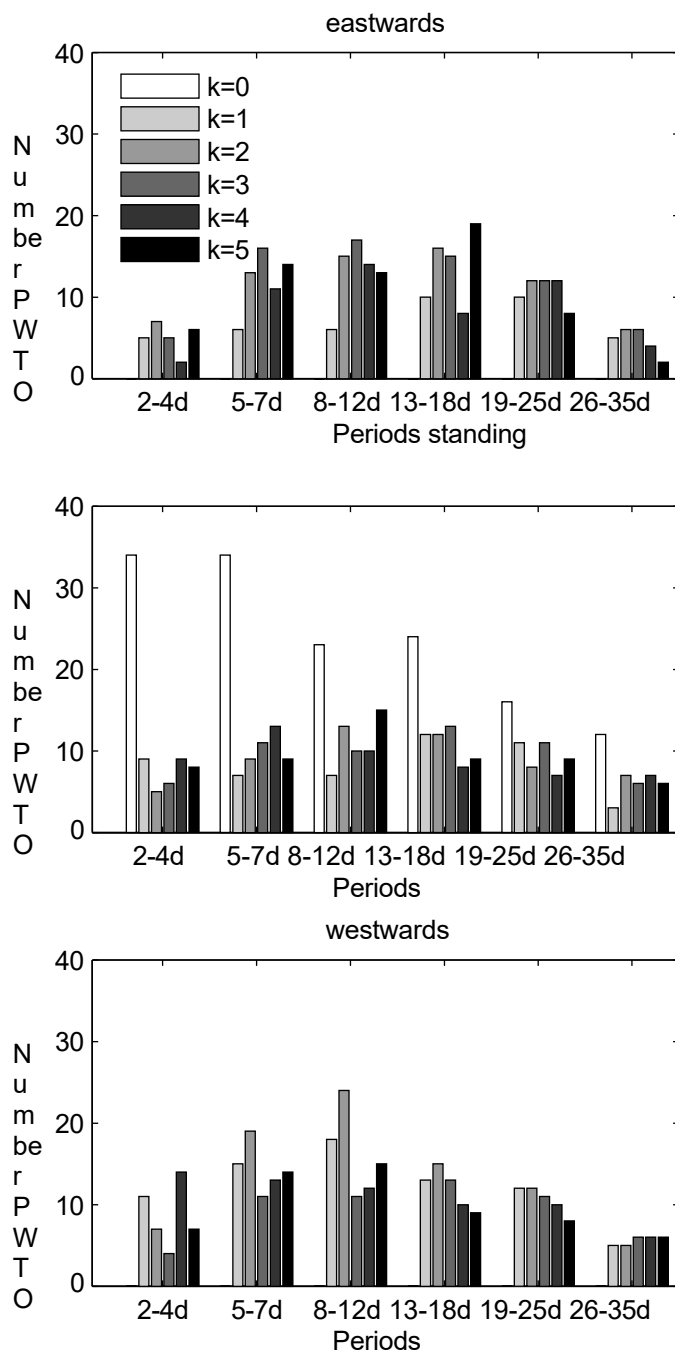


Figure 7.1: Number of observed PWTO in f_J , TEC_{rell} filter in 55° N, 2002-2008, differentiated by wave number and period class. Top: eastward moving PWTO; middle: stationary PWTO; bottom: westward moving PWTO. The grey values of the columns mark the wave number.

line to assume differences between the geomagnetic field lines to the geographic system. Secondly, stationary components are cancelled out by using the relative differential TEC.

Figure 7.2 shows the RMS amplitude spectra of the oscillations of the zonal mean (wavenumber 0, top left), as well as the standing waves with wavenumbers 1 to 5 depending on the season. Each graph shows separately the analysis results of one wavenumber and the zonal mean, respectively. It must be noted that each graph has a different grey scale with logarithmic division. The RMS amplitudes of the variations of the zonal mean are maximum. Thus, the PWTO are dominant in the zonal mean both in the frequency of their occurrence (see Fig. 7.1) and in their amplitude. As the wavenumber of the PWTO increases, the RMS amplitudes become smaller. Fig. 7.2 clearly shows a seasonal cycle of standing waves with maximum RMS amplitudes in winter and an absolute minimum of wave activity in summer.

Maximum for all wave numbers is the 2-day oscillation. It is maximum for the zonal mean with an RMS amplitude of 11%. While the quasi 2-day wave is more frequent in the zonal mean, it is less frequent for wave numbers 1 to 5 (but with very large amplitudes). Its maximum amplitudes are observed in the $f_{j,TEC_{rell}}$ filter in winter. In the variations of the zonal mean (Fig. 7.2, top left), a PWTO with the period of 5 days is also particularly prominent. With an RMS amplitude of 6.4%, it is the second strongest PWTO after the 2-day PWTO. Oscillations in the zonal mean with periods between 4 and 7 days (quasi 5-day oscillation) occur in almost every winter between 2002 and 2008 and thus belong to the typical PWTO of the zonal mean. The strongest and longest quasi-5-day oscillation was in December 2004 to January 2005 with an amplitude of up to 19% in the $f_{j,TEC_{rell}}$ filter (not shown here). In addition, PWTOs occur in the zonal mean with a wide variety of periods between 2 and 20 days. Another common representative is the 13-day PWTO. It can be observed throughout the year, with the maximum RMS amplitude in winter.

PWTOs with wavenumber 1 (Fig. 7.2, top right) occur mainly in winter. Typical representatives are the quasi 5-day wave, the quasi 10-day wave and the quasi 16-day wave. During the study period, standing waves with periods between 4 and 7 days can be observed in four winters and in five winters with periods between 8 and 12 days. In six winters, periods between 13 and 25 days occur. However, the PWTO activity of the standing wave with wave number 1 is not only limited to winter. Individual weaker events can also be observed at other times of the year. Above all, the quasi-16-day wave can be observed throughout the year.

PWTO with wave number 2, standing (Fig. 7.2 centre left), occur mainly from autumn to spring, with their strongest expression in autumn and winter. Quasi-5-day waves are particularly pronounced and relatively frequent, occurring in six winters with an RMS amplitude of 1%. Another typical PWTO of wave number 2,

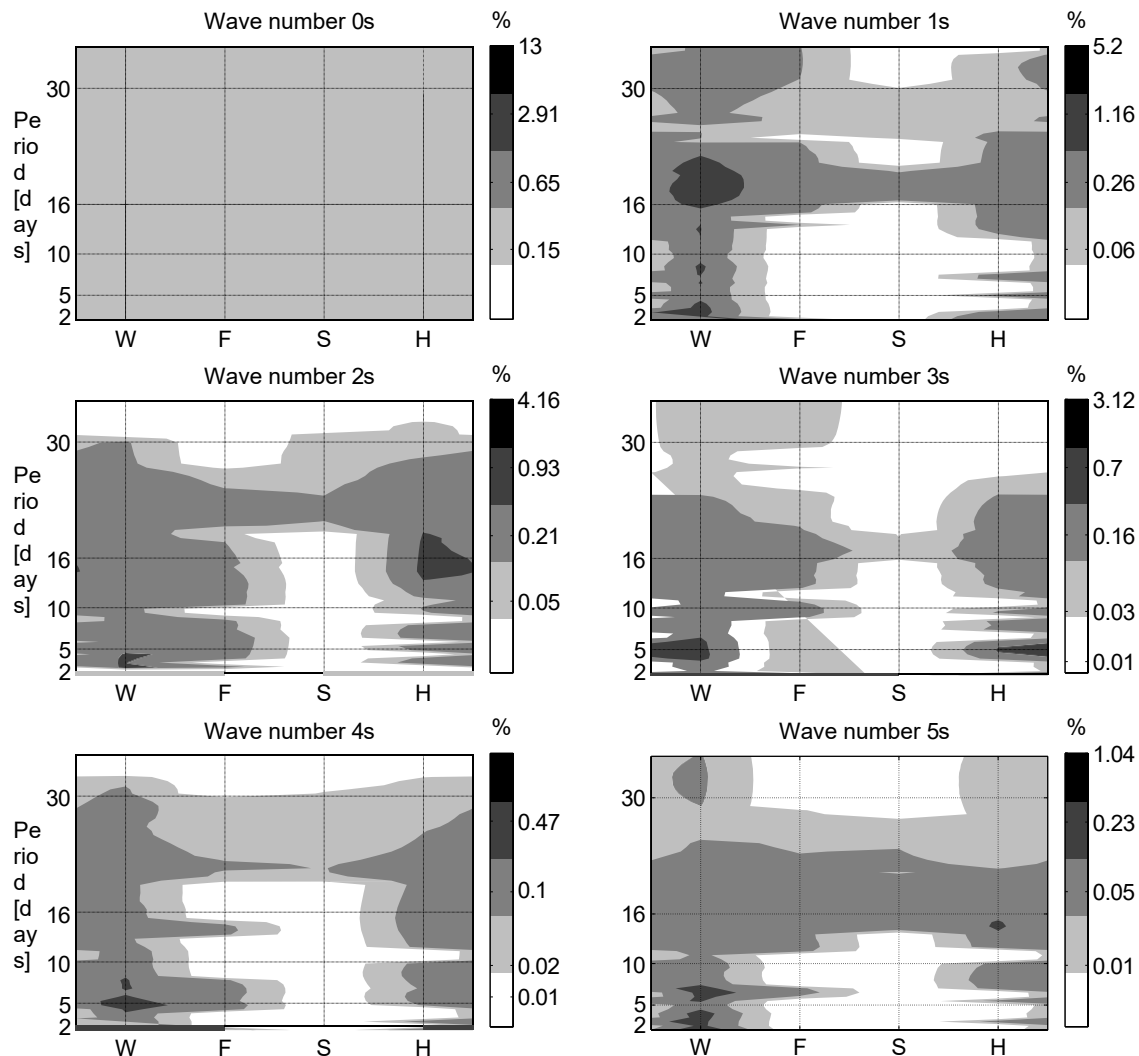


Figure 7.2: RMS of the amplitude of the standing waves of different wave numbers on 55° N observed in the $f_{\text{J}}\text{TEC}_{\text{ell}}$ filter (2002-2008) depending on the season (W: winter, F: spring, S: summer, H: autumn). The amplitude in % refers to the percentage deviation from the 27-day median.

is the quasi-16-day wave. It occurs every year during the study period (in autumn and winter), with an RMS amplitude of 1.2%.

The wave phenomena with wave number 3 (Fig. 7.2, centre right) occur mainly in autumn and winter. The PWTO with wave number 3 also have the greatest amplitude with a quasi-period of 5 days. These 5-day waves occur almost every winter in the study period (with the exception of 2006/2007) with an RMS amplitude of 1.1%. The quasi 16-day period of the standing PWTO (wave number 3) is also very frequent.

The PWTO with wave number 4 (Fig. 7.2, bottom left) also clearly show a stronger appearance in winter. The strongest PWTO is the quasi-10-day wave (0.4% RMS amplitude). In the period with higher solar activity (2002-2006) the amplitudes are somewhat stronger than in the solar minimum. The quasi-16-day wave (0.3% RMS amplitude) occurs twice with significant amplitude in the period under study. The event in autumn had a significantly larger amplitude (not shown here). However, it can also be observed in two other winters, which is why it should be counted among the typical PWTO.

The PWTO with wavenumber 5 in the f_j, TEC_{rell} filter (Fig. 7.2 bottom right) have the lowest activity compared to the PWTO of wavenumbers 0 to 4. In the solar maximum 2002- 2005 no PWTO with wavenumber 5 are observed. Between 2006 and 2008, some quasi-16-day waves occur, mainly in autumn.

The analysis results of the travelling waves are summarised in Fig. 7.3. The RMS amplitudes of the travelling waves on 55° N are shown as a function of the wave number, the direction of movement, the period length and the seasonal occurrence. The wave numbers marked with "w" indicate a westward movement and the wave numbers marked with "e" indicate an eastward movement. For better comparability, the grey value scales correspond to those used for the standing waves.

The comparison of Fig. 7.2 and 7.3 shows at first glance that the RMS amplitudes of the travelling PWTO are of the same order of magnitude, but generally somewhat smaller than those of the standing PWTO. The PWTO observed in the f_j, TEC_{rell} filter thus seem to have more of a local pulsating character, like standing waves. Nevertheless, the RMS amplitudes of the travelling PWTO in Fig. 7.3 show that these phenomena cannot be neglected either. The RMS amplitudes of the travelling PWTO are between 1.6% for wavenumber 1 westward and 0.3% for wavenumber 5 westward.

As is already known from the standing PWTO, the activity of the migrating PWTO is also subject to an annual cycle with the maximum in winter and the minimum in summer. The decrease in RMS amplitude with shorter wavelengths, which is known from standing waves, can also be observed in migrating PWTO.

Of all the migrating PWTOs, the westward-migrating PWTOs with wave number 1 (Fig. 7.3, top left) dominate with a maximum RMS amplitude of the quasi 16-day wave

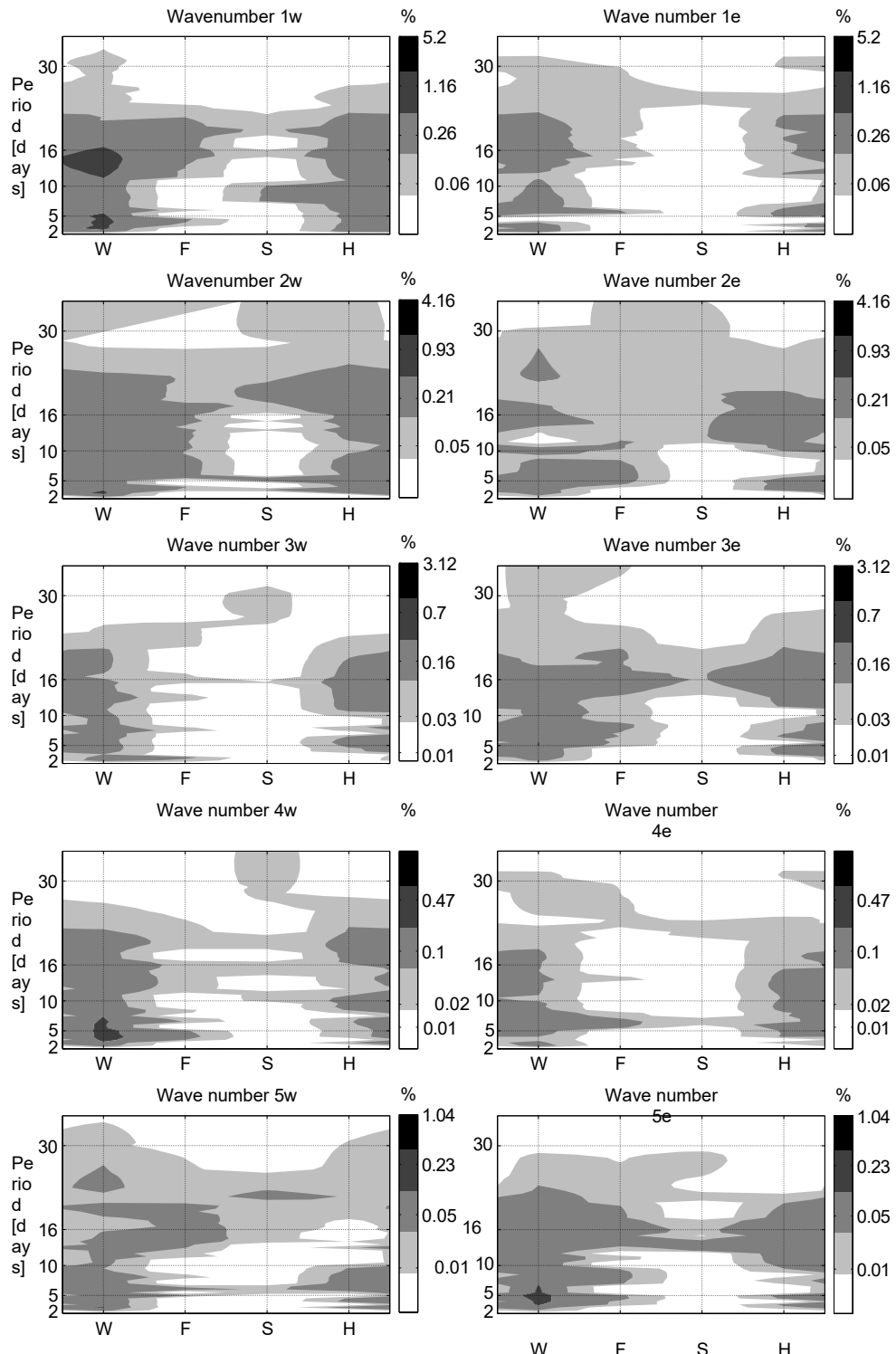


Figure 7.3: RMS of the amplitude of the travelling waves at 55° N observed in the f_j , TEC_{rell} filter (2002-2008) during the different seasons.

DLR - FB-2013-23



of 1.6%. The quasi-16-day wave is very common. It occurs every winter.

PWTO with wavenumber 2 are mainly observed with the quasi-periods of 5, 10 and 16 days. The quasi 16-day wave is the most frequent. In autumn, the eastward-moving waves dominate and in winter the westward-moving ones. Eastward- and westward-migrating PWTO are similarly pronounced. Their maximum RMS amplitudes are 1% for the quasi-5- and 16-day waves. The same typical periods were also observed for the standing PWTO with wave number 2. A correlation is obvious. Some PWTO, such as the quasi-16-day wave, which was very strong in October 2006, appear at the same time both as a standing wave and as an eastward-moving wave. In each case, both waves have similar amplitudes. It is possible that a change in the shape of the standing PWTO leads to this analysis result.

The PWTOs with wave number 3 are dominated by the eastward-migrating PWTOs. They occur preferentially with quasi-periods of 5 and 16 days. The appearance of the migrating PWTO with wave number 3 also seems to be related to that of the stationary PWTO with wave number 3, which are mostly observed simultaneously or consecutively. The RMS amplitudes of the eastward moving wave 3 reach up to 0.7% for the quasi-5-day waves.

With wave number 4, strong westward-moving waves with a 5-day period occur. The RMS amplitudes of 0.6% are larger than the RMS amplitudes of the standing PWTO with wave number 4. PWTO with wave number 5 are more pronounced as eastward-moving waves, whereby their RMS amplitude is as large as that of standing wave 5.

As already mentioned, stationary and travelling PWTO with identical wavenumber and period often occur simultaneously or consecutively, whereby it is assumed that they describe the same phenomenon. In addition, it is also observed that PWTO with the same period but different wavenumbers occur in the same period, at the same time or in direct succession. For example, between December 2005 and January 2006, a strong quasi-16-day oscillation is observed both in the zonal mean and with wave numbers 1, 2, 4 (not shown here). First (at the turn of the year) the particularly strong wave 2 appears, then (in January) wave 1 moves westwards and finally (end of January/beginning of February) the oscillation of the zonal mean. This shows that PWTOs occurring in groups probably have the same origin. The different wave numbers can be caused by interaction with other waves or the breaking of the waves.

The results of the analysis of the IGS TEC maps (Figs. B.3, B.4 and B.5) show a similar climatology of PWTO in the ionosphere as the DLR TEC maps, but they are not quite identical. The magnitude of the RMS amplitudes in the IGS maps is the same as determined in the DLR maps. In addition, the accumulation of PWTO with shorter periods is confirmed by the IGS maps and also the seasonal dependency of the PWTO is shown.

is comparable. For the larger wavenumbers ($k \geq 3$) the IGS maps show

However, somewhat smaller RMS amplitudes were determined than in the DLR maps. The quasi 5-day wave also occurs frequently in the IGS maps, but does not appear as dominant as in the DLR maps.

If the observations of the ionospheric PWTO are compared with the stratospheric PW activity in the study period (e.g. with zonal wind data at 10hPa, 55° N, see Fig. A.1, A.2 and A.3 in the appendix), clear differences in the dominant periods can be observed. While the PWTO with the smaller periods tend to dominate in the ionosphere, the PW with the larger periods (period duration > 5 days) are stronger in the stratosphere. The zonal mean oscillations that dominate in the ionosphere are also not comparable with the zonal mean oscillations that are only weakly pronounced in the stratosphere.

7.3. The latitude dependence of planetary wave signatures

In the previous section, the analyses were restricted to the latitude circle 55° N. The extent to which the occurrence and amplitudes of PWTO depend on latitude will be investigated in the following. The analyses are limited to the winter months, December to February, because the most and strongest PWTO are observed in this period (see section 7.2), and to standing waves because these PW- TO in the $f_j, \text{TEC}_{\text{rell}}$ filter describe the largest proportion of the variation.

The RMS amplitudes (see Eq. 7.1) of the standing PWTO in winter are plotted against their period and latitude in Fig. 7.4. It can be clearly seen that the PWTO occur preferentially at certain latitudes depending on their wave number. The 5-day oscillation of the zonal mean is strongest near the North Pole. When the data coverage in Fig. 4.2 is considered, the high proportion of variations of the zonal mean in the immediate vicinity of the pole is not surprising. The map grid points are close together in this area, and the data coverage is thin in this map region, so that measured values near the pole affect all grid points larger than 85° N almost uniformly. The PWTOs of wavenumber 1 have the largest RMS amplitudes at 80° N. They are not, however, dependent on the grid points. However, they are not restricted to the high latitudes, but have a second, somewhat smaller activity maximum in the mid-latitudes, where the centre of activity appears to be outside the TEC map region. With increasing wavenumber, the centres of activity of the PWTO appear to shift from the high latitudes towards the mid-latitudes. The PWTO of wavenumber 2 have their maximum between 70 and 80° N and a secondary maximum in the mid-latitudes outside the map region. The PWTO of wave number 3 have a clear centre of activity between 55 and 65° N. The activity of the

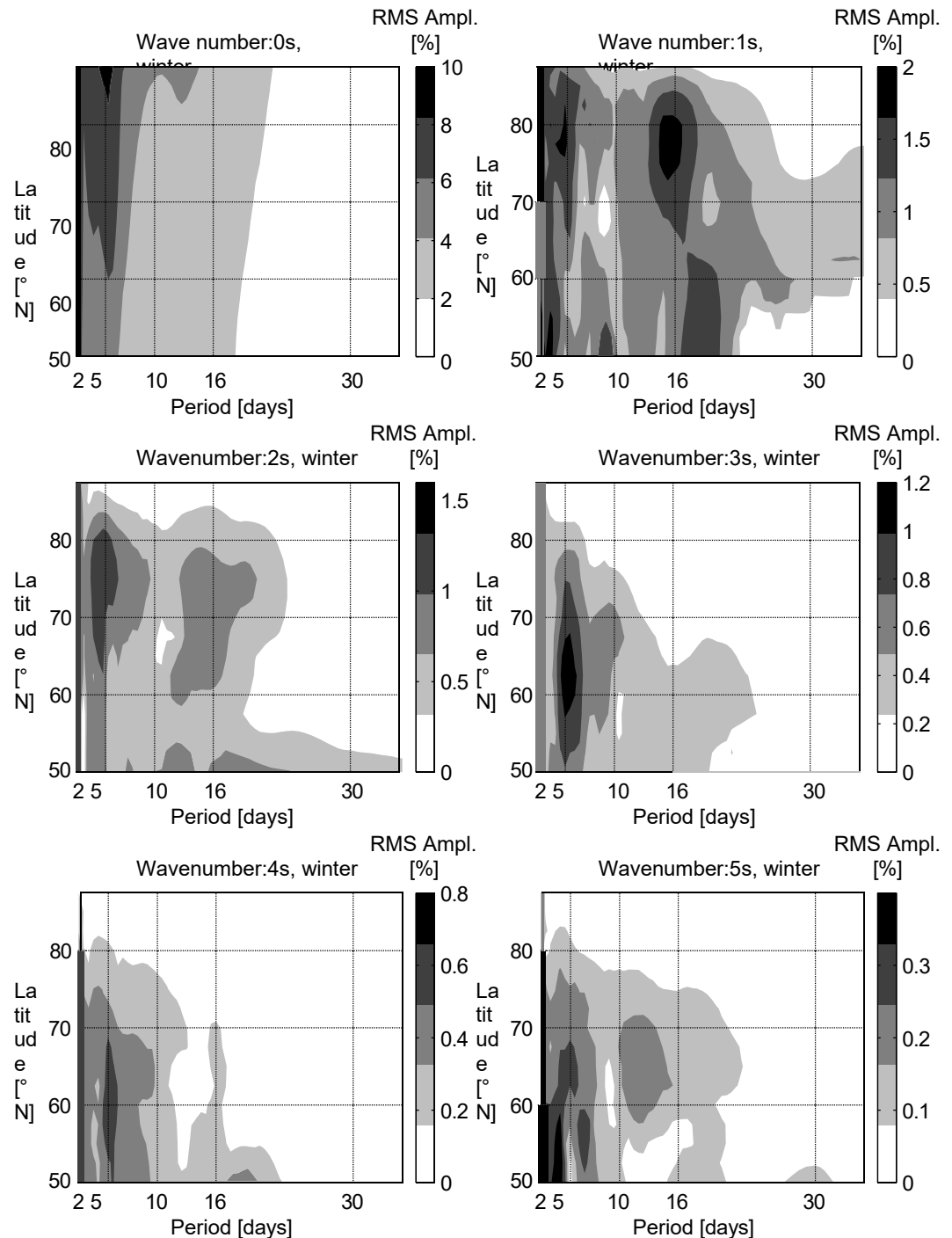


Figure 7.4: RMS amplitude of standing PWTO in the winter months December–February, 2002–2008, as a function of latitude.

PWTO of wavenumbers 4 and 5 is greatest between 50 and 70° N, with individual PWTO being maximum between 60 and 70° N and others being maximum at mid-latitudes, probably outside the map area.

From the wavenumber and the latitude, the zonal wavelength of the PWTO can be determined. The typical wavelengths of the PWTO are:

- ↗ Wave number k=1 (maximum at 60-80° N): A C:: 6950km Wave
- ↗ number k=2 (maximum at 70-80° N): A = 3475 - 6845km
- ↗ Wave number k=3 (maximum at 55-65° N): A = 5640 -
- ↗ 7650km Wave number k=4 (maximum at 50-70° N): A = 340
- ↗ - 6431km Wave number k=5 (maximum at 50-55° N): A = 736-
- ↗ C:: 5144km

Roughly speaking, the wavelengths of the PWTOs with different wavenumbers are therefore similar.

The analyses of the IGS maps (see Fig. B.6) provide a similar picture of the latitudinal dependence of PWTO in the ionosphere as the DLR maps. Nevertheless, a significant difference is found. In contrast to the DLR TEC maps, the IGS TEC maps clearly show a maximum of wave 1 between 50 and 60° N. This difference between the TEC maps and the DLR TEC maps is not significant. This difference in the TEC maps cannot be explained, because the active regions of the other PWTOs with wave numbers 2-5 match. The actual geographical location of the PWTO with wave number 1 in the ionosphere therefore remains unresolved and can only be clarified by additional observations/data sources.

The comparison with the PW activity in the stratosphere (using the example of the zonal wind in 10hPa, see Fig. A.4) shows that the strongest wave activities occur there (limited to the study area 50-90° N and the study period 2002-2008) at similar latitudes as in the ionosphere. There are agreements for all wave numbers greater than 1. The agreements are particularly clear for wave number 2, which is strongest between 70 and 80° N, and wave number 3, which is strongest at approx. 60° N. Thus, although the observed periods of PWTO differ from those of PW in the zonal wind (10hPa), the regions of strongest activity of the waves nevertheless coincide. The activity centres of the PWTO with wave numbers 0 and 1 differ from those of the stratospheric PW. The analysis describes the maximum variation of the zonal mean in the stratosphere between 60 and 80° N. Stratospheric wave 1 is strongest in the immediate vicinity of the pole. This wave 1 at the pole is caused by the displacement of the polar vortex from the north pole. A second maximum of stratospheric wave 1 is located at about 60° N. Although the DLR TEC maps show the maximum of wave 1 at approx. 80° N, the IGS TEC maps show a maximum of the

Wave 1 displayed in the same geographical region where stratospheric PW with wave number 1 are also maximum.

7.4. Discussion of the influence of the geomagnetic field

Although there are some similarities between the ionospheric PWTO and the PW of the middle atmosphere, it must be investigated whether there are other causes for these variations. It is often discussed whether the PWTO observed in the ionosphere may also be caused in situ, by solar-driven quasi-periodic variations of the geomagnetic field or EUV radiation from the Sun (e.g. *Forbes et al.*, 2000; *Altadill et al.*, 2001, 2003; *Laštovička*, 2006; *Rishbeth*, 2006; *Xiong et al.*, 2006). These two influences were already minimised by the use of the $f_{j,TEC_{rell}}$ filter. However, as already explained in chapter 6, not all solar and geomagnetic influences on the TEC can be excluded.

The question of the origin of the PWTO will be examined in more detail in this section of the paper with the help of a new approach. The approach is based on the assumption that PWTO triggered by atmospheric PW centre around the geographic pole (like PW), while PWTO formed in situ or by variations of the geomagnetic field move around the geomagnetic pole (due to the binding of the plasma to the geomagnetic field).

To study this question, a new map grid is introduced that is adapted to the field lines of the geomagnetic field. The new grid is centred around the geomagnetic south pole, which is geographically located at about 114° W/ 83° N (as of 2005, the position can change by a few minutes of arc within a year), and extends to 60° Sgeomagnetisch. The grid size of 2.5° / 7.5° (f_j ,longitude/ f_j ,latitude) is adapted to that of the geo-graphical TEC map grid (Fig. 7.5, dark grey lines). The geomagnetic coordinate system used is a modified apex coordinate system developed by *Richmond* (1995). The $f_{j,TEC_{rell}}$ filter data are transferred from the geographic to the geomagnetic grid with linear interpolation. The two map grids are shown in Fig. 7.5 for comparison. PWTO analyses are carried out on the latitude circle 70° S of the geomagnetic grid and compared with the results of the geographic grid. This region is particularly suitable because the data coverage is relatively uniform (see Fig. 4.2). Due to the increased PWTO activity during the winter months, the analyses are limited to the months of December to February. Furthermore, the analyses are limited to wave numbers 1 to 3 because, as shown in the previous section (section 7.3), only these are dominant at high latitudes.

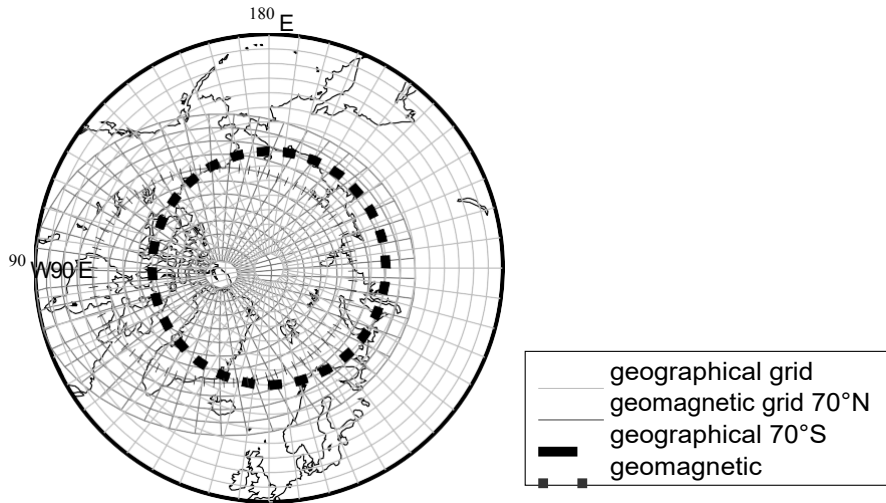


Figure 7.5: Map grid of the TEC maps. Light grey: geographic grid; Dark grey: geomagnetic grid; Dotted black circle: latitude circle 70° Ngeographic; Grey dot-dash circle: latitude circle 70° geomagnetic.

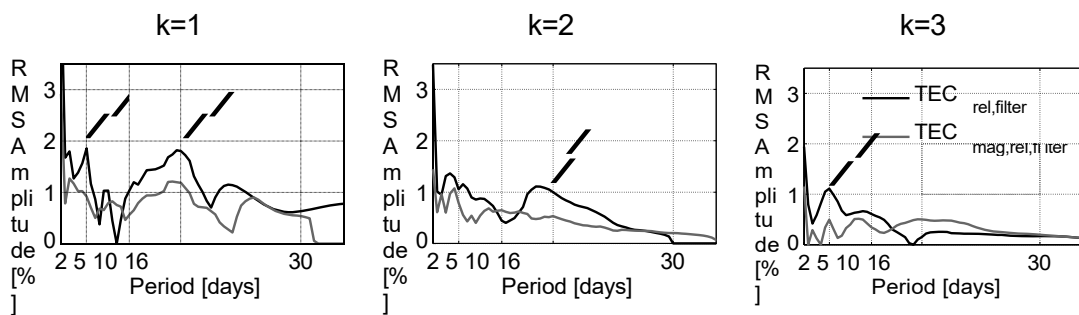


Figure 7.6: Comparison between PWTOs measured in geomagnetic (grey lines) and geographic (black lines) coordinate systems for standing waves in winter (Dec-Feb) 2002-2008. Left: Wave number 1; Middle: Right: wave number 3. The arrow marks PWTOs that clearly dominate the geographic grid.

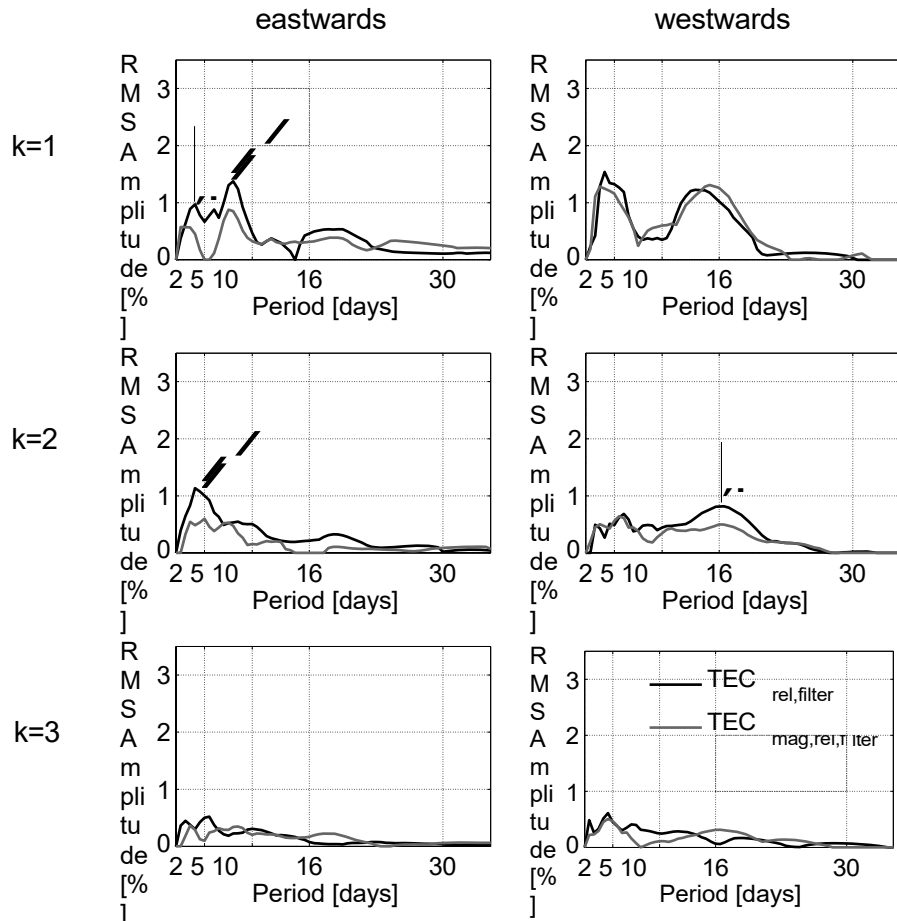


Figure 7.7: Comparison between PWTOs measured in geomagnetic (grey lines) and geographic (black lines) coordinate systems for travelling waves in winter (Dec-Feb) 2002-2008. Top: wave number 1; Middle: Wave number 2; Bottom: Left column: eastward moving PWTO; Right column: westward moving PWTO. The arrows mark PWTOs that clearly dominate the geographical grid.

The results, shown in Fig. 7.6 for standing waves and Fig. 7.7 for travelling waves, show very similar expressions of PWTO on the geographic grid and the geomagnetic grid. Often a slightly stronger expression of the PWTO is observed in the geographic grid. These PWTO are marked with arrows (Fig. 7.6 and 7.7). No clear result is obtained for the PWTO with wavenumber 1 moving westwards. Their expression is almost identical in the geographic and geomagnetic grid.

These results do not allow a clear conclusion. However, it appears that the PWTO observed in the ionospheric TEC maps preferentially circulate around the geographic pole, not the geomagnetic one. This suggests that the PWTO are indeed not tied to the geomagnetic field and do not arise from external or internal coupling. Instead, there are parallels with the PW of the lower and middle atmosphere, which are centred around the geographic pole by the action of the Coriolis force. The results shown here could therefore be an indication of coupling of the middle and upper atmosphere by atmospheric waves.

7.5 Summary and discussion

In this chapter, a spectral decomposition of the filtered $f_{j,TEC_{rel}}$ signal was carried out. Based on the analysis results, characteristic features of the PWTO in the years 2002-2008 could be determined. The comparison with the activity of stationary and migrating PW in the stratosphere shows that the typical occurrence (seasonal dependencies and wave parameters) of PWTO in the $f_{j,TEC_{rel}}$ filter corresponds well with that of stratospheric PW in the period under investigation. Both show a maximum activity in winter and a minimum activity in summer. The geographic location of the activity centres of the waves also shows good agreement between ionospheric PWTO and stratospheric PW for all wave numbers greater than 1 (the geographic location of the activity centre of the PWTO with wave number 1 could not be determined exactly). Furthermore, the natural frequencies known for the atmosphere were detected in the oscillations of the $f_{j,TEC_{rel}}$ filter, indicating that the observed PWTO are probably free oscillations. The most frequent periods described in this paper are also described in numerous observations of PWTO in the last decades (e.g. *Altadill et al.*, 2001, 2004; *Jacobi et al.*, 2007; *Lašto-vík* 2006, 1997). The aforementioned literature on the analyses of PWTO in the ionosphere at mid-latitudes is often limited to only a short period of time, to one location or individual PWTO or period ranges. Comparisons with the results of this work can therefore only be made individually. Agreements with

of PWTO activity in the filtered $f_{j,TEC_{rel}}$ described in the present paper, there are with *Gordienko et al.* (2005) and *Lašovic'ka* (2006), who observe the greatest day-to-day variability of the f_{oF} and the largest PWTO amplitudes in the winter months, respectively. The same is true for the observation of *Altadill et al.* (2004), who measure the most frequent occurrence of PWTO with larger periods (10-16 days) in winter. The dominance of zonal mean ($k = 0$) variations in frequency and amplitude is also confirmed by various works (e.g. *Altadill*, 2000; *Pancheva et al.*, 2009). *Lašovic'ka* (2006) finds no significant variation in the amplitude of the PWTO in the relative f_{oF} in the course of a solar cycle. Consistently, no dependence on the solar cycle can be found in the activity of the PWTO in the $f_{j,TEC_{rell}}$ filter (not shown here). For example, the dominant quasi-5-day waves observed in the $f_{j,TEC_{rell}}$ filter are almost uniformly strong during the entire study period (2002-2008) (not shown here).

In some cases, the literature describes properties of the PWTO that deviate from the results presented here. For example, *Altadill and Apostolov* (2003) describe maximum amplitudes of the 2- to 6.5-day waves in the f_{oF} at the equinoxes. However, because absolute and not relative amplitudes are used, this statement is not comparable with the PWTO amplitudes measured in the $f_{j,TEC_{rell}}$ filter.

The comparison of the PWTO observed in the DLR TEC maps to stratospheric PW in the mid-latitudes essentially reveals two differences. First, in the ionosphere the zonal mean variation dominates, while in the stratosphere the zonal mean variation is weaker than the PW with wavenumbers $k \geq 1$ (see Fig. A.2 and A.3). Secondly, oscillations with shorter periods ($T \leq 5$ days) are dominant in the ionosphere, whereas periods greater than 10 days are strongest in the stratosphere.

The observation of the dominance of zonal mean variations is confirmed by TIMED/-SABER analyses in the lower thermosphere (*Pancheva et al.*, 2009) and f_{oF} analyses (*Altadill*, 2000). *Pancheva et al.* (2009) hold the variations of the solar parameters responsible for the zonal mean variations. However, since this influence was significantly reduced in the $f_{j,TEC_{rell}}$ filter, this explanatory approach does not seem sufficient. *Horton et al.* (2008) describe a different explanatory approach, which assumes that AGW triggers the zonal mean variations in the MLT region on the basis of analytical investigations. The clarification of the actual cause of the zonal mean oscillations in the ionosphere remains an interesting research goal.

The observation of predominantly low periods in the ionosphere agrees well with the results of *Pogoreltsev et al.* (2007). Using analyses with a mechanistic model of the middle and upper atmosphere (MUAM), they describe that the rise of long-period PW is not possible. According to their statement, only short-period normal modes and ultra-fast Kelvin waves are able to ascend to the lower thermosphere. In *Hunt* (1984), too, the weakening of long-period PW and the strengthening of short-period PW above the stratosphere was

described. Maximum amplitude in the f_j ,TEC_{rell} filter has the PWTO with a two-day period for all wave numbers. A connection with the quasi 2-day wave, which is a known phenomenon in the mesosphere (Fröhlich, 2005; Jacobi and Kürschner, 2007), cannot be assumed because of the difference in seasonal occurrence. While the activity of the quasi 2-day wave in the mesosphere is maximum in summer due to the vertical wind gradients (Jacobi *et al.*, 1998), the PWTO with two-day period in the f_j ,TEC_{rell} filter are mainly observed in winter. Instead, it can be assumed that these 2-day oscillations are the reflection of drastic changes in the TEC, as they occur during geomagnetic storms. This would also explain their large amplitude, because deviations of the TEC from the mean behaviour of up to 200% have been measured for geomagnetic storms (Jakowski and Schlüter, 1999; Afraimovich *et al.*, 2001). The correlation analysis of the amplitude of the 2-day oscillation of the zonal mean and the geomagnetic index Ap shows that some extrema agree. However, the correlation coefficient of 0.3 (95% significant) is small. This means that quasi-2-day oscillations are often observed at times of geomagnetic disturbances, but not every time. An increase in the activity of the quasi 2-day wave during geomagnetic storms is nevertheless also observed in hmF (Pancheva *et al.*, 2002). The fact that the quasi 5-day wave is measured more strongly in the ionosphere than in the stratosphere and mesosphere can be confirmed by independent observations (Lawrence and Jarvis, 2003). However, unlike the maximum of the 5-day wave in the f_j ,TEC_{rell} filter in December and January, the maximum of the 5-day wave in f oF and SABER/TIMED temperatures is measured at the equinoxes (October and April) (Altadill *et al.*, 2001; Pancheva *et al.*, 2010). It should be noted, however, that the comparison is made with absolute amplitudes and that the measurements did not take place in exactly the same region. Because their seasonal occurrence neither coincides with stratospheric nor with mesospheric or ionospheric 5-day waves, the origin of PWTO with a 5-day period remains unclear (Borries and Hoffmann, 2010).

It should be noted that the absence of high periods in the observations of the f_j ,TEC_{rell} filter should not be overestimated, because the cost-intensive filter method used (see section 6.4) cancelled out all oscillations that occur simultaneously with oscillations of the solar signal. Since oscillations with periods between 25 and 30 days (the 27-day rotation period of the sun) occur almost continuously in the solar signal, signals in this period range are almost completely cancelled out. Oscillations with corresponding periods, which are caused by the influence of PW from the middle atmosphere, can therefore not or hardly be analysed.

The stationary PW so dominant in the stratosphere (see Fig. A.5) are no longer detectable in the f_j ,TEC_{rell} filter because of the filter method used. Other methods must be developed specifically for investigating stationary waves in the ionosphere. The emergence of quasi-stationary waves due to the deviation of the geomagnetic pole from the geographical pole must be taken into account.

The comparison to PWTO activity in the geomagnetic coordinate system has shown,

that PWTO activity is in most cases more pronounced in the geographic than in the geomagnetic reference system. This observation is an indication that PWTOs are concentrated around the geographic pole, similar to PWs in the middle atmosphere. However, since the differences in the measurements are only small and significance cannot be determined, this result should only be viewed with reservations.

The question remains open as to the origin of the PWTO observed in the f_j , TEC_{rell} filter signal. After some parallels to the PW of the middle atmosphere have been shown in this chapter, the question arises whether connections between individual stratospheric PW and ionospheric PWTO can be established. A possible connection to rising PW from the stratosphere will be investigated in the following chapter on the basis of differentiated considerations of various potential coupling mechanisms.

8. Potential connections to stratospheric planetary waves

8.1. Introduction

This chapter deals with the coupling mechanisms for the transfer of energy from PW to the ionosphere. A selection of coupling mechanisms proposed in the literature was presented in section 3.5. Not all of the mentioned mechanisms can be examined, firstly due to the lack of crucial data (especially at altitudes between 90 and 200km) and secondly to limit the scope of this paper. Therefore, only three selected studies are described in this chapter. In section 8.2, the simultaneous occurrence of PW in the stratosphere and PWTO in the ionosphere with the same wave parameters (wave number and phase velocity) is examined. This should provide information about the action of the 1st or 2nd coupling mechanism. The possibility of non-linear interaction of PW is analysed in section 8.3 (5th coupling mechanism) and the modulation of AGW (4th coupling mechanism) in section 8.4. A summary and discussion of the results is given in section 8.5.

8.2. Simultaneous activities in the stratosphere and ionosphere

The simplest approach to investigate a connection between PW activity in the stratosphere and ionospheric PWTO is to compare the simultaneous occurrence of waves with the same characteristics in both atmospheric layers. Here

it is assumed that the first or second of the coupling mechanisms presented in section 3.5 is active. Because it is not possible to determine whether the PWs affect the wind system or the thermospheric composition without examining supplementary data in the mesosphere, it is not possible to distinguish which of the two mechanisms is active. However, this will not be considered in this chapter.

The approach considered here neglects two details. Firstly, it does not take into account that an unknown delay can occur in the ascent of the PW. Secondly, it implies that the PW propagate directly into the ionosphere with constant period and wavenumber. As already described in section 3.5, this is not possible for all PW. However, because the observation of coexisting waves is not excluded (e.g. *Lawrence and Jarvis*, 2003; *Borries et al.*, 2007; *Pancheva et al.*, 2008b; *Mukhtarov et al.*, 2010), this method will be used to search for indications of a possible coupling.

The following investigations are based on the assumption that when the energy of stratospheric PWs is transferred to the ionosphere, the corresponding PWTOs in the ionosphere occur only with a small time delay (less than the period) to the original PWs in the stratosphere, if at all, and the frequency and wavelength remain almost constant. The FK wavelet spectra of $f_{TEC_{rel}}$ filter in 55° N and NCEP zonal wind data in 10hPa and 55° N are checked for simultaneous significant wave phenomena. For this purpose, the period range is divided into six classes as in section 7.2. Days with significant amplitudes in the same class in both the stratosphere and the ionosphere are marked with 1, all others with 0. Contiguous days marked with 1 are counted as one coexisting PWTO. The number of matches is meaningless without comparison to the number of matches with randomly occurring oscillations. For this purpose, a Monte Carlo test was performed with 1000 spectra of filtered¹ white noise. Mean and standard deviation of the number of matches were derived from the test. Because the results are approximately Gaussian distributed, the significance level is set at the mean plus twice the standard deviation, corresponding to the 95% significance level of normally distributed data. The significance level is shown in Fig.

8.1 marked with red bars.

The sum of the observed simultaneous PW in the stratosphere and PWTO in the ionosphere is broken down for the individual wave numbers and frequency bands in Figure 8.1. The figure contains partial coincidences of waves that occur earlier in the ionosphere than in the stratosphere. Because the vertical transport of PW energy shifts the phase of the wave forward in time (e.g. *Brown and John*, 1979), these cases were not eliminated from the listing. In addition, the start of oscillation can often not be determined exactly to the day (e.g. in the case of a non-constant

¹White noise was filtered using the same method as $f_{TEC_{rel}}$ filter.

frequency, slowly increasing amplitude or several oscillations with similar frequencies that cannot be precisely separated).

Based on the results in Figure 8.1, it is clear that, compared to the PWTOs that occur (see Fig. 7.1), about one third (a total of 128 out of 383) are observed simultaneously with stratospheric PWs. Matches are only observed for PWs with periods ≥ 5 days, which is related to the fact that hardly any significant PWs with periods smaller than 5 days occur in the stratosphere. Most matches are found for PW/PWTO with periods greater than 12 days and a wave number greater than 1.

PWTO with a significant number of matches to stratospheric PW are the eastward moving quasi-16-day wave with wave number 2, the quasi-20-day and quasi-30-day variations of the zonal mean, the standing quasi-16-day wave with wave number 2 and the standing quasi-30-day wave with wave number 3. No significant matches to stratospheric PW are found for the westward moving PWTO. Overall, for most PWTO in the $f_j, \text{TEC}_{\text{rell}}$ filter the number of observed matches to stratospheric PW in the zonal wind is below the determined significance level, which is why in these cases coincidental matches are to be assumed. Of the 96 wave classes investigated, significant matches are observed for only 6 wave types (6%). The number of PWTO coinciding with stratospheric PW in the IGS maps is somewhat lower than determined for the DLR maps. Here, only 2 significant matches are determined, whereby the significance level is only reached for one wave class coincident in the DLR and IGS data.

It can be assumed that with the significance test used, even a few wave classes can deliver significant results by chance. Because the proportion of significantly over-agreeing wave classes is only small, it is possible that none of the results is significant. However, it should be noted that the significant wave types occur in clusters. Based on this clustering, a correlation seems possible for the eastward waving quasi-16-day waves and standing waves with periods greater than 13 days. Investigations based on case studies could provide further results on this aspect. Because these studies go beyond the scope of this paper, they are proposed for follow-up work.

In summary, the significant agreements between stratospheric PW and ionospheric PWTO determined here show that a connection between the two phenomena is possible. However, this finding is not statistically reliable and exact statements about the coupling mechanisms (1st or 2nd coupling mechanism) cannot be made on the basis of these results.

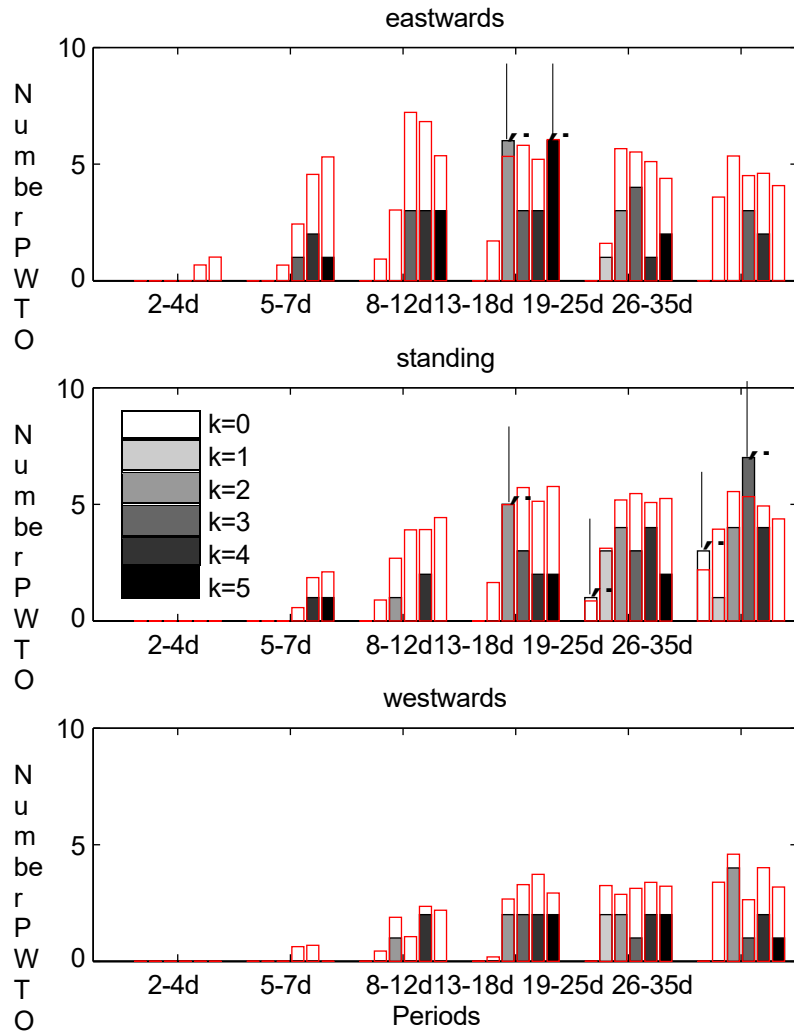


Figure 8.1: Number of simultaneously observed PW (NCEP zonal wind, 10hPa, 55° N) and PWTO (f_j , TEC_{rell} filter 55° N). The grey shading of the bars indicates the wave number. Red bars indicate the 95% significance level. The arrows mark the significant wave classes.

8.3. Results of non-linear interaction

In this section, the non-linear interaction of PW is investigated. This process triggers various secondary waves whose wave parameters depend on the primary waves (sum/difference of frequency and wavenumber).

The non-linear interaction between two waves works as follows: Given is a signal X consisting of 2 waves with the wave numbers k_1 and k_2 and the angular frequencies w_1 and w_2 .

$$X = \cos(k_1 A + w_1 t) + \cos(k_2 A + w_2 t) \quad (8.1)$$

A quadratic system acting on this signal causes the non-linear interaction of the two waves (primary waves), the result of which is the two primary waves and four secondary waves (see e.g. *Angelats i Coll and Forbes*, 2002).

$$\begin{aligned} X^2 = & 1 + \frac{1}{2} [\cos(k_1 A + w_1 t) + \cos(k_2 A + w_2 t)] \\ & + \cos((k_1 + k_2)A + (w_1 + w_2)t) \\ & + \cos((k_1 - k_2)A + (w_1 - w_2)t) \end{aligned} \quad (8.2)$$

As shown in Eq. 8.2, these four secondary waves have the wavenumbers/frequencies (k_1 / w_1), (k_2 / w_2), ($k_1 + k_2 / w_1 + w_2$) and ($k_1 - k_2 / w_1 - w_2$). The four types of secondary waves are numbered here as type I-IV. In the non-linear interaction between high-frequency and low-frequency waves, the frequencies of two secondary waves are close to the frequency of the high-frequency primary waves, resulting in the effect of amplitude modulation. In the atmosphere, for example, amplitude modulations of tides by PW can be observed.

Assuming that the wave ($k_1 w_1$) is a stratospheric PW whose parameters are known and the wave ($k_2 w_2$) is any atmospheric wave whose parameters are unknown, then the secondary wave of type I can be determined exactly, while types II to IV depend on the unknown second primary wave. If the second primary wave is tidal, the periods of the secondary waves with types II to IV will be less than a day (or just above) and thus not directly observable as PW- TO (possibly the effects of beat/modulation in the ionosphere are perceptible). If the second primary wave is also a PW, the type II secondary wave is included in the type I results. Types III and IV can only be identified with a very differentiated analysis. Because this effort is very high, the interaction between migrating PW and SPW is analysed as an example.

In the following, we will now examine whether the four secondary wave types resulting from the non-linear interaction between stratospheric migrating PW ($k_w w_w$) and stratospheric SPW ($k_s o$) can be observed in the ionosphere. According to Eq. 8.2

the following four secondary waves result from their non-linear interaction:

- Type I : (k_w ; w_w)
- Type II : (k_s ; o)
- Type III : ($k_w + k_s$; w_w)
- Type IV : ($k_w - k_s$; w_w)

For k_s the wavenumbers 1 to 3 are used. For the parameters k_w and w_w the frequencies and wavenumbers of the significant PW of the FK spectra calculated from NCEP reanalysis zonal wind data are used. The theoretical results of the interactions of the measured stratospheric PW are compared with observations in the f_j, TEC_{rell} filter.

The secondary wave type I arises regardless of which wave the primary PW interacts with non-linearly, be it an SPW, a tidal wave or another wave. In Fig. 8.2 the type I secondary wave matches of stratospheric PW with ionospheric PWTO are displayed. A total of 77 matches of PWTO with type I secondary waves are found. These are significantly fewer than were observed for the simultaneous PW/PWTO in section 8.2. However, the analysis method itself means that there are fewer matches. This is shown by the smaller significance levels (red bars in Fig. 8.2). The smaller number of matches is due to fewer spectra being compared (only half). For most wave classes (grey bars in Fig. 8.2), however, the number of matches is below the significance level. In five cases it exceeds it. These five cases are PWTO with wave number 0 and westward moving PWTO with wave numbers 2 and 6 with quasi-periods of 10 and 16 days.

Type II of the secondary waves considered here are stationary waves. Because stationary waves cannot be analysed in the f_j, TEC_{rell} filter (see section 7.2), this secondary wave type is not listed here.

For secondary wave type III, a total of 132 matches occur between theoretically generated secondary waves in the stratosphere and PWTO in the ionosphere. This number is very similar to the number of direct matches between stratospheric PW and ionospheric PWTO. Significant numbers occur for seven types of PWTO in this case. These are the eastward-migrating wave 5 with quasi-16-day and quasi-20-day periods, the zonal mean variations with quasi-16-day, quasi-20-day and quasi-30-day periods, the standing wave 4 with quasi-20-day period and the westward-migrating wave 2 with quasi-20-day period (Fig. 8.3).

A very similar result is observed for the type IV secondary waves (Fig. 8.4). Here, the sum of the measured coincidences is 116. Significant accumulations occur for six types of PWTO, the zonal mean oscillations with quasi-10-, 16-, 20- and 30-day periods, the westward moving wave 1 with quasi-16-day period and the westward moving wave 2 with quasi-10-day period.

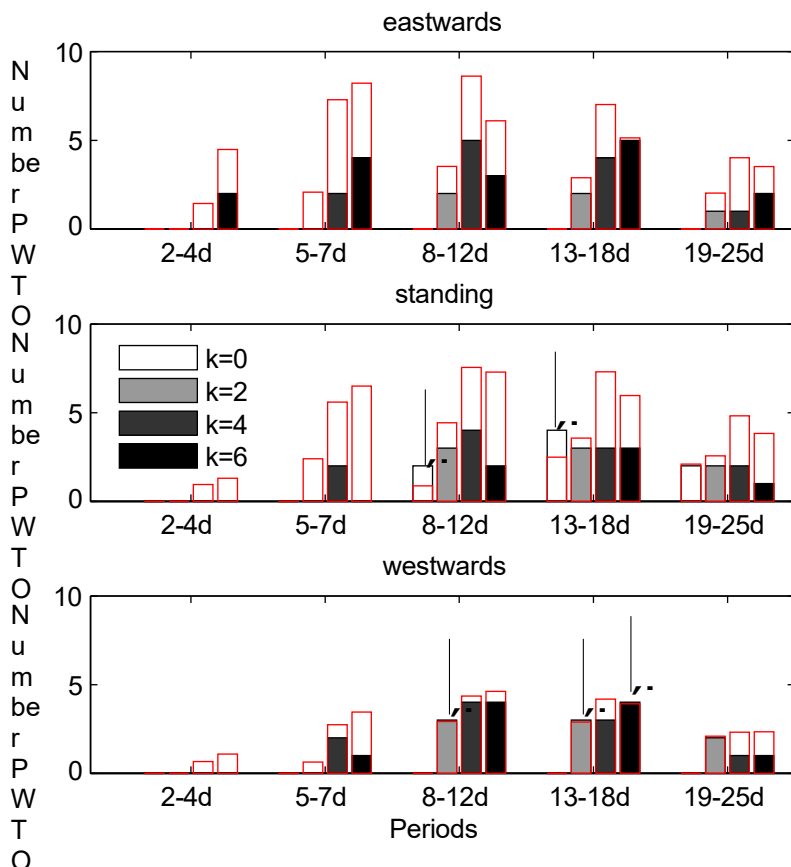


Figure 8.2.: Number of simultaneously observed PWTO in $f_{\text{J}}\text{TEC}_{\text{rell}}$ filter (55° N) and waves of secondary wave type I, which are theoretical result of non-linear interaction of PW and SPW (NCEP zonal wind, 10hPa, 55° N). The 95% significance level is marked with red bars. The arrows mark the significant wave classes.

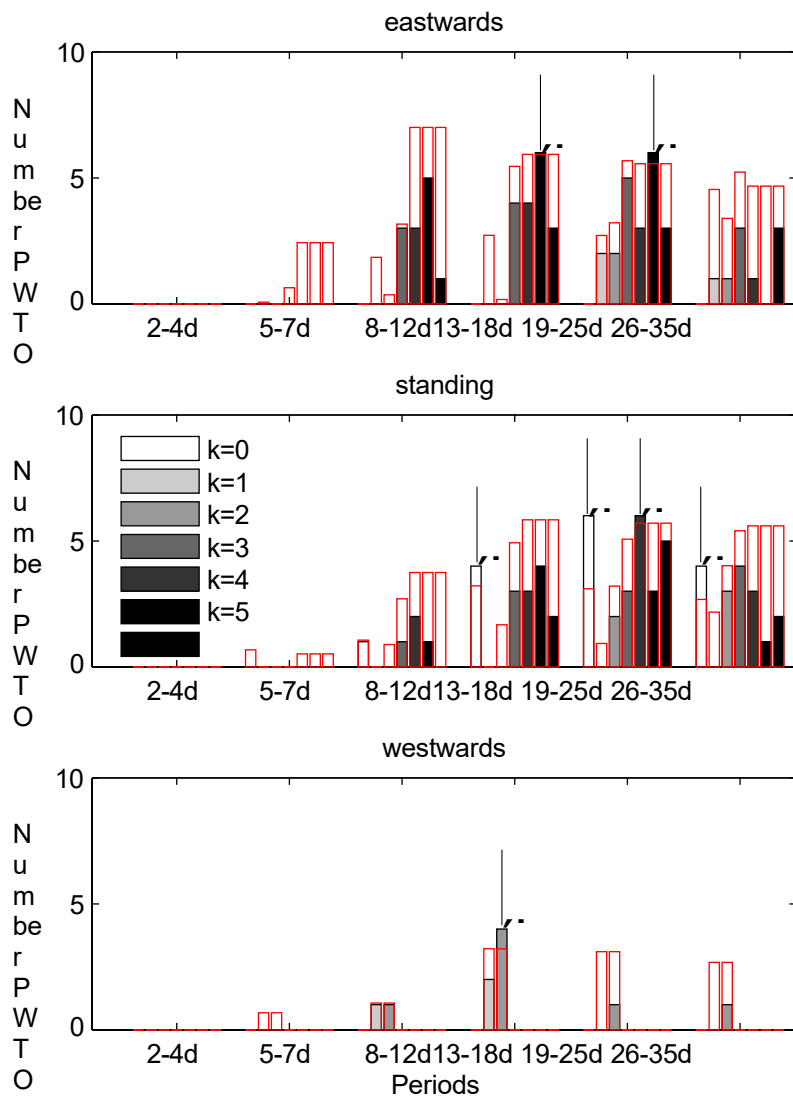


Figure 8.3.: Number of simultaneously observed PWTO in f_J , TEC_{rell} filter ($55^{\circ} N$) and waves of secondary wave type III, which are theoretical result of non-linear interaction of PW and SPW (NCEP zonal wind, 10hPa, $55^{\circ} N$). The 95% significance level is marked with red bars. The arrows mark the significant wave classes.

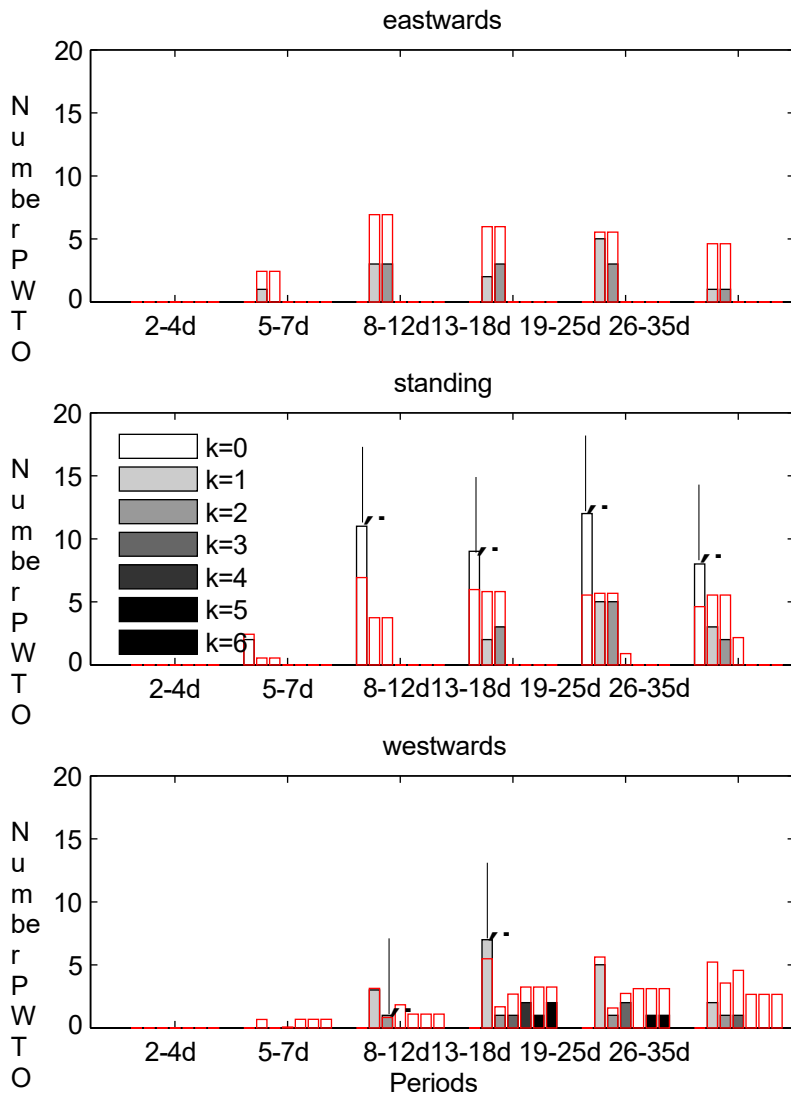


Figure 8.4.: Number of simultaneously observed PWTO in $f_{j,\text{TEC}_{\text{rel}}}$ filter (55° N) and waves of secondary wave type IV, which are theoretical result of non-linear interaction of PW and SPW (NCEP zonal wind, 10hPa, 55° N). The 95% significance level is marked with red bars. The arrows mark the significant wave classes.

The IGS data show a lower number of matches between ionospheric PWTO and potential stratospheric secondary waves (see Figs. B.8- B.9) than the DLR data. Instead of the total of 18 wave classes with significant matches in the DLR data, a total of 11 wave classes with significant matches are determined in the IGS data. These are almost exclusively limited to the zonal mean oscillations.

The investigation of the potential nonlinear interaction of PW has shown that some PWTO in the $f_j, \text{TEC}_{\text{rell}}$ filter can be associated with stratospheric PW if a nonlinear interaction between migrating PW and SPW is assumed. This conjecture assumes that the secondary waves can rise higher than the primary waves due to altered wave parameters (wavelength and phase velocity). In the case of a primary influence of the nonlinear interaction on the coupling mechanisms between the lower and middle atmosphere and the ionosphere, significantly more matches between PWTO and potential secondary waves (especially of type I, which is independent of the second primary wave) would be expected than direct matches between PWTO and stratospheric PW. However, similar numbers of matches between PWTO and potential secondary waves are observed as matches between PWTO and PW were measured. For only 18 out of 270 (6.7%) of the examined classes of PWTO the number of matches reaches the 95% significance level. Thus, with the statistical method used, no decisive indication for a primary influence of the PWTO can be found.

5. coupling mechanism (see section 3.5) can be established. Instead, case studies are suggested for the following investigations. Although only a few significant matches were measured, these nevertheless suggest a connection with vertically propagating secondary waves. Significant agreements, some of which go far beyond the significance level, are frequently measured for the variations of the zonal mean. Due to the clustering of the occurrence, it can be assumed that these PWTO are connected with stratospheric PW.

When evaluating the results, some weaknesses of the method used should be noted. As in the previous section, these analyses do not differentiate whether the PWTO or the PW with significant amplitude occurs first. Furthermore, the classification can lead to a wave being recorded in neighbouring classes at the same time.

8.4. Modulating atmospheric gravity waves

The theoretical possibilities of transferring the energy of the PW into the ionosphere also include the modulation of the AGW, through which secondary PW can be generated in the E-region (coupling mechanism 4). The modulation of the AGW with PW properties is a linear effect. The transfer of PW signatures to AGW occurs through the influence of the vertically propagating AGW by the PW-influenced wind systems in the stratosphere. This can cause variations in the frequency and amplitude of AGW. This transfer process of PW into the ionosphere was proposed by Meyer (1999) and tested by modelling. Meyer (1999) was able to demonstrate a transfer of PW energy into the lower thermosphere. However, to the best of our knowledge, no empirical analyses have yet been carried out to investigate the relevance of the 4th coupling mechanism for the atmosphere-ionosphere coupling.

If AGW penetrates into the thermosphere, it is assumed that their signatures can also be seen in the ionosphere. This assumption is based on the observation of coincident signatures of AGW in the ionospheric TEC and AGW in the MLT region (Saito *et al.*, 2002, 2007; Tsugawa *et al.*, 2007). The signatures of AGW in the ionosphere are called Travelling Ionospheric Disturbances (TID). A significant influence of AGW on the ionosphere was determined theoretically and empirically by Vadas and Liu (2009). They describe that secondary AGW (i.e. secondary waves generated by non-linear interaction in the lower thermosphere) can even rise into the F2 layer.

In this chapter, the following action chain will be investigated and tested: PW-Modulation of AGW-Modulation of TID- PWTO. First, PW are observed in the stratosphere. At the same time, a modulation of AGW amplitudes is observed, which continues into the lower thermosphere. A modulation of TIDs then occurs in the TEC and PWTO are observed at the same time. If no break in the chain occurs, modulation of AGW is a likely transmission mechanism. However, if an interruption of the action chain occurs, the 4th coupling mechanism is considered unlikely. In the following, the observation of the TID activity and then the AGW activity is explained before the investigation of the action chain begins.

Ionospheric TIDs can be determined very accurately from the differential carrier phases of the GNSS signals. A proven method for determining the TID amplitudes is to link-referenced² the TEC differences to a moving hourly TEC mean (also called

²"Link" in this case means uninterrupted measurement between a satellite and a ground station.

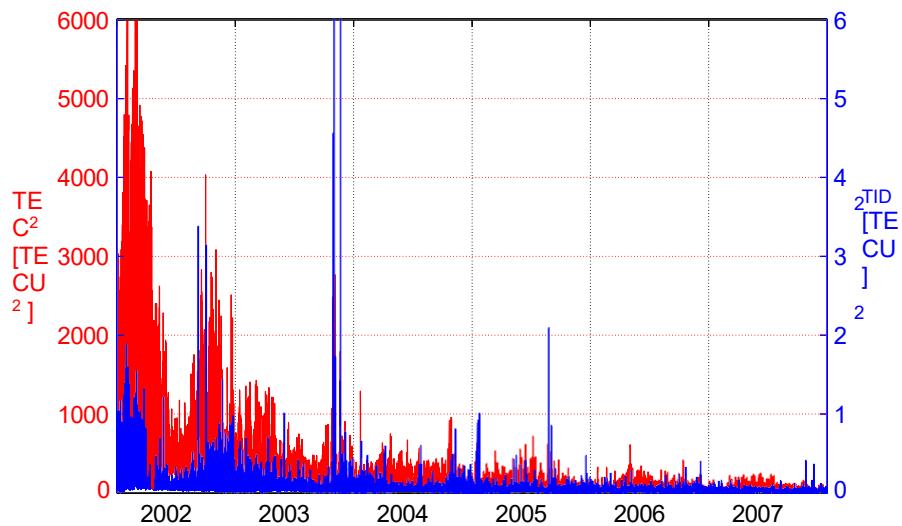


Figure 8.5: Comparison of the variance of the TID amplitudes (blue) with the quadratic TEC (red, taken from the Europe TEC maps of the DLR) in the subregion (10° W- 30° E, 50 - 55° N). The blue axis labels the variance, the red axis the quadratic TEC. The vertical grid lines mark the change of year (1 January).

link-related) (the measurement method is described in detail in *Borries et al. (2009)*). In this way, about 1000-2000 TID amplitudes can be measured over Europe every 30 seconds. To investigate the variation of TID activity, the variance of the measured TID amplitudes for the European region (-10 - 30° E, 35 - 65° N) is determined for each hour. Preliminary studies have shown that the TID activity in this region is largely homogeneous zonally, while there are strong differences meridionally. Therefore, the study region is divided meridionally into 6 sub-regions, each with a meridional extent of 5° . The variance of the measured TID amplitudes for the subregion 10° W- 30° E, 50 - 55° N and the period 2002 to 2007 is shown in Fig. 8.5 (blue).

During the study period (2002-2007) a clear decreasing trend of the variance of the TID amplitudes can be observed. Local variance maxima occur at the equinoxes. The comparison in Fig. 8.5 shows that the variance of the TID amplitudes is approximately proportional to the squared TEC. As a measure of the TID activity therefore the quotient of the amplitude variance (u^2_{TID}) and the square of the median

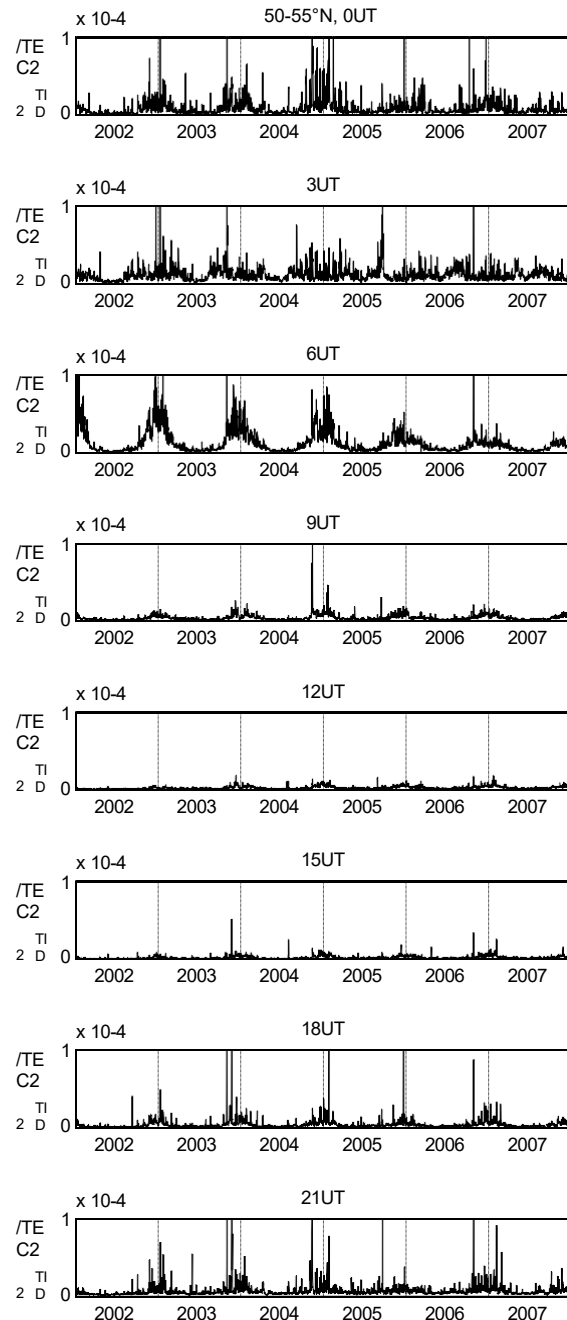


Figure 8.6.: Variance of TID amplitudes relative to TEC in the region 10° W- 30° E, $50\text{-}55^{\circ}$ N. Each graph represents a different universal time (UT): 0UT at the top, 21UT at the bottom. The vertical grid lines mark the change of year (1 January).

of the zonally averaged TEC was chosen.

$$P_{TO}(cp\ t) = \frac{u_{TO}^2(cp\ t)}{\text{median}_{27}(m_A(T\ EC(A\ cp\ t)))^2} \quad (8.3)$$

The function m_A calculates the zonal mean. However, the study area of the TIDs only covers the longitude range 10° W to 30° E. The median is calculated in a 27-day running window. The TID activity P_{TO} is calculated for each subregion with the mean latitude cp with a temporal resolution of 1 hour. Excerpts from the measurements of the TID activity for the study period 2002 to 2007 for different universal times (UT, where universal time and local time are close to each other in this region) are shown in Fig. 8.6. A clearly increased TID activity during the winter months can be seen, which was also noted by *Tsybulya* (2005). The comparison of the different times of day shows a clearly lower TID activity during the day and a very large variability at night, whereby very large amplitudes can occur at night. In the morning hours (6UT), TID activity is generally high, with a clear seasonal cycle. The relatively small variance below the seasonal cycle at this UT suggests a climatological effect. This is the solar terminator, with its relatively large gradients reflected in the TID activity in this way. The annual cycle here arises from the local change in sunrise time during a year.

Because of the relatively small degree of interference, the TID activity around 12UT was chosen as the object of the investigation of the modulation with periods of PW. The TID activity is analysed spectrally with the continuous wavelet transform. Significant oscillations in the wavelet amplitude spectrum of TID activity (subregion 10° W- 30° E, 50 - 55° N) are marked in black in Figure 8.7. During the winter months, significant oscillations are clearly visible in the period range of PW. Similarities to PW activity in the middle atmosphere can thus be demonstrated in the modulation of ionospheric TID amplitudes.

Significant oscillations of the zonal mean of $f_j, TEC_{rel\ filter}$ (10° W- 30° E, 50° N) will be enclosed by blue lines in Fig. 8.7. The comparison between the PWTO modulations of the TID activity and the PWTO in the $f_j, TEC_{rel\ filter}$ shows some correspondences in winter months. A connection between the modulations of the TID and the ionospheric PWTO thus seems possible.

AGW analyses are based on SABER/TIMED³ temperature data. The orbital satellite measurements (individual temperature profiles from 30-130km) are analysed separately for diurnal and nocturnal overflights. By high-pass filtering the signals with vertical wavelengths $A_{i2} < 6$ km, the amplitude T^i of the AGW-

³SABER (Sounding of the Atmosphere using Broadband Emission Radiometry) is one of the instruments of NASA's TIMED (Thermosphere Ionosphere Mesosphere Energetics and Dynamics) mission, for global exploration of the mesosphere and lower thermosphere.

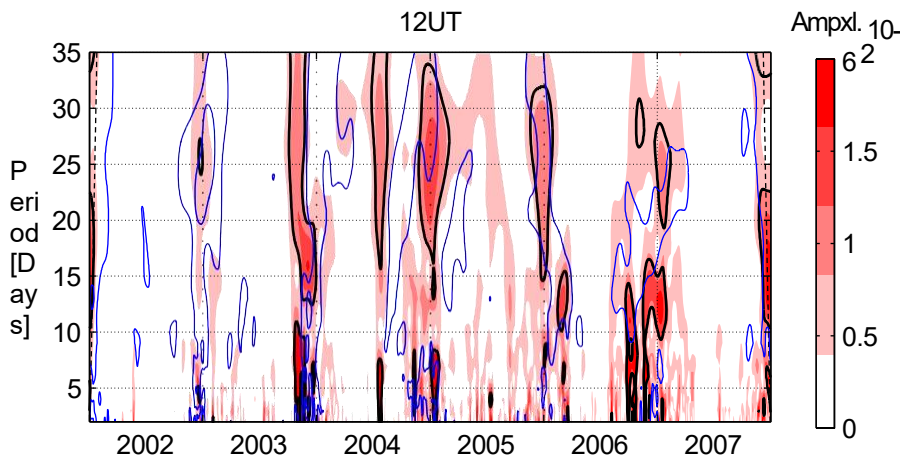


Figure 8.7: Wavelet spectrum of TID activity (12UT) in the region -10° E to 30° E, 50° N to 55° N. The red shading indicates the amplitude of the oscillation, the black lines outline the 95% significant amplitudes. Blue lines outline areas with 95% significant oscillations of the f_J , TEC_{rell} filter (zonal mean -10 - 30° E, 50° N). The vertical grid lines indicate the change of year (1 January).

proportion is determined. Measurements on approx. 15 orbits per day are interpolated into a regular 3-dimensional grid (length, width, height), whereby a continuous width reduction from 50° S to 50° N is achieved. For the comparison to the ionospheric TID activity, the AGW amplitudes for 50° N are used.

Because the evaluation of the SABER data is complex and the modulation of the AGW by PW cannot be determined directly by spectral analyses, special proxies for the description of the amplitude modulation by PW were developed in cooperation with P. Hoffmann (University of Leipzig). These PW proxies are described by the following equations:

$$\begin{aligned}
 P_{\text{a}}^{1/\text{ion}}(t \text{ cp}) &= u_t(\mathbf{m}_A(\cdot)) \\
 &= \frac{\sum_{A=1}^{T-1} \mathbf{1}_{x \in A \text{ cp}} - 1}{T-1} \quad (8.4) \\
 P_{\text{a}}^{1/\text{prop}}(t \text{ cp}) &= m_A(u_t(\mathbf{m}_A^{t-T}(\cdot))) \\
 &= \frac{\frac{1}{T-1} \sum_{A=1}^{T-1} b(x \in A \Phi) - 1}{T-1} \quad (8.5)
 \end{aligned}$$

$$\begin{aligned}
 \text{with } b(x A cp) &= (x A cp) \quad \frac{1}{I \setminus} \wedge (x A^T cp) \\
 P_{a}^{1/\text{stat}}(t cp) &= u_A(m_t(\cdot)) \\
 &= \sqrt{\frac{1}{T} \int_{x=t-T}^{t+T} (x A cp)^T \frac{1}{I \setminus} \wedge (y A^T cp)} \quad (8.6)
 \end{aligned}$$

The functions u_t and m_t calculate the temporal standard deviation and the temporal mean in a sliding window with width $T = 30$ days, and the functions u_A and m_A calculate the zonal standard deviation and the zonal mean accordingly. Here $I \setminus$ is the available length range. Meaningful PW proxies are only obtained if the length range $0\text{--}360^\circ$ is available. Zonal mean variatio-

nes are described by the PW proxy $P_{a}^{1/i2on}$, stationary PW by the proxy $P_{a}^{1/\text{stat}}$, and the proxy $P_{a}^{1/\text{prop}}$ contains the roaming PW. These PW proxies can

can be calculated from any data sets that have a zonal and temporal dimension. They thus allow a general description of PW activity without a spectral decomposition (Borries and Hoffmann, 2010). The normalisation of the data with their standard deviation enables the comparison of their PW proxies.

For the analysis of the action chain, the given PW proxies are calculated from the stratospheric reanalyses, SABER AGW data, TID data and TEC data. There is a limitation in the calculation of the PW proxies for the TIDs because the zonal variation of the TIDs cannot be resolved due to the small zonal extent of the study region ($10^\circ\text{W}\text{--}30^\circ\text{E}$). The PW proxies, which are calculated from the TID activity, can therefore only be understood as a very rough approximation and must be considered in a differentiated manner. Ultimately, the use of the PW proxies enables the comparison sought between the stratospheric PW activity, the AGW modulation in the MLT region, the TID modulation in the ionosphere and the ionospheric PWTO.

Figure 8.8 shows the corresponding PW proxies $P_{a}^{1/i2on}$ for the zonal mean variations at latitude $cp = 50^\circ\text{N}$. In the stratosphere, where the zonal mean variations are weak, the PW proxy $P_{a}^{1/i2on}$ of the zonal wind in 10hPa is accordingly small, with amplitudes somewhat larger in winter than in summer. The $P_{a}^{1/i2on}$ of the AGW amplitudes show a similar picture in the stratosphere. Here, too, $P_{a}^{1/i2on}$ is generally small with maximum amplitudes in winter. In the upper mesosphere (80km altitude) the seasonal variation changes to maximum amplitudes in summer. Above this, at an altitude of 100 to 120km, there is no clear seasonal trend in the $P_{a}^{1/i2on}$ of AGW amplitudes.

can be seen. In contrast to the relatively small $P_{a}^{1/i2on}$ in the stratosphere and the MLT region, the PW proxy of $f_j, \text{TEC}_{\text{rel filter}}$ shows very strong zonal mean variations in the ionosphere (in good agreement with the results in chapter 7). Also the high

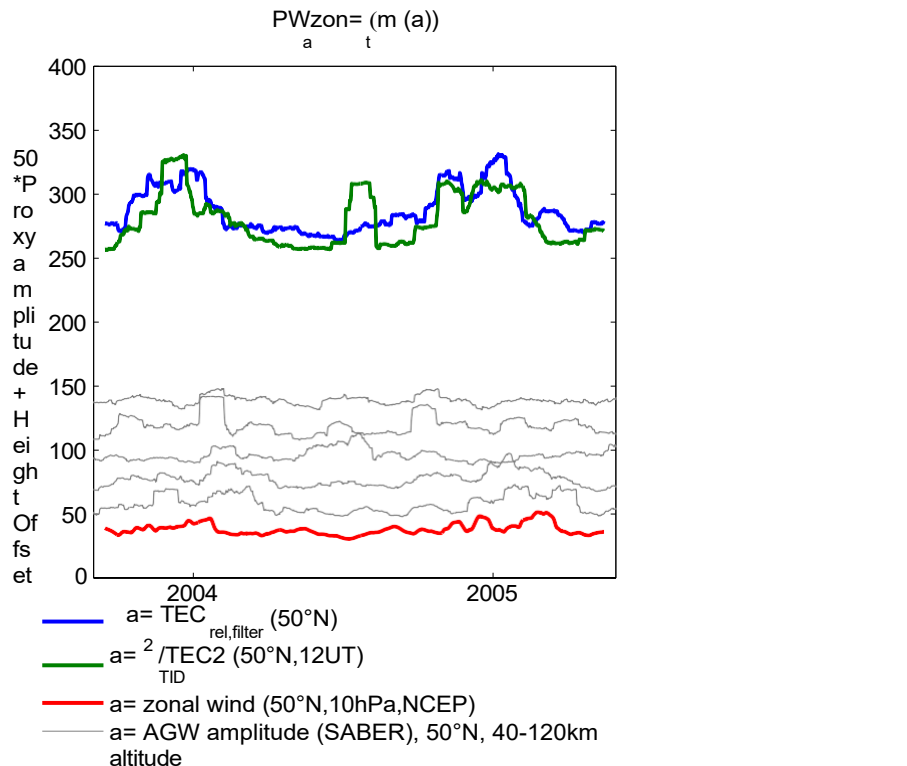


Figure 8.8.: PW proxy
Mean Variations

of the
P 1 / i²on

Zonal
 a_t

calculates for

fj, TEC_{rel filter} (blue), the TID activity (green), the AGW amplitudes (grey) and the zonal wind u in 10hPa (red) in 50° N for the period from 01 September 2003 to 31 May 2005. Before calculating the proxies, the data were normalised with their standard deviation. The PW proxies were multiplied by 50 and the approximate height of the observation was added (stratospheric zonal wind (10hPa): 30km; AGW: 40, 60, 80, 100, 120km; TID: 250km; fj, TEC_{rel filter}: 250km). The vertical grid lines indicate the change of year (1 January).

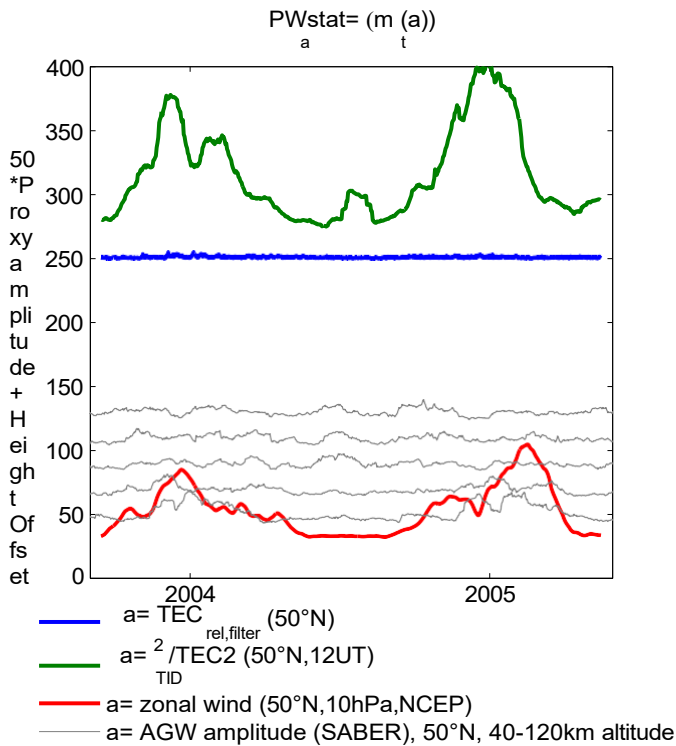


Figure 8.9.: PW proxy of the stationary waves $P_{1/a}^{\text{stat}}$ calculated for $f_j, \text{TEC}_{\text{cell}}$ filter (blue), the TID activity (green), the AGW amplitudes (grey) and the zonal wind in 10hPa (red) in 50° N. The further image description corresponds to Fig. 8.8.

Winter activity of the PWTO is reflected in the PW proxy of the f_j ,TEC_{rell} filter. The PW proxy $P_{\alpha}^{1/2on}$ of TID activity shows very good agreements with the f_j ,TEC_{rell} filter proxy. The strong amplitude swing in July 2004 is due to large TID activity caused by a strong geomagnetic storm on 26 July (Borries et al., 2009).

The PW proxies $P_{a1}^{1/\text{stat}}$, which describe the expression of the stationary waves, are shown for the stratospheric zonal wind, amplitudes of AGW in the MLT region, the ionospheric TID activity and $f_j, \text{TEC}_{\text{rell}}$ filter in Fig. 8.9. The dominance of stationary waves in the stratosphere is clearly reflected in the PW proxy of the stratospheric zonal wind, where very large amplitudes of $P_{1/\text{stat}}$ are observed in winter. A slight modulation of AGW amplitudes is observed in the stratosphere and lower mesosphere (40 and 60 km altitude). However, it does not continue upwards. The $P_{1/\text{stat}}$ of $f_j, \text{TEC}_{\text{rell}}$ filter shows no amplitudes (except for a small noise) because the data processing excludes the analysis of stationary waves. In contrast, the PW proxy of TID activity shows very large amplitudes in winter. However

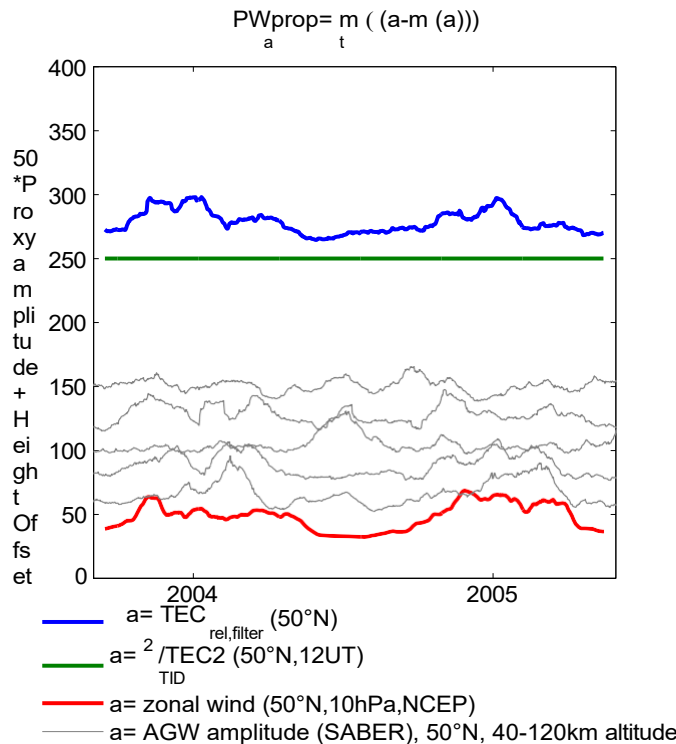


Figure 8.10.: PW proxy of travelling and standing waves $P_{1/a}^{prop}$ calculates for f_j , $TEC_{rel,filter}$ (blue), the TID activity (green), the AGW amplitudes (grey) and the zonal wind in 10hPa (red) in $50^\circ N$. The rest of the image description corresponds to Fig. 8.8.

this proxy is not meaningful because of the insufficient zonal coverage of the TID data. The PW proxy $P_{1/a}^{prop}$, shown in Fig. 8.10, describes the proportion of travelling and standing waves. However, it also contains the noise component of the signal. The $P_{1/a}^{prop}$ of the stratospheric zonal wind in 10hPa (NCEP) is less than the corresponding $P_{1/stat}$ and greater than $P_{1/i2on}$. It shows that the PW activity of the migratory and standing waves in the stratosphere begins in October and ends in late spring. The $P_{1/a}^{prop}$ of the AGW amplitudes is greater than the corresponding $P_{1/stat}$ and $P_{1/i2on}$. In the stratosphere and lower mesosphere, like the $P_{1/a}^{prop}$ of the Zonal-wind (10hPa) shows a seasonal variation with the amplitude maximum in winter. In the upper mesosphere (80km altitude) the seasonal cycle is reversed and the amplitude maximum is observed in summer. It is known that in this region AGW activity is highest in summer with a shift to the equinoxes at higher altitudes (Jacobi et al., 2006). These activity maxima are reflected in the PW proxies.

In addition, the maximum of $P_{1/\text{prop}}^a$ at an altitude of about 80km can be caused by the quasi-2-day wave, whose activity is greatest in summer at this altitude (*Forbes and Zhang, 1997; Fröhlich, 2005*). No well-defined seasonal variation can be identified in the lower thermosphere. Nevertheless, there seems to be a tendency towards higher amplitudes in winter. In the ionosphere ($f_j, \text{TEC}_{\text{rel filter}}$) a clear seasonal cycle can be observed. With the amplitude maximum in winter, beginning in October and ending in April/May, the seasonal cycle resembles that of the travelling and standing waves in the stratospheric zonal wind. For TID activity, the proxy $P_{1/\text{prop}}$ cannot be calculated due to the lack of zonal coverage of the data.^a

For the interpretation of the results, some limitations, some of which have already been mentioned, have to be taken into account. The biggest weakness of this analysis is the low zonal coverage of the TID data, which makes the PW proxies of TID activity unreliable. Another weakness to consider is that the $P_{1/\text{prop}}$ includes not only the travelling and standing waves, but also the noise in the data. Thus, if the signal-to-noise ratio is small, the amplitude of the $P_{1/\text{prop}}$ can be affected by the noise. Furthermore, it should be noted that TIMED-SABER is sun-synchronous, which creates a kind of wave whose effect on this analysis should be considered.

In summary, the action chain PW modulation of the AGW modulation of the TID PWTO is not detectable for any of the three PW wave types (zonal mean variations, static waves and travelling and standing waves). Apart from the limitations in the calculation of the PW proxies of the TID amplitudes, the action chain is always interrupted in the upper mesosphere (approx. 80km altitude). A transfer of the PW amplitudes to the dynamo-induced E-field thus seems unlikely. Nevertheless, similar amplitudes of the PW proxies can be observed in the stratosphere and the ionosphere for zonal wind variations and travelling and standing waves. However, clear correspondences between local maxima of stratospheric and ionospheric proxies cannot be found in Figures 8.8 to 8.10. Although the chain of action cannot be observed continuously, it seems premature to 4. coupling mechanism as not possible. Clearer results are expected if targeted PW proxy maxima at times when coincident stratospheric PW and ionospheric PWTO are known from the FC analyses are discussed. Corresponding analyses are proposed for follow-up work.

8.5 Summary and discussion

In this chapter, possible connections between stratospheric PW and ionospheric PWTO were investigated and possible coupling mechanisms were considered. It should be emphasised here that not all coupling mechanisms were included. It

was focused on a selection of processes that seemed likely and for which suitable analytical methods and data were available.

First, evidence for direct propagation of PWs into the lower thermosphere (coupling processes 1 and 2) was sought by analysing direct matches in the wave parameters of significant stratospheric PWs and ionospheric PWTOs. Second, the possible influence of secondary PWs, which arise from a non-linear interaction of PWs, on the lower thermosphere was analysed (5th coupling mechanism) by testing correspondences between potential secondary waves and ionospheric PWTO. Third, coupling through modulated AGW (4th coupling mechanism) was investigated by analysing the action chain PW modulation of AGW modulation of TID PWTO. Some evidence of coupling between the ionospheric wave-like phenomena with atmospheric waves was uncovered. Differences were also discovered that need to be discussed.

The differences in the climatology of PWs in the stratosphere and the properties of ionospheric PWTOs shown in Chapter 7 already indicate that not many direct matches between stratospheric PWs and PWTOs are to be expected. Accordingly, the number of direct matches between stratospheric PW and ionospheric PWTO is largely in the random range. For a few wave types, the number of matches exceeds the random level. Especially for long-period PW (quasi-16-day wave and quasi-30-day wave) with wave numbers greater than one, significant matches are found. An example for the direct propagation of the quasi-16-day wave with wavenumber 1 into the lower thermosphere (120km altitude) could recently be proven with observations of SABER/TIMED temperatures (*Mukhtarov et al.*, 2010). Moreover, a quasi-16-day wave was observed simultaneously with the 16-day temperature wave in the lower thermosphere in both f_{oF} and $f_{j,T} EC_{rel}$. Because the quasi-16-day wave in the E region probably does not have a sufficiently large amplitude to affect the wind dynamo of the E region (*Forbes et al.*, 1995; *Forbes*, 1996), it can be assumed that the variation in thermospheric composition associated with the PW affects the ionosphere (1st coupling mechanism). It seems reasonable to assume that the significant correspondences between stratospheric PW and ionospheric PWTO found here are also related to each other via the 1st coupling mechanism. However, because the number of significant matches is not large, a primary coupling mechanism cannot be assumed. Furthermore, it should be noted that the analyses of the IGS maps only show significant correspondences for 2 wave classes (see Fig. B.7).

In contrast to the few significant matches of primary waves, the number of matches between potential secondary waves of stratospheric PW and ionospheric PWTO is significant for some wave types. A particular indication of the contribution of the nonlinear interaction to the atmosphere-ionosphere-

coupling are particularly many coincidences for the PWTO of the zonal mean, which were described in section 8.3. The particularly strong zonal mean oscillations in the fj, TEC_{rell} filter are neither directly related to the solar influence nor to zonal mean oscillations in the lower and middle atmosphere (see Chapters 6 and 7). However, based on the results in section 8.3, it seems likely that the zonal mean oscillations arise as secondary waves due to the non-linear interaction between PW. However, various other PWTO with wave numbers between 0 and 6 and periods longer than 8 days also find significant correspondences with potential secondary PW. The analyses of the IGS maps show a very similar result (see Figs. B.8- B.10). The non-linear interaction between PWs could thus be an essential part of the transfer of PW energy into the ionosphere (5th coupling mechanism).

The modulation of AGW amplitudes as a possible component of the coupling of the atmosphere-ionosphere system (4th coupling mechanism) was investigated in section 8.4. The investigation using proxies of PW modulation at different altitude levels between 30 and about 250km altitude showed similarities between stratospheric PW and ionospheric PWTO. Moreover, in the stratosphere and lower mesosphere, AGW amplitudes appear to be modulated by PW. However, this modulation disappears in the mesopause region. In this region, near the zero wind line or region with low zonal winds, is the "wave turbopause" (Offermann *et al.*, 2007). Due to the low wind speeds, rising waves break more strongly in this region. The breaking waves in turn generate turbulence, release energy and momentum to the surrounding area and feed back to the zonal wind. According to the results in section 8.4, the AGW seem to break more in the "wave turbopause", releasing the energy of their modulation in this region. No continuous PW activity could be detected in the action chain PW modulation of the AGW modulation of the TID PWTO, so the 4th coupling mechanism seems unlikely. Because the completed analyses cover a relatively large period of almost 2 years, no individual phenomena were considered. Further analyses of the PW proxies at times when coincidences of stratospheric PWs and ionospheric PWTOs occur are necessary in order to identify the

4. to prove or disprove the coupling mechanism (modulation of AGW).

The 3rd coupling mechanism (modulation of the tides) was not analysed in more detail in this work for the reasons given. However, there are numerous references to its effect in the literature. Long ago, model studies showed that tides in the thermosphere (above 120km altitude) during sunspot minimum conditions are driven by forces from below (Hong and Lindzen, 1976) and recent observations (Immell *et al.*, 2009; Forbes *et al.*, 2009) confirm these studies. Consequently, it is reasonable to assume that during a sunspot minimum, tidal signals can be transmitted from the middle atmosphere to the ionosphere/thermosphere. Recent model studies with the NCAR TIME-GCM (Thermosphere- Ionosphere-Mesosphere-Electrodynamics General Circulation Model of the National Center

for Atmospheric Research) confirm this hypothesis (*Liu et al.*, 2010a). *Liu et al.* (2010a) describe the influence of quasi-SPW on the ionosphere (dynamo, ion drift, F2 layer height, maximum electron density and TEC) in the sunspot minimum through the nonlinear interaction with tides. Evidence for this coupling mechanism is also found in various observations. *Huang et al.* (2009), for example, describe the modulation of the daily tide in the lower and middle atmosphere (mid-latitudes). Some observations of PW and tides in the MLT region show the occurrence of various secondary waves that arise from nonlinear interaction or amplitude modulation (*Manson and Meek*, 1990; *Teitelbaum and Vial*, 1991; *Beard et al.*, 1999). *Pancheva et al.* (2008b) also describe the contribution of modulated tides to the generation of PWTO in the MLT region in the tropics. Moreover, spatial structures known from PW have been found in mid-latitudes in the parameters of the sporadic E layer, which is closely related to the semidiurnal tide (*Haldoupis and Pancheva*, 2002; *Zykov et al.*, 2009). Complementarily, comparisons between mesopause winds (meteor radar data from Collm, 13° E, 51.3° N) and $f_j, \text{TEC}_{\text{rell}}$ filter can reveal coincidences in the modulation of the mesosphere-dominant semidiurnal tide and PWTO in the $f_j, \text{TEC}_{\text{rell}}$ filter. Figure 8.11 shows an example of such a coincidence. In January 2006, the semi-diurnal tide is simultaneously modulated with a quasi-10-day wave and a PWTO with a period of 10 days is observed in the zonal mean of the $f_j, \text{TEC}_{\text{rell}}$ filter. In February 2006, a quasi-16-day wave occurs simultaneously in the modulation of the half-day tide and in the $f_j, \text{TEC}_{\text{rell}}$ filter.

Empirical studies, such as those carried out in this chapter, provide information on possible coupling mechanisms between the lower and middle atmosphere and the ionosphere. In combination with modelling analyses, such as those carried out in *Liu et al.* (2010a) and *Pogoreltsev et al.* (2007), the physical mechanisms of the coupling can be proven.

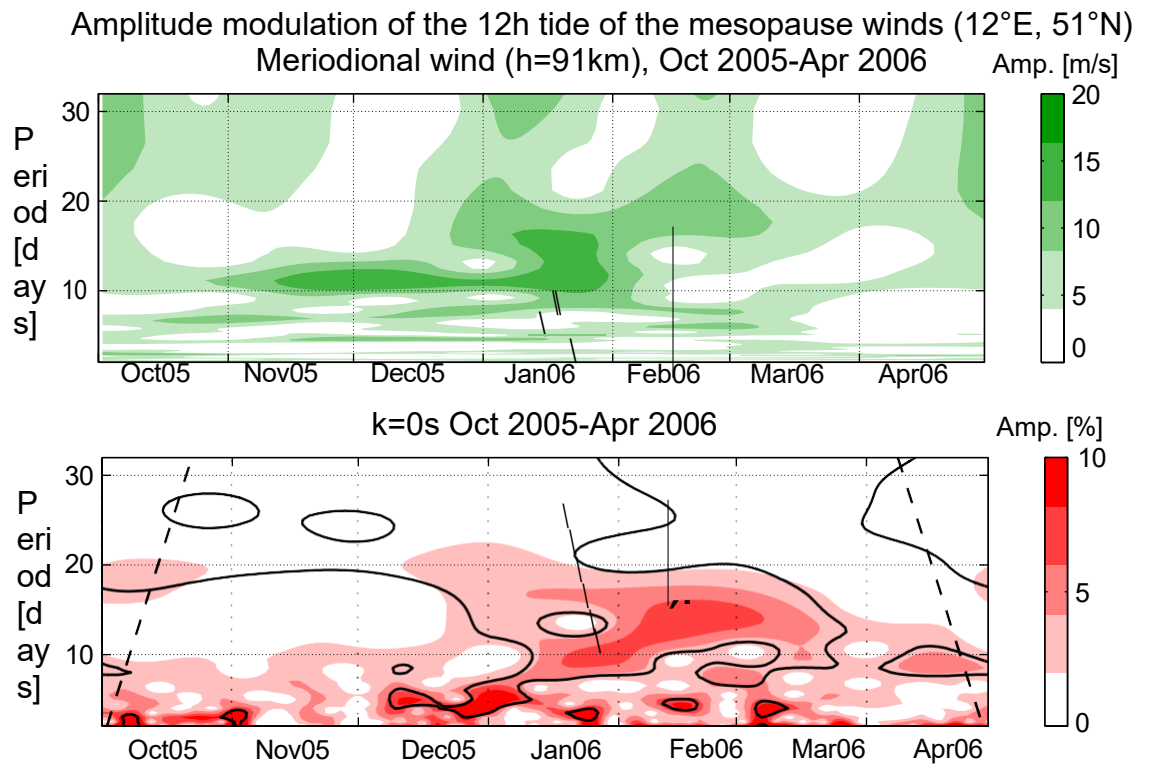


Figure 8.11.: Top: Fourier amplitude spectrum of the modulation of the semi-diurnal tide of the meridional wind at an altitude of 91km, measured with the meteor radar in Collm (13° E, 51.3° N). Bottom: Wavelet spectra of the zonal mean variation in the f_J , TEC_{rell} filter, 52.5° N. The arrows indicate simultaneous oscillations.

9. Summary and outlook

In the present work, so-called planetary wave-like oscillations (PWTO), i.e. ionospheric large-scale periodic variations with wavelengths of several thousand kilometres and periods between 2 and 30 days, were investigated. The analyses aimed to contribute to confirming or refuting the hypothesis of coupling between the middle atmosphere and the ionosphere by planetary waves (PW).

Regional hemispheric maps reflecting the total electron content (TEC) of the atmosphere in the northern hemisphere (50° N-North Pole) were used. This dataset provides new, more accurate information on the horizontal extent and movement of PWTO than previously used local measurements from ionosondes. In addition, characteristic features can be derived due to its complete availability. Because the previously available TEC maps were either not accurate enough or limited to too small regions, this data set is particularly useful for the investigation of the PWTO. Current and proven methods of spectral analysis (wavelet transform and Fourier transform) were used for the analyses. They were chosen because they are particularly well suited for discrete, equidistant data and best approximate periodic signals. In addition, they do not require any further assumptions on the signal. A combination of spatial and temporal analyses (frequency-wavenumber analysis) enabled the spectral decomposition of the data set into individual wave components characterised by their zonal wavenumber, period and zonal direction of motion. Correlation analyses between TEC and solar parameters (F10.7 and solar wind speed) revealed the significant influence of the Sun on the variation of TEC in the time scale range of days. Both the solar rotation period (27 days) and its subharmonics (13.5 days, 9 days and 7 days) could be detected in the TEC signal. Interesting seasonal dependencies in the type of correlation (correlated/anticorrelated) were observed, which could be explained by density changes and changes in ec- liptics. Further studies that expand on these observations and investigate the causes in more depth can start at this point. It was shown that the quasi-periodic signals of the solar parameters produce forced oscillations in the TEC signal. With a special filter method based on the wavelet transformation, these forced solar controlled oscillations were specifically removed from the TEC signal. The comparison of the filtered and unfiltered signal showed,

that up to 50% of the energy of the PWTO in the TEC signal (period range 2-30days) is generated by solar variations.

The filtered TEC signal was spectrally decomposed using frequency-wavenumber analysis to determine the characteristics of the oscillations remaining in the signal in the scale range of PW. The analyses showed that the PWTO have some properties in common with PW, but there are also significant differences. Common features are the wave activity maximum in winter, the preferred geographical latitudes, the movement of the waves around the geographical pole and typical periods of PW. PWTOs differ from stratospheric PWs in the dominance of zonal mid-ocean oscillations and predominantly shorter periods. However, the differences do not exclude the existence of a coupling.

There are various explanations in the literature for the coupling between the lower atmosphere and the ionosphere, some of which were empirically examined in this study. Firstly, the direct ascent of PW into the lower thermosphere, secondly the non-linear interaction between PW and thirdly the modulation of atmospheric gravity waves (AGW) were investigated. It is assumed that the transfer of PW energy to the ionosphere in the lower thermosphere occurs either via PW variation of thermospheric composition or modulation of wind dynamo. The analyses revealed some, but only limited, evidence for direct propagation of PW into the lower thermosphere. Much more evidence was found for non-linear interaction between PW. Especially the zonal centre oscillations, which dominate in the ionosphere and whose origin could not be clarified so far, can be associated with secondary waves of PW. The analysis of AGW has not detected any amplitude modulation of AGW in the lower thermosphere. This process therefore seems to play a minor role in the atmosphere-ionosphere coupling.

Ultimately, the listed results of this work lead to the conclusion that a coupling of the middle atmosphere and ionosphere by PW is possible, i.e. that a part of the energy of PW is transferred into the ionosphere. The process of nonlinear interaction between PW seems to be an essential part of the transfer process of PW energy into the ionosphere. The resulting secondary waves, which propagate to the lower thermosphere, affect either the wind dynamo of the E-region, which in turn affects the dynamo-induced E-field and vertical ion drift, or the thermospheric composition, reflecting their variation in the recombination rate. For some PW, such as the quasi-16-day wave, it is possible to propagate directly into the lower thermosphere, causing variations in the thermospheric composition there.

Despite the extensive analyses, some aspects that are part of the topic of atmosphere-ionosphere coupling by PW had to be neglected in the present work due to a lack of suitable analysis methods and data. This concerns, for example, the investigation of the effect of stratospheric warming on the coupling.

and the effect of PW on electrojets and sporadic E-layer, which can be investigated in more depth in future work. The modulation of atmospheric tides, which has already been identified as a potential coupling mechanism, is also recommended for further analysis.

Furthermore, some new topics were opened up in the present work that are worth investigating in detail. On the one hand, interesting results on the connection between solar wind and TEC were obtained in chapter 6, which should be analysed in more detail. On the other hand, chapter 8.4 has given new insights into the climatology and modulation of AGW, which can be deepened in further investigations. Because the data set used is still relatively short at the present time, future analyses over an even longer period of time may provide more and thus statistically more reliable information on the climatology of the PWTO.

List of figures

1.1. Temperature profile of the atmosphere.....	2
2.1. Temperature profile of the lower and middle atmosphere	6
2.2. Wave triangle	15
2.3. Coupling processes in the ionosphere-thermosphere system	17
3.1. Planetary wave activity in the atmosphere	26
3.2. Diagram of the coupling mechanisms	32
4.1. Mapping function to convert the sT EC into a vertical TEC	37
4.2. Data coverage of the DLR North Pole TEC map	39
4.3. DLR North Pole TEC Map	40
4.4. Comparison between DLR North Pole TEC maps, IGS TEC maps and f _{oF} -measurements of the ionosonde Juliusruh	41
5.1. Amplitude spectrum of the short-term Fourier analysis	47
5.2. Wavelet amplitude spectrum	51
6.1. 10.7cm Radio flux index, running mean and relative differences to the running mean.....	59
6.2. Wavelet amplitude spectrum of f _j ,F10.7 _{rel}	59
6.3. Wavelet amplitude spectrum of the solar wind	61
6.4. Wavelet amplitude spectrum of the Kp index.....	62
6.5. Correlation between Kp and solar wind.	63
6.6. Correlation of f _j ,TEC _{rel} with f _j ,F10.7 _{rel} , solar wind and Kp.....	64
6.7. Wavelet amplitude spectra of f _j ,TEC _{rel} and the solar variatio- Adjusted f _j ,TEC _{rel}	68
6.8. Estimation of the share of solar controlled variations in the f _j ,TEC _{rel}	69
7.1. Number of observed PWTO in f _j ,TEC _{rel} filter.....	75
7.2. RMS amplitude of the standing waves of different wavenumbers in the f _j ,TEC Wave numbers in the f _j ,TEC _{rel} filter.....	77
7.3. RMS of the amplitude of the travelling waves in the f _j ,TEC _{rel} filter	79

7.4.	RMS amplitude of the standing PWTO in the winter months in dependency- of the geographical latitude.	82
7.5.	Map grid of the geographic and geomagnetic TEC maps.	85
7.6.	Comparison between PWTO for standing waves measured in geomagnetic and geographic coordination systems.	85
7.7.	Comparison between PWTO for travelling waves measured in geomagnetic and geographic coordinate systems.....	86
8.1.	Number of PW and PWTO observed simultaneously.....	94
8.2.	Number of simultaneously observed PWTO and stratospheric waves of secondary wave type I.	97
8.3.	Number of simultaneously observed PWTO and stratospheric waves of secondary wave type III.	98
8.4.	Number of simultaneously observed PWTO and stratospheric waves of secondary wave type IV.....	99
8.5.	Variance of TID amplitudes and squared TEC.....	102
8.6.	Variance of TID amplitudes in relation to TEC.....	103
8.7.	Wavelet spectrum of TID activity.	105
8.8.	PW proxy of the zonal mean variations.....	107
8.9.	PW proxy of the stationary waves.	108
8.10.	PW proxy of travelling and standing waves.....	109
8.11.	Modulation of the semi-diurnal tide in the mesosphere.	114
A.1.	Number of observed PW in the NCEP zonal wind.....	B
A.2.	RMS amplitudes of the standing PW in the zonal wind at 10hPa.....	C
A.3.	RMS amplitude of the migrating PW in the zonal wind at 10hPa.	D
A.4.	RMS amplitude of the standing PW in the zonal wind in 10hPa.	E
A.5.	Width dependence of stationary PW.....	F
B.1.	Correlation of IGS-fj,TEC _{rel} with fj,F10.7 _{rel} , solar wind and Kp.	H
B.2.	Estimation of the proportion of solar-driven variations in fj,TEC _{rel} in IGS maps.	I
B.3.	Number of PWTO observed in IGS-fj,TEC _{rell} filter.....	K
B.4.	RMS amplitude of the standing waves of different wave numbers in the IGS- fj,TEC _{rell} filter	L
B.5.	RMS of the amplitude of the travelling waves in the IGS-fj,TEC _{rell} filter.....	M
B.6.	RMS amplitude of the standing PWTO in the winter months in dependency- of the geographical latitude.	N
B.7.	Number of PW and PWTO observed simultaneously.....	P
B.8.	Number of simultaneously observed PWTO and stratospheric waves of secondary wave type I.	Q

- B.9. Number of simultaneously observed PWTO and stratospheric waves of secondary wave type III..... R
- B.10. Number of simultaneously observed PWTO and stratospheric waves of secondary wave type IV S

Bibliography

- Abdu, M., T. Ramkumar, I. Batista, C. Brum, H. Takahashi, B. Reinisch, and J. Sobral (2006), Planetary wave signatures in the equatorial atmosphere-ionosphere system, and mesosphere- E- and F-region coupling, *Journal of Atmospheric and Solar-Terrestrial Physics*, **68**, 509-522, doi:10.1016/j.jastp.2005.03.019.
- Afraimovich, E. L., E. A. Kosogorov, L. A. Leonovich, O. S. Lesyuta, and I. I. Ushakov (2001), Novel technology for detecting atmospheric disturbances using GPS. Instantaneous response of the ionosphere to a sudden commencement of strong magnetic storms, *Advances in Space Research*, **27**(6-7), 1345-1350.
- Altadill, D. (2000), Planetary Wave Type Oscillations in the Ionospheric F-Region, *Adv. Space Res.* , **26**(8), 1287-1296.
- Altadill, D., and E. M. Apostolov (2003), Time and scale size of planetary wave signatures in the ionospheric F-region. Role of the geomagnetic activity and mesosphere/lower thermosphere winds, *J. Geophys. Res.* , **108**, A11, doi:10.1029/2003JA010015.
- Altadill, D., E. M. Apostolov, J. Solé, and C. Jacobi (2001), Origin and Development of Vertical Propagating Oscillations with Periods of Planetary Waves in the Ionospheric F Region, *Phys. Chem. Earth (C)*, **26**(6), 387-393..
- Altadill, D., E. M. Apostolov, C. Jacobi, and N. J. Mitchell (2003), Six-day westward propagating wave in the maximum electron density of the ionosphere, *Annales Geophysicae*, **21**, 1577-1588.
- Altadill, D., E. M. Apostolov, J. Boska, J. Laštovička, and P. Sauli (2004), Planetary and gravity wave signatures in the F-region ionosphere with impact on radio propagation predictions and variability, *Annals of Geophysics*, **47**(2/3), 1109-1119.
- Angelats i Coll, M., and J. M. Forbes (2002), Nonlinear interactions in the upper atmosphere- re: The $s = 1$ and $s = 3$ nonmigrating semidiurnal tides, *Journal of Geophysical Research*, **107**(A8), 1157, doi:10.1029/2001JA900179.

- Aushev, V., I. Fedulina, G. Gordienko, M. López-González, A. Pogoreltsev, S. Ryazapova, and M. Shepherd (2006), Springtime effects in the mesosphere and ionosphere observed at northern midlatitudes, *Planetary and Space Science*, 54, 559-571, doi:10.1016/j.pss.2006.01.002.
- Bachmann, K. T., H. Maymani, K. Nautiyal, and V. Te Velde (2004), An analysis of solar-cycle temporal relationships among activity indicators, *Advances in Space Research*, 34(2), 274-281, doi:10.1016/j.asr.2004.03.010.
- Bäni, W. (2002), *Wavelets : an introduction for engineers*, 1 ed., IX, 264 pp, Munich ; Vienna : Oldenbourg.
- Baran, L., I. Ephishov, and I. Shagimuratov (2001), Ionospheric Total Electron Content Behaviour During November 1997 Storm, *Phys. Chem. Earth (C)*, 26(5), 341-345.
- Barnett, J., and K. Labitzke (1990), Climatological Distribution of Planetary Waves in the Middle Atmosphere, *Advances in Space Research*, 10(12), 63-91.
- Barthlott, C. (2003), Coherent vortex structures in the atmospheric boundary layer, *Wissenschaftliche Berichte des Instituts für Meteorologie und Klimaforschung der Universität Karlsruhe*, 33.
- Beard, A. G., N. J. Mitchell, P. J. S. Williams, and M. Kunitake (1999), Non-linear inter- actions between tides and planetary waves resulting in periodic tidal variability, *Journal of Atmospheric and Solar-Terrestrial Physics*, 61, 363-376, doi:10.1016/S1364-6826(99)00003-6.
- Borries, C., and P. Hoffmann (2010), The Characteristics of F2-layer Planetary Wave Type Oscillations in Northern Middle and High Latitudes during 2002-2008, *Journal of Geophysical Research - Space Science*, 115, A00G10, doi:10.1029/2010JA015456.
- Borries, C., N. Jakowski, C. Jacobi, P. Hoffmann, and A. Pogoreltsev (2007), Spectral analysis of planetary waves seen in ionospheric total electron content (TEC) : First results using GPS differential TEC and stratospheric reanalyses, *Journal of Atmospheric and Solar-Terrestrial Physics*, 69(17-18), 2442-2451, doi:10.1016/j.jastp.2007.02.004.
- Borries, C., N. Jakowski, and V. Wilken (2009), Storm induced large scale TIDs observed in GPS derived TEC, *Annales Geophysicae*, 27(4), 1605-1612.
- Bouwer, S. D. (1992), Periodicities of solar irradiance and solar activity indices. II, *Solar Physics*, 142, 365-389, doi:10.1007/BF00151460.

- Brown, G., and J. John (1979), Vertical penetration of planetary waves into the lower ionosphere, *Journal of Atmospheric and Terrestrial Physics*, 41, 379-385.
- Buonsanto, M. (1999), Ionospheric Storms - A Review, *Space Science Reviews*, 88(3-4), 563-601, doi:10.1023/A:1005107532631.
- Buttkus, B. (1991), *Spectral analysis and filter theory in applied geophysics*, Springer.
- Cander, L. R., and S. J. Mihajlovic (2005), Ionospheric spatial and temporal variations during the 29-31 October 2003 storm, *Journal of Atmospheric and Solar-Terrestrial Physics*, 67, 1118-1128, doi:10.1016/j.jastp.2005.02.020.
- Charney, J., and P. Drazin (1961), Propagation of planetary-scale disturbances from the lower into the upper atmosphere, *Journal of Geophysical Research*, 66, 83-109.
- Daubechies, I. (1992), *Ten Lectures on Wavelets, CBMS-NSF Regional Conference Series in Applied Mathematics*, vol. 61, xx+357 pp., Society for Industrial and Applied Mathematics Philadelphia, Pennsylvania, Philadelphia, PA.
- Davies, K. (1996), Winds and Drifts, in *The Upper Atmosphere - Data Analysis and Interpretation*, edited by W. Dieminger, G. Hartmann, and R. Leitinger, 1 ed., Springer, Berlin.
- de Adler, N. O., A. G. Elías, and J. R. Manzano (1997), Solar cycle length variation: its relation with ionospheric parameters, *Journal of Atmospheric and Solar-Terrestrial Physics*, 59, 159-162, doi:10.1016/S1364-6826(96)00056-9.
- Dickinson, R. E. (1969), Vertical Propagation of Planetary Rossby Waves through an Atmosphere with Newtonian Cooling, *Journal of Geophysical Research*, 74(4), 929-938.
- Dudok de Wit, T., M. Kretzschmar, J. Aboudarham, P.-O. Amblard, F. Auchère, and J. Lilenstein (2008), Which solar EUV indices are best for reconstructing the solar EUV irradiance?, *Advances in Space Research*, 42, 903-911, doi:10.1016/j.asr.2007.04.019.
- Floyd, L., J. Newmark, J. Cook, L. Herring, and D. McMullin (2005), Solar EUV and UV spectral irradiances and solar indices, *Journal of Atmospheric and Solar-Terrestrial Physics*, 67(1-2), 3-15, doi:10.1016/j.jastp.2004.07.013.
- Forbes, J. M. (1996), Planetary Waves in the Thermosphere-Ionosphere System, *J. Geomag. Geoelectr.*, 48, 91-98.

- Forbes, J. M. (2007), Dynamics of the Thermosphere, *J. Meteorol. Soc. Japan*, **85B**, 193-213.
- Forbes, J. M., and X. Zhang (1997), Quasi 2-day oscillation of the ionosphere: A statistical study, *Journal of Atmospheric and Solar-Terrestrial Physics*, **59**(9), 1025-1034..
- Forbes, J. M., M. Hagan, S. Miyahara, F. Vial, A. Manson, C. Meek, and Y. Portnyagin (1995), Quasi 16-day oscillation in the mesosphere and lower thermosphere, *Journal of Geophysical Research*, **100**(D5), 9149-9163.
- Forbes, J. M., S. Palo, and X. Zhang (2000), Variability of the ionosphere, *Journal of Atmospheric and Solar-Terrestrial Physics*, **62**, 685-693.
- Forbes, J. M., S. L. Bruinsma, X. Zhang, and J. Oberheide (2009), Surface-exosphere coupling due to thermal tides, *Geophysical Research Letters*, **36**, L15,812, doi:10.1029/2009GL038748.
- Förster, M., and N. Jakowski (2000), Geomagnetic Storm Effects on the Topside Ionosphere and Plasmasphere: A Compact Tutorial and New Results, *Surveys in Geophysics*, **21**(1), 47-87, doi:10.1023/A:1006775125220.
- Fröhlich, C. (2005), The Quasi Two-Day Wave - its impact on the zonal mean circulation and wave-wave interactions in the middle atmosphere, Ph.D. thesis, University Leipzig.
- Gordienko, G. I., V. M. Aushev, I. N. Fedulina, S. S. Ryazapova, and M. G. Shepherd (2005), Observation of the F2-layer variability from the "Alma-Ata" observatory, *Journal of Atmospheric and Solar-Terrestrial Physics*, **67**, 563-580, doi:10.1016/j.jastp.2004.07.039.
- Habarulema, J. B., L.-A. McKinnell, and B. D. L. Opperman (2009), A recurrent neural network approach to quantitatively studying solar wind effects on TEC derived from GPS; preliminary results, *Annales Geophysicae*, **27**(5), 2111-2125.
- Hagan, M., J. M. Forbes, and F. Vial (1993), Numerical investigation of the propagation of the quasi-two-day wave into the lower thermosphere, *Journal of Geophysical Research*, **98**(D12), 23,193-23,205.
- Haldoupis, C., and D. Pancheva (2002), Planetary Waves and Midlatitude Sporadic E Layers: Strong Experimental Evidence for a Close Relationship, *Journal of Geophysical Research*, **107**, JA000,212.

- Hargreaves, J. K. (1992), *The Solar-Terrestrial Environment*, Cambridge atmospheric and space science series, 1 ed, Cambridge Univ Press.
- Hathaway, D. H. (2010), The Solar Cycle, *Living Reviews in Solar Physics*, 7, 1-+.
- Hayashi, Y. (1971), A generalized method of resolving disturbances into progressive and retrogressive waves by space Fourier and time cross-spectral analyses, *Journal of the Meteorological Society of Japan*, 49(2), 125-128.
- Hirooka, T., and I. Hirota (1985), Normal mode Rossby waves observed in the upper stratosphere, Part II: Second antisymmetric and symmetric modes of wavenumbers 1 and 2, *Journal of Atmospheric Science*, 42(6), 536-548.
- Hirota, I., and T. Hirooka (1984), Normal mode Rossby waves observed in the upper stratosphere, Part I: First symmetric modes of zonal wavenumbers 1 and 2, *Journal of Atmospheric Science*, 41(8), 1253-1264.
- Holton, J. (1972), *An Introduction to Dynamic Meteorology*, 1 ed., Academic Press, New York and London.
- Hong, S.-S., and R. D. Lindzen (1976), Solar semidiurnal tide in the thermosphere, *Journal of Atmospheric Sciences*, 33, 135-153.
- Horton, W., T. D. Kaladze, J. W. Van Dam, and T. W. Garner (2008), Zonal flow generation by internal gravity waves in the atmosphere, *Journal of Geophysical Research (Space Physics)*, 113(A12), 8312-+, doi:10.1029/2007JA012952.
- Huang, C. M., S. D. Zhang, and F. Yi (2009), Intensive radiosonde observations of the diurnal tide and planetary waves in the lower atmosphere over Yichang ($111^{\circ} 18' E$, $30^{\circ} 42' N$), China, *Annales Geophysicae*, 27, 1079-1095.
- Hunt, B. G. (1984), Some wave characteristics of the middle atmosphere simulated in a general circulation model extending from the surface to 100 km, *The Quarterly Journal of the Royal Meteorological Society*, 110(463), 187 - 202, doi:10.1002/qj.49711046313.
- Immel, T. J., S. B. Mende, M. E. Hagan, P. M. Kintner, and S. L. England (2009), Evidence of Tropospheric Effects on the Ionosphere, *EOS Transactions*, 90, 69-70, doi:10.1029/2009EO090001.
- Ito, R., S. Kato, and T. Tsuda (1986), Consideration of an Ionospheric Wind Dynamo Driven by a Planetary Wave with a Two-Day Period, *J. Atmos. Terr. Phys.*, 48, 1-14.

- Jacobi, C., and D. Kürschner (2007), Interannual variability of the quasi two-day wave over Central Europe (52° N, 15° E), *Wiss. Mitteil. Inst. f. Meteorol. Univ. Leipzig*, 41, 17-26.
- Jacobi, C., R. Schminder, and D. Kürschner (1998), Planetary wave activity obtained from long-period (2-18 days) variations of mesopause region winds over Central Europe (52° N, 15° E), *Journal of Atmospheric and Solar-Terrestrial Physics*, 60(1), 81-93.
- Jacobi, C., N. M. Gavrilov, D. Kürschner, and K. Fröhlich (2006), Gravity wave climatology and trends in the mesosphere/lower thermosphere region deduced from low-frequency drift measurements 1984-2003 (52.11N, 13.21E), *Journal of Atmospheric and Solar-Terrestrial Physics*, 68, 1913-1923, doi:10.1016/j.jastp.2005.12.007.
- Jacobi, C., N. Jakowski, A. Pogoreltsev, K. Fröhlich, P. Hoffmann, and C. Borries (2007), The CPW-TEC project: Planetary waves in the middle atmosphere and ionosphere, *Advances in Radio Science*, 5, 393-397.
- Jakowski, N. (1996), TEC Monitoring by Using Satellite Positioning Systems, in *Modern Ionospheric Science*, edited by H. Kohl, R. Rüster, and K. Schlegel, 1 ed., pp. 371-390, European Geophysical Society.
- Jakowski, N., and E. Paasch (1984), Report on the observations of the total electron content on the ionosphere in Neustrelitz/GDR from 1976 to 1980, *Annales Geophysicae*, 2(4), 501-504.
- Jakowski, N., and S. Schlüter (1999), Ionospheric storms detected by GPS based TEC monitoring, in *COST 251/Workshop on "Procedures and Testing of the Models for Ionospheric Telecommunications Application"*, pp. 103-107.
- Jakowski, N., B. Fichtelmann, and A. Jungstand (1991), Solar Activity Control of Ionospheric and Thermospheric Processes, *Journal of Atmospheric and Terrestrial Physics*, 53(11/12), 1125-1130.
- Juusola, L., K. Kauristie, O. Amm, and P. Ritter (2009), Statistical dependence of auroral ionospheric currents on solar wind and geomagnetic parameters from 5 years of CHAMP satellite data, *Annales Geophysicae*, 27(3), 1005-1017.
- Kaiser, G. (1994), *A Friendly Guide to Wavelets*, 1 ed., 300 pp, Birkhäuser, Boston, Basel, Berlin.
- Kane, R. P., E. R. de Paula, and N. B. Trivedi (1995), Variations of solar EUV, UV and ionospheric foF2 related to the solar rotation period, *Annales Geophysicae*, 13(7), 717-723.

Labitzke, K., and H. van Loon (1992), Climatology of the middle atmosphere: observations up to 80km altitude, *ProMet*, 22(2-4), 45-49.

Langematz, U., and S. Pawson (1992), Climatology of the middle atmosphere, *ProMet*, 22(2-4), 50-57.

Lašovicčka, J. (1997), Observations of Tides and Planetary Waves in the Atmosphere- Ionosphere System, *Advances in Space Research*, 20(6), 1209-1222.

Lašovicčka, J. (2001), Effects of Gravity and Planetary Waves on the Lower Ionosphere as Obtained from Radio Wave Absorption Measurements, *Phy. Chem. Earth (B)*, 26(6), 381-386.

Lašovicčka, J. (2006), Forcing of the ionosphere by waves from below, *Journal of Atmospheric and Solar-Terrestrial Physics*, 68(3-5), 479-497, doi:10.1016/j.jastp.2005.01.018.

Lašovicčka, J., and P. Sauli (1999), Are planetary wave type oscillations in the F2 region caused by planetary wave modulation of upward propagating tides?, *Advances in Space Research*, 24(11), 1473-1476.

Lašovicčka, J., P. Krizan, P. Sauli, and D. Novotna (2003), Persistence of the planetary wave type oscillations in foF2 over Europe, *Annales Geophysicae*, 21, 1543-1552.

Lašovicčka, J., P. Sauli, and P. Krizan (2006), Persistence of planetary wave type oscillations in the midlatitude ionosphere, *Annals of Geophysics*, 49(6), 1235-1246.

Lawrence, A., and M. Jarvis (2003), Simultaneous observations of planetary waves from 30 to 220 km, *Journal of Atmospheric and Solar-Terrestrial Physics*, 65, 765-777, doi: 10.1016/S1364-6826(03)00081-6.

Lei, J., J. Thayer, J. M. Forbes, Q. Wu, C. She, W. Wan, and W. Wang (2008), Ionosphere response to solar wind high-speed streams, *Geophysical Research Letters*, 35, L19,105, doi:10.1029/2008GL035208.

Lindzen, R. D. (1967), Planetary waves on beta planes, *Monthly Weather Review*, 95, 441- 451.

Lindzen, R. D. (1990), The Atmosphere - A Challenge, A memorial to Jule Charney, in *Historical Monograph Series of the Am. Meteor. Soc.* , edited by R. Lindzen, E. Lorenz, and G. Platzman, 1 ed.

- Liu, H.-L., W. Wang, A. D. Richmond, and R. G. Roble (2010a), Ionospheric variability due to planetary waves and tides for solar minimum conditions, *Journal of Geophysical Research*, 115, A00G01, doi:10.1029/2009JA015188.
- Liu, J., B. Zhao, and L. Liu (2010b), Time delay and duration of ionospheric total electron content responses to geomagnetic disturbances, *Annales Geophysicae*, 28(3), 795-805.
- Madden, R. (1979), Observations of large-scale travelling waves, *Rev. Geophys. Space Phys.*, 17, 1935.
- Madden, R., and K. Labitzke (1981), A free Rossby wave in the troposphere and stratosphere during January 1979, *Journal of Geophysical Research*, 86, 1247-1254.
- Manson, A., C. Meek, Y. Luo, W. Hocking, J. MacDougall, D. Riggin, D. Fritts, and R. Vincent (2003), Modulation of gravity waves by planetary waves (2 and 16 d): observations with the North American-Pacific MLT-MFR radar network, *Journal of Atmospheric and Solar-Terrestrial Physics*, 65, 85-104.
- Manson, A. H., and C. E. Meek (1990), Long period (about 8-20 h) wind oscillations in the upper middle atmosphere at Saskatoon (55 deg N) - Evidence for non-linear tidal effects, *Planetary and Space Science*, 38, 1431-1441, doi:10.1016/0032-0633(90)90118-A.
- Maraun, D., and J. Kurths (2004), Cross wavelet analysis: significance testing and pitfalls, *Nonlinear Processes in Geophysics*, 11, 505-514.
- Mayr, H., J. Mengel, E. Talaat, H. Porter, and K. Chan (2004), Modeling study of mesospheric planetary waves: genesis and characteristics, *Annales Geophysicae*, 22, 1885-1902.
- Meyer, C., and J. Forbes (1997), Natural oscillations of the ionosphere-thermosphere-mesosphere (ITM) system, *Journal of Atmospheric and Solar-Terrestrial Physics*, 59(17), 2185-2202.
- Meyer, C. K. (1999), Gravity wave interactions with mesospheric planetary waves: A mechanism for penetration into the thermosphere-ionosphere system, *Journal of Geophysical Research*, 104(A12), 28,181-28,196, doi:10.1029/1999JA900346.
- Mikhailov, A. (1983), A Possible Mechanism of In-Phase Variation of Electron Density in the E and F2 Regions of the Ionosphere, *Geomagn. Aeron.*, 23, 557-561.
- Mitchell, N., P. Williams, and A. Beard (1996), Nonlinear Planetary/Tidal Wave Interactions in the Lower Thermosphere Observed by Meteor Radar, *Ann. Geophys.*,

14, 364-366.

- Mlynczak, M. G., F. J. Martin-Torres, C. J. Mertens, B. T. Marshall, R. E. Thompson, J. U. Kozyra, E. E. Remsberg, L. L. Gordley, J. M. R. III, and T. Woods (2008), Solar-terrestrial coupling evidenced by periodic behaviour in geomagnetic indexes and the infrared energy budget of the thermosphere, *Geophysical Research Letters*, 35, L05,808, doi:10.1029/2007GL032620.
- Mukhtarov, P., B. Andonov, C. Borries, D. Pancheva, and N. Jakowski (2010), Forcing of the ionosphere from above and below during the Arctic winter of 2005/2006, *Journal of Atmospheric and Solar-Terrestrial Physics*, 72(2-3), 193-205, doi:10.1016/j.jastp.2009.11.008.
- Offermann, D., M. Jarisch, H. Schmidt, J. Oberheide, K. Grossmann, O. Gusev, J. Russell III, and M. Mlynczak (2007), The "wave turbopause", *Journal of Atmospheric and Solar-Terrestrial Physics*, 69(17-18), 2139-2158, doi:10.1016/j.jastp.2007.05.012.
- Oinats, A. V., K. G. Ratovsky, and G. V. Kotovich (2008), Influence of the 27-day solar flux variations on the ionosphere parameters measured at Irkutsk in 2003-2005, *Advances in Space Research*, 42(4), 639-644, doi:10.1016/j.asr.2008.02.009.
- Palmroth, M., T. I. Pulkkinen, J. Polvi, A. Viljanen, and P. Janhunen (2009), On the response of ionospheric electrojets to solar wind discontinuities, *Annales Geophysicae*, 27(10), 3791-3803.
- Palo, S. E., R. G. Roble, and H. M. E. (1999), Middle atmosphere effects of the quasi two-day wave determined from a General Circulation Model, *Earth Planets Space*, 51, 629-647.
- Pancheva, D., and I. Lysenko (1988), Quasi-two-day fluctuations observed in the summer F-region electron maximum, *Bulg. Geophys. J.*, 24(2), 41-51.
- Pancheva, D., A. Beard, N. Mitchell, and H. Muller (2000), Nonlinear interactions between planetary waves in the mesosphere/ lower-thermosphere region, *Journal of Geophysical Research*, 105(A1), 157-170.
- Pancheva, D., N. J. Mitchell, R. Clark, J. Drobjeva, and J. Laštovička (2002), Variability in the maximum height of the ionospheric F2-layer over Millstone Hill (September 1998- March 2000); influence from below and above, *Annales Geophysicae*, 20, 1807-1819.
- Pancheva, D., P. Mukhtarov, and B. Andonov (2007), Zonally symmetric oscillations in the Northern Hemisphere stratosphere during the winter of 2003-2004, *Geophysical Research Letters*, 34, L04,807, doi:10.1029/2006GL028666.

- Pancheva, D., P. Mukhtarov, N. J. Mitchell, B. Andonov, E. Merzlyakov, W. Singer, Y. Murayama, S. Kawamura, J. Xiong, W. Wan, W. Hocking, D. Fritts, D. Riggan, C. Meek, and A. Manson (2008a), Latitudinal wave coupling of the stratosphere and mesosphere during the major stratospheric warming in 2003/2004, *Ann. Geophys.*, 26, 467-483.
- Pancheva, D., P. Mukhtarov, N. Mitchell, D. Fritts, D. Riggan, H. Takahashi, P. Batista, B. Clemesha, S. Gurubaran, and G. Ramkumar (2008b), Planetary wave coupling (5-6-day waves) in the low-latitude atmosphere-ionosphere system, *Journal of Atmospheric and Solar-Terrestrial Physics*, 70, 101-122, doi:10.1016/j.jastp.2007.05.014.
- Pancheva, D., P. Mukhtarov, B. Andonov, N. Mitchell, and J. Forbes (2009), Planetary waves observed by TIMED/SABER in coupling the stratosphere-mesosphere-lower thermosphere during the winter of 2003/2004: Part 2-Altitude and latitude planetary wave structure, *Journal of Atmospheric and Solar-Terrestrial Physics*, 71(1), 75-87, doi: 10.1016/j.jastp.2008.09.027.
- Pancheva, D., P. Mukhtarov, B. Andonov, and J. M. Forbes (2010), Global distribution and climatological features of the 5-6-day planetary waves seen in the SABER/TIMED temperatures (2002-2007), *Journal of Atmospheric and Solar-Terrestrial Physics*, 72, 26- 37, doi:10.1016/j.jastp.2009.10.005.
- Pancheva, D. V., P. J. Mukhtarov, M. G. Shepherd, N. J. Mitchell, D. C. Fritts, D. M. Riggan, S. J. Franke, P. P. Batista, M. A. Abdu, I. S. Batista, B. R. Clemesha, and T. Kikuchi (2006), Two-day wave coupling of the low-latitude atmosphere-ionosphere system, *J. Geophys. Res.*, 111, A07,313, doi:10.1029/2005JA011562.
- Pendlebury, D., T. G. Shepherd, M. Pritchard, and C. McLandress (2007), Normal mode rossby waves and their effects on chemical composition in the late summer stratosphere, *Atmos. Chem. Phys. Discuss.*, 7, 12,011-12,033.
- Perlitz, J., and N. Harnik (2003), Observational Evidence of a Stratospheric Influence on the Troposphere by Planetary Wave Reflection, *Journal of Climate*, 16, 3011-3026.
- Pogoreltsev, A., A. A. Vlasov, K. Fröhlich, and C. Jacobi (2007), Planetary waves in coupling the lower and upper atmosphere, *Journal of Atmospheric and Solar-Terrestrial Physics*, 69(17-18), 2083-2101, doi:doi 10.1016/j.jastp.2007.05.014.
- Prölss, G. W. (2004), *Physics of Near-Earth Space - an Introduction*, 2 ed., XV, 529 pp., Springer, Berlin [u.a.]

Richmond, A. (1995), Ionospheric Electrodynamics Using Magnetic Apex Coordinates, *J. Geomag. Geoelectr.*, 47, 191-212.

Rishbeth, H. (2006), F-region links with the lower atmosphere?, *Journal of Atmospheric and Solar-Terrestrial Physics*, 68(3-5), 469-478, doi:10.1016/j.jastp.2005.03.017.

Rodger, A., and M. Jarvis (2000), Ionospheric research 50 years ago, today and tomorrow, *Journal of Atmospheric and Solar-Terrestrial Physics*, 62, 1629-1645.

Rodgers, C. (1976), Evidence for the 5-day wave in the upper stratosphere, *Journal of Atmospheric Science*, 33, 710-711.

Saito, A., M. Nischimura, M. Yamamoto, S. Fukao, T. Tsugawa, Y. Otsuka, S. Miyazaki, and M. Kelley (2002), Observations of travelling ionospheric disturbances and 3-m scale irregularities in the nighttime F-region ionosphere with the MU radar and a GPS network, *Earth, Planets Space*, 54(1), 31-44.

Saito, S., M. Yamamoto, H. Hashiguchi, A. Maegawa, and A. Saito (2007), Observational evidence of coupling between quasi-periodic echoes and medium scale travelling ionospheric disturbances, *Annales Geophysicae*, 25, 2185-2194.

Salby, M. L. (1981), Rossby normal modes in nonuniform background configurations. Part II: equinox and solstice conditions, *Journal of Atmospheric Sciences*, 38, 1827-1840.

Salby, M. L. (1984), Survey of planetary-scale travelling waves: the state of theory and observations, *Rev. Geophys. Space Phys.*, 22, 209.

Sardón, E., A. Rius, and N. Zarraoa (1994), Estimation of the transmitter and receiver differential biases and the ionospheric total electron content from Global Positioning System observations, *Radio Science*, 29(3), 577-586.

Schunk, R. W., and A. F. Nagy (2000), *Ionospheres*, 1 ed., 572 pp, Cambridge University Press.

Sehnal, L. (1987), Semi-annual variation of the thermospheric density, *Advances in Space Research*, 7, 199-202, doi:10.1016/0273-1177(87)90092-5.

Shalimov, S., and V. Lapshin (2003), Dynamics of Planetary Waves in the Ionosphere as Observed from GPS Satellites, *Cosmic Research*, 41(3), 216-220.

- Smith, E. V. P., and D. M. Gottlieb (1975), Solar flux and its variations, *NASA Special Publication*, 366, 97-117.
- Song, H. Q., Y. Chen, K. Liu, S. W. Feng, and L. D. Xia (2009), Quasi-Periodic Releases of Streamer Blobs and Velocity Variability of the Slow Solar Wind near the Sun, *Solar Physics*, 258, 129-140, doi:10.1007/s11207-009-9411-0.
- Speth, P., and R. Madden (1983), Space-time spectral analyses of northern hemisphere peopotential heights, *Journal of the Atmospheric Sciences*, 40, 1086-1100.
- Tawadrous, M. Y. (1989), Comparison of observed and modelled semi-annual thermospheric density variations, *Bulletin of the Astronomical Institutes of Czechoslovakia*, 40, 28-30.
- Teitelbaum, H., and F. Vial (1991), On tidal variability induced by nonlinear interaction with planetary waves, *Journal of Geophysical Research*, 96, 14,169-+, doi:10.1029/91JA01019.
- Torrence, C., and G. Compo (1998), A Practical Guide to Wavelet Analysis, *Bulletin of the American Meteorological Society*, 79(1), 61-78.
- Tsugawa, T., N. Kotake, Y. Otsuka, and A. Saito (2007), Medium-scale travelling ionospheric disturbances observed by GPS receiver network in Japan: a short review, *GPS Solutions*, 11, 139-144, doi:10.1007/s10291-006-0045-5.
- Tsybulya, K. (2005), Detection and Analysis of the Ionospheric Electron Density Structures Using GPS Radio Occultations onboard the CHAMP Satellite, Ph.D. thesis, University Leipzig.
- Vadas, S. L., and H. Liu (2009), Generation of large-scale gravity waves and neutral winds in the thermosphere from the dissipation of convectively generated gravity waves, *Journal of Geophysical Research (Space Physics)*, 114, 10,310-+, doi:10.1029/2009JA014108.
- Vellante, M., M. Förster, U. Villante, T. L. Zhang, and W. Magnes (2007), Solar activity dependence of geomagnetic field line resonance frequencies at low latitudes, *Journal of Geophysical Research*, 112(A02205), 1-14.
- Volland, H. (1988), *Atmospheric Tidal and Planetary Waves*, Atmospheric Science Library, 1 ed, 348 pp, Kluwer Academic Publishers.
- Wüst, S. (2008), Interactions between atmospheric gravity waves, *planeta-*.

The effects of the DYANA campaign on the waves and the base flow, Ph.D. thesis, University of Augsburg.

Xiong, J., W. Wan, B. Ning, L. Liu, and Y. Gao (2006), Planetary wave-type oscillations in the ionosphere and their relationship to mesospheric/lower thermospheric and geomagnetic disturbances at Wuhan (30.6° N, 114.5° E), *Journal of Atmospheric and Solar-Terrestrial Physics*, **68**(3-5), 498 - 508, doi:DOI 10 1016/j.jastp 2005 03 018.

Yun, W.-T. (1996), Changes in transient waves and excitation mechanisms due to anthropogenic influences, Ph.D. thesis, University of Cologne.

Zhang, Y., W. Sun, X. Feng, C. Deehr, C. Fry, and M. Dryer (2008), Statistical analysis of corotating interaction regions and their geoeffectiveness during solar cycle 23, *Journal of Geophysical Research*, **113**, A08,106, doi:10 1029/2008JA013095.

Zykov, E. Y., O. N. Sherstyukov, and A. D. Akchurin (2009), Effects of planetary waves in parameters of the midlatitude sporadic E layer, *Geomagnetism and Aeronomy/Geomagnetizm i Aeronomiya*, **49**, 519-523, doi:10 1134/S0016793209040136.

Acknowledgement

Many people supported me in the preparation of this work, and I would like to take this opportunity to thank them most sincerely.

I would like to thank Prof. Dr. Langematz for her willingness to accompany my doctorate as first examiner and doctoral supervisor, for the comprehensive professional supervision and the warm welcome she gave me in her team. I would also like to thank Prof. Dr. Jacobi for taking on the co-advisory role and for his excellent professional support on middle and upper atmosphere topics throughout my doctorate.

My special thanks go to Prof. Dr. Teschke, not only for the good training in the field of signal analysis, but also for his trust in me and the opening of free space to work on my dissertation. I would like to thank Dr. Jakowski most sincerely for his trust in my work, his always open ear for questions and problems and his constructive criticism when reading my manuscripts. I would like to thank my colleagues at DLR-IKN for their interest and numerous suggestions, especially Dr Wilken and Dr Mayer.

Discussions at conferences have been a decisive orientation for me and have always given my work some guidance in the right direction. I would like to thank Prof. Dr. Pancheva, Prof. Dr. Forbes and Prof. Dr. Holschneider in particular for their valuable suggestions.

My heartfelt thanks go to my family, who have read my work more than once, even though they do not have as much interest in and understanding of the ionosphere and upper atmosphere as I do. My very special thanks go to my sweetheart Marc, who put up with my frustrating moments and always gave me courage and hope to keep working. Finally, I would like to thank Prof. Dr. Wehrenpfennig for his efforts to inspire me to do a doctorate. Without his encouragement, I probably would not have started the doctorate.

In the present work, data from various institutions/persons are used, for whose provision I would like to express my gratitude at this point. The F10.7 and Kp index are kindly provided by the National Geophysical Data Center, which is part of the National Oceanic & Atmospheric Administration (NOAA) ([ftp://
ftp.ngdc.noaa.gov/STP/GEOGRAPHIC_DATA/INDICES/KP_AP/](ftp://ftp.ngdc.noaa.gov/STP/GEOGRAPHIC_DATA/INDICES/KP_AP/)). The Space Physics Cen-

ter of the University of California makes the solar wind data of the Solar Wind Experiment available on the IGPP Solar Wind Data Server (<http://www-ssc.igpp.ucla.edu>). The NO- AA/OAR/ESRL PSD, Boulder, Colorado, USA, publishes stratospheric reanalysis data on their web page <http://www.esrl.noaa.gov/psd/>. The gravity wave analyses of the SABER data were calculated and made available by P. Hoffmann (University of Leipzig).

I would like to thank the Deutsche Forschungsgemeinschaft for the support provided by Grants JA 836/24-1 and JA 640/5-1.

A. FK spectra from stratospheric data

NCEP reanalysis data are used to analyse stratospheric PW activity. The data are provided in 17 different pressure levels in a global grid with $2.5 \times 2.5^{\circ}$ resolution in length and width and a temporal resolution of 1 day by NOAA/OAR/ESRL PSD, Boulder, Colorado, USA. The zonal wind data in 10hPa are used as representative data for the spectral analyses presented here. The same analyses are carried out for the same geographical region as in Chapter 7. The climatology determined here does not have to correspond exactly to the climatology of PW activity in the stratosphere known from the literature, because the period studied is relatively short and therefore not representative.

A. *FK spectra from stratospheric data*

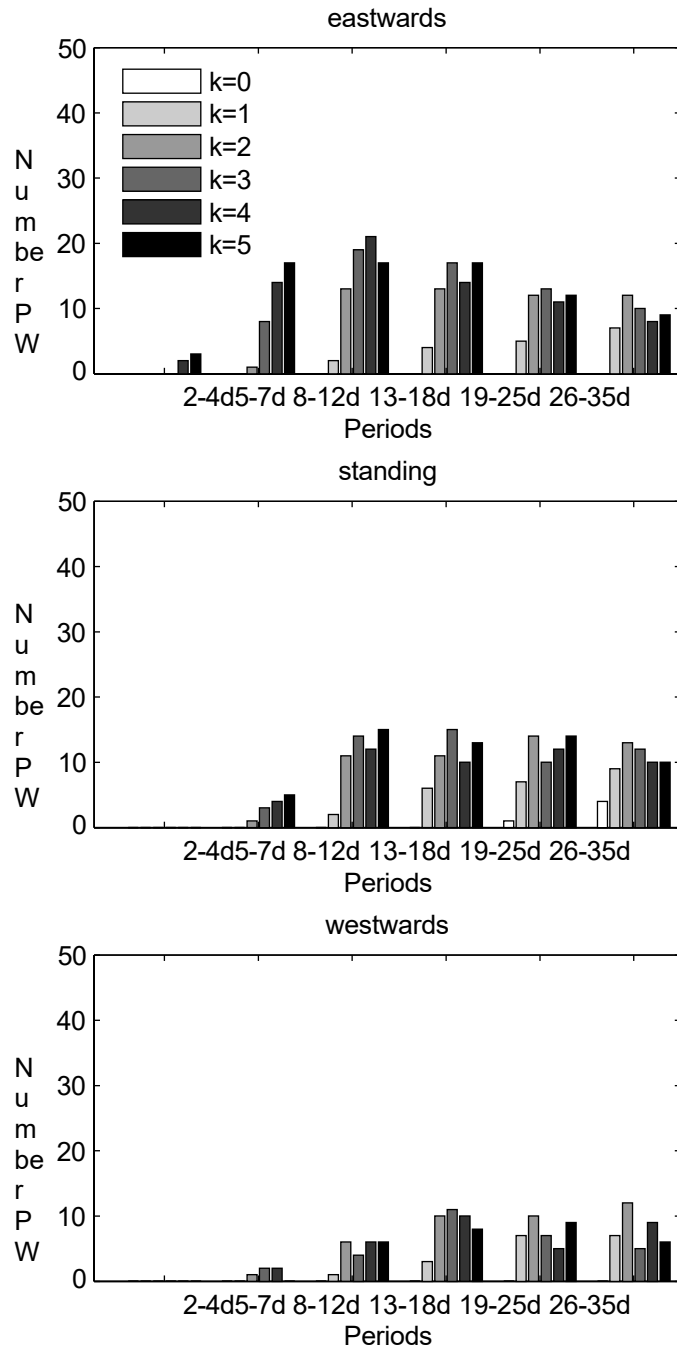


Figure A.1: Number of observed PW in the NCEP zonal wind, 10hPa, in 55° N, 2002-2008, differentiated by wave number and period class. Top: eastward moving PW; middle: stationary PW; bottom: westward moving PW. The grey values of the columns mark the wave number.

B

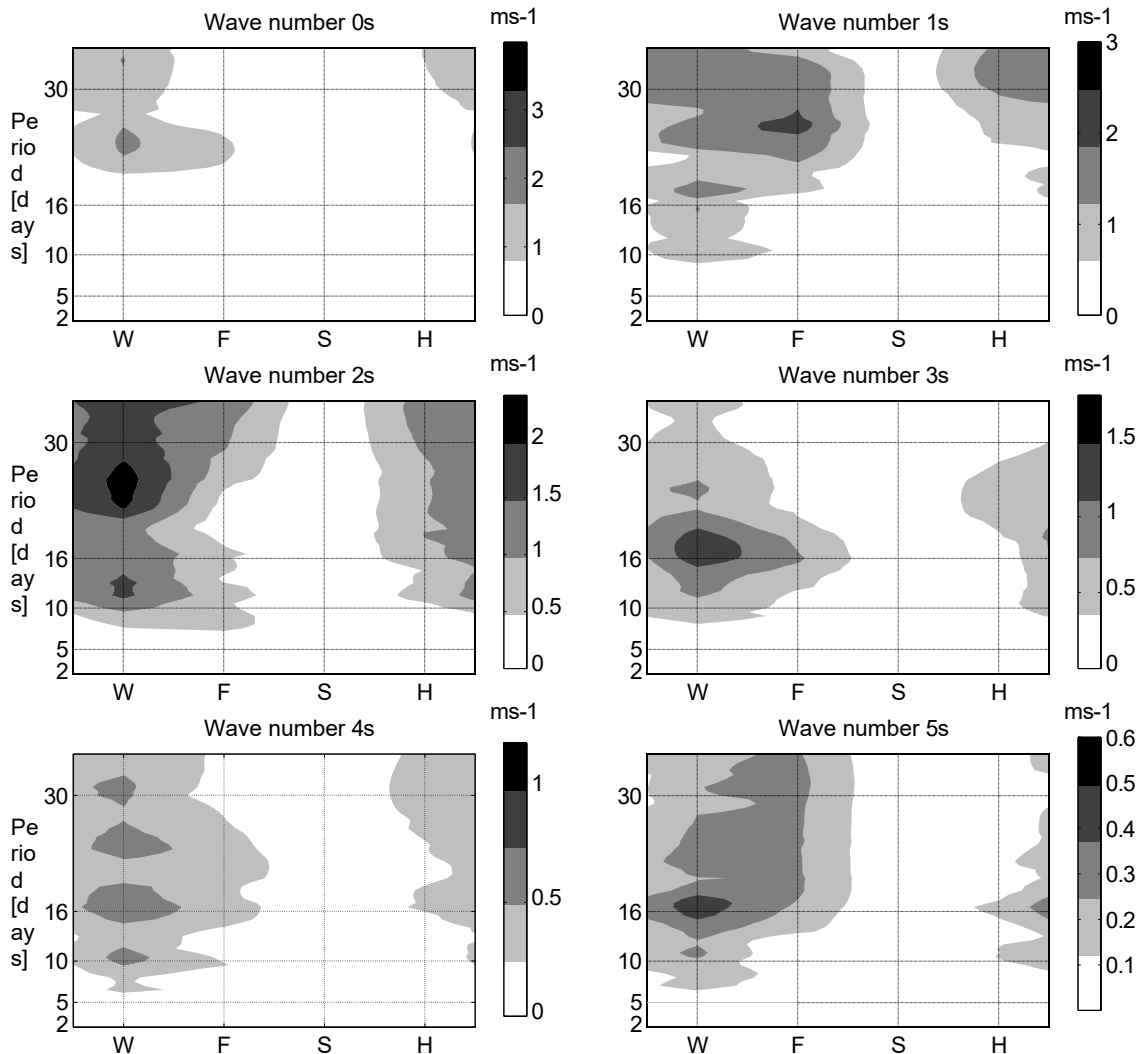
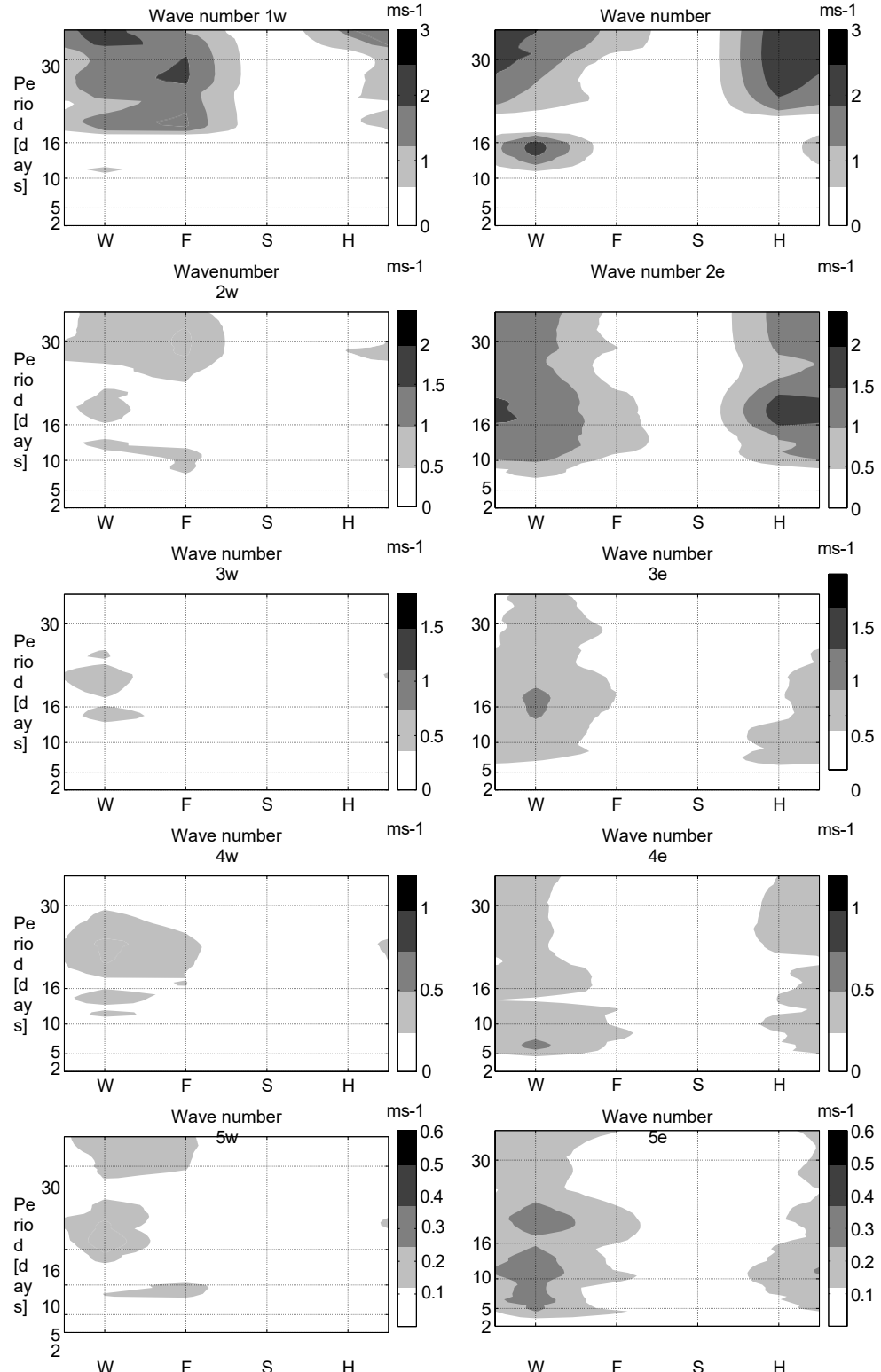


Figure A.2.: RMS of the amplitude of standing waves of different wavenumbers at 55° N observed in the zonal wind at 10hPa (NCEP reanalyses, 2002-2008) as a function of season (W: winter, F: spring, S: summer, H: autumn).

A. FK spectra from stratospheric data



D Figure A.3.: RMS of the amplitude of the travelling waves at 55° N observed in the zonal wind at 10hPa (NCEP reanalyses, 2002-2008) during of the different seasons.

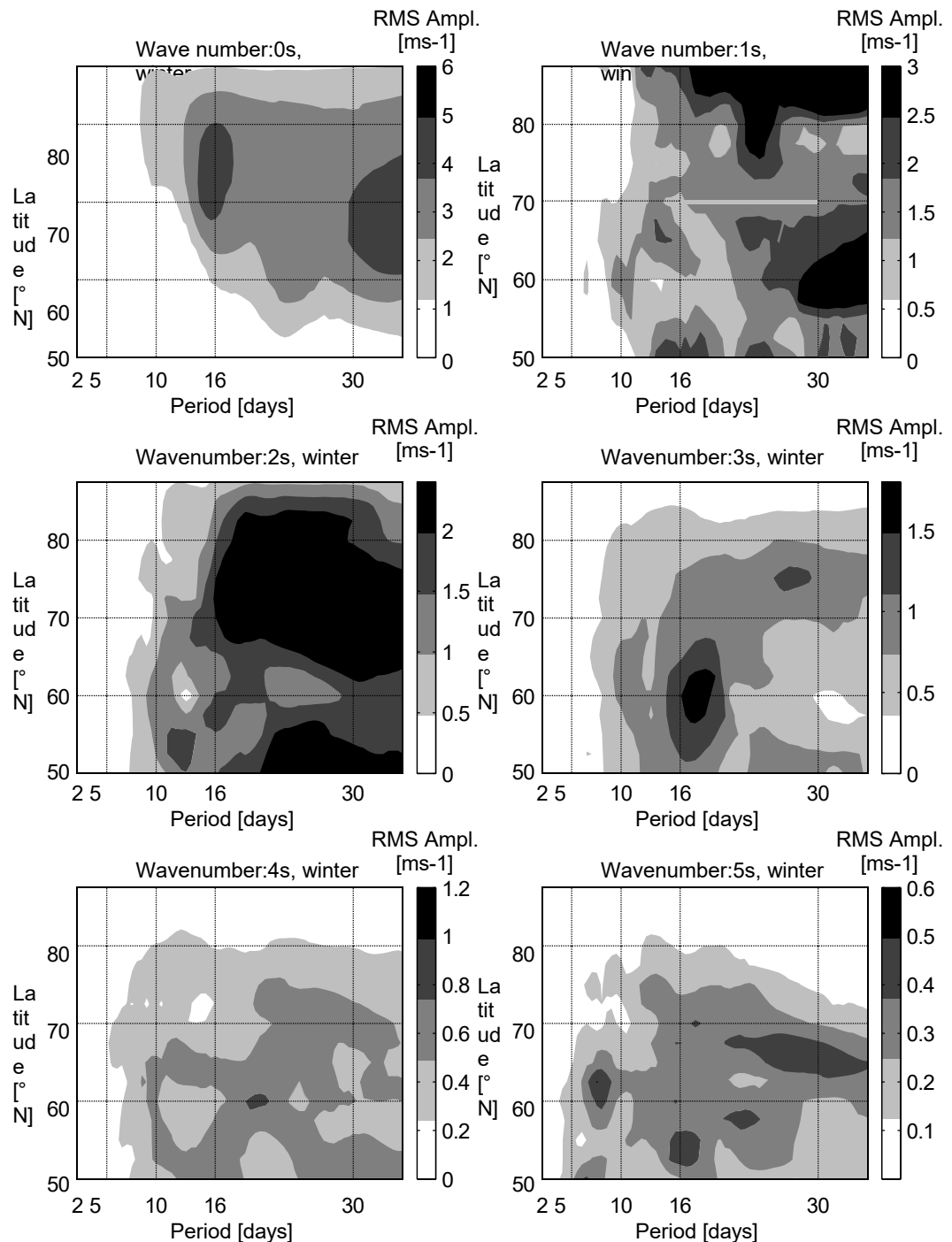


Figure A.4: RMS amplitude of standing PW in the winter months December-February as a function of geographical latitude. Observed in NCEP reanalyses of the zonal wind at 10hPa, 2002- 2008.

A. *FK spectra from stratospheric data*

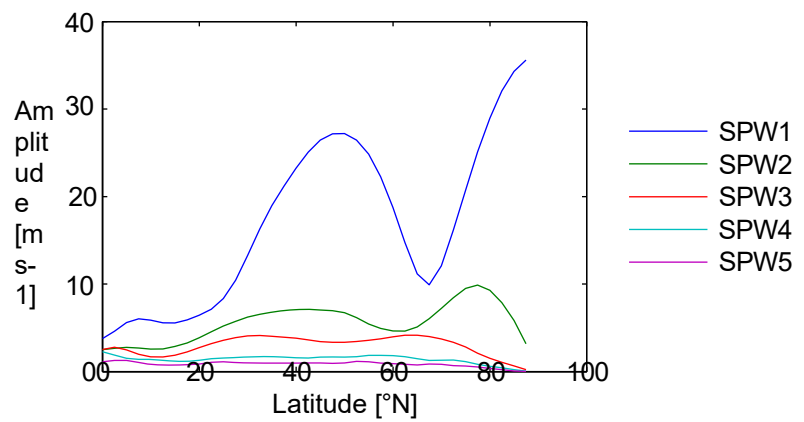


Figure A.5.: Width dependence of the stationary PW in the zonal wind (10hPa) for wavenumbers 1 (blue) to 5 (violet).

B. Analyses of the IGS-TEC maps

The analyses described in Chapters 6 to 8 are carried out in parallel with IGS-TEC maps. The results are presented in sections B.1 to B.3.

The TEC maps provided by the International GNSS Service (IGS) are the weighted average of TEC maps produced at four different facilities: the

"Centre for Orbit Determination in Europe (CODE) at the University of Bern in Switzerland, the European Space Operations Centre Ionosphere Monitoring Facility of ESA in Darmstadt, the Ionospheric and Atmospheric Remote Sensing Group at the Jet Propulsion Laboratory (JPL) in Pasadena, California, USA, and the Research Group of Astronomy and Geomatics at the Technical University of Catalonia (UPC) in Barcelona, Spain. The weighting is based on the one hand on the comparison of the slant TEC of a small number of IGS stations and on the other hand on the result of an external self-consistency validation. The IGS TEC maps have been routinely validated with TOPEX altimeter measurements since 2001. They are produced with a temporal resolution of 2 hours and a grid size of 2.5° in width and 5° in length.

B.1. TEC variations with solar origin

The correlation between TEC and solar parameters is shown in Fig. B.1. The share of solar variation in the $f_{j, \text{TEC}_{\text{rel}}}$ is shown in Fig. B.2.

B. Analyses of the IGS-TEC maps

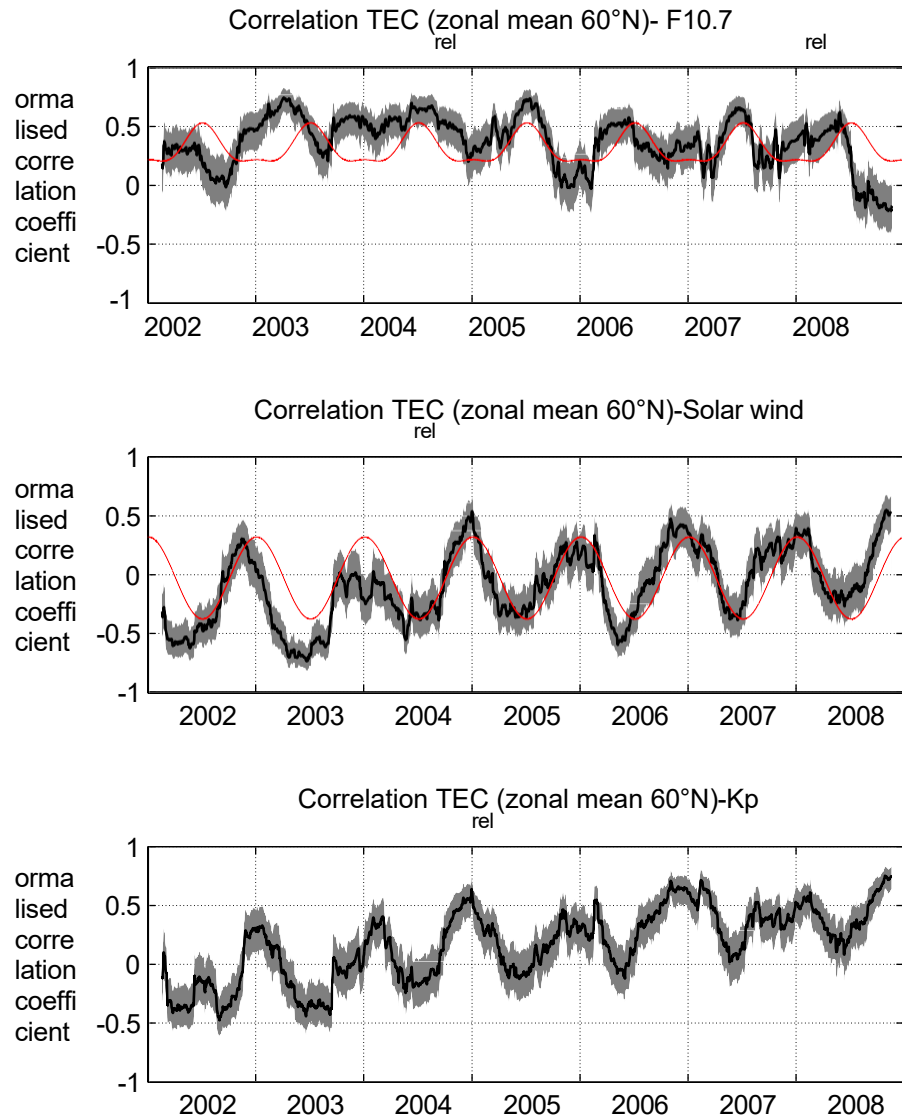


Figure B.1.: Correlation of IGS-fj,TEC_{rel} (zonal mean 60° N) with f_j,F10.7_{rel} (top), IGS-fj,TEC_{rel} with absolute solar wind speed (middle) and IGS-fj,TEC_{rel} with Kp (bottom). The correlation was calculated under a sliding window with the window length 90 days. The grey shading indicates the confidence interval 95% significance. Red curves show the least squares models of the correlation values. The vertical grid lines indicate the change of year (1 January).

B.1. TEC variations with solar origin

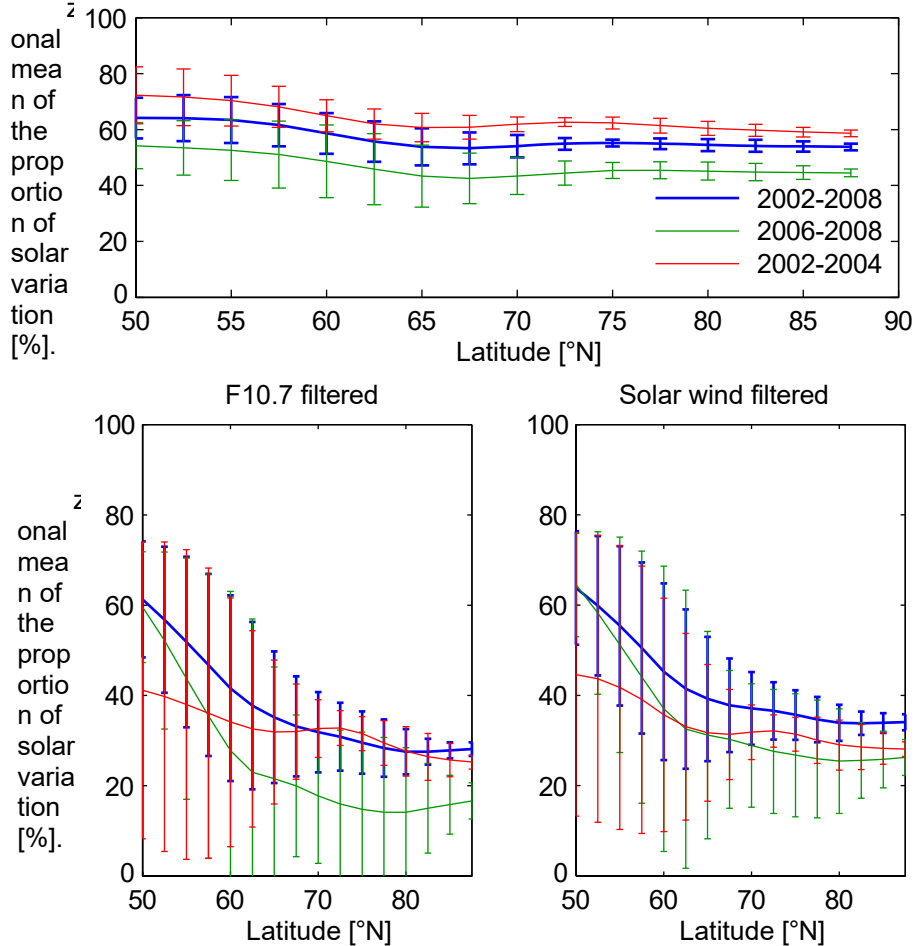


Figure B.2: Estimation of the proportion of solar-driven variations in the $f_{\text{J}} \text{TEC}_{\text{rel}}$ in IGS maps as a function of latitude. The zonally averaged share is shown in each case. Top: Filtering of F10.7, solar wind and K_p, mean of the years 2002-2008 (blue), mean in solar minimum 2006-2008 (green); mean in solar maximum 2002-2004 (red); Bottom left: the filtering of F10.7 alone; Bottom right: the filtering of solar wind alone. The standard deviation is shown with bars.

*B. Analyses of the IGS-TEC
maps*

B.2. Characteristic properties of planetary wave signatures in the ionosphere

The number of observed PWTO in the IGS maps is shown in Fig. B.3. The RMS amplitudes of the standing waves of different wavenumbers in the IGS-fj,TEC_{rell} filter are shown in Fig. B.4 and the RMS amplitudes for the travelling waves in Fig. B.5. The latitude dependence of the PWTO observed in the IGS maps is shown in Fig. B.6.

B.2. properties of PWTO in the ionosphere

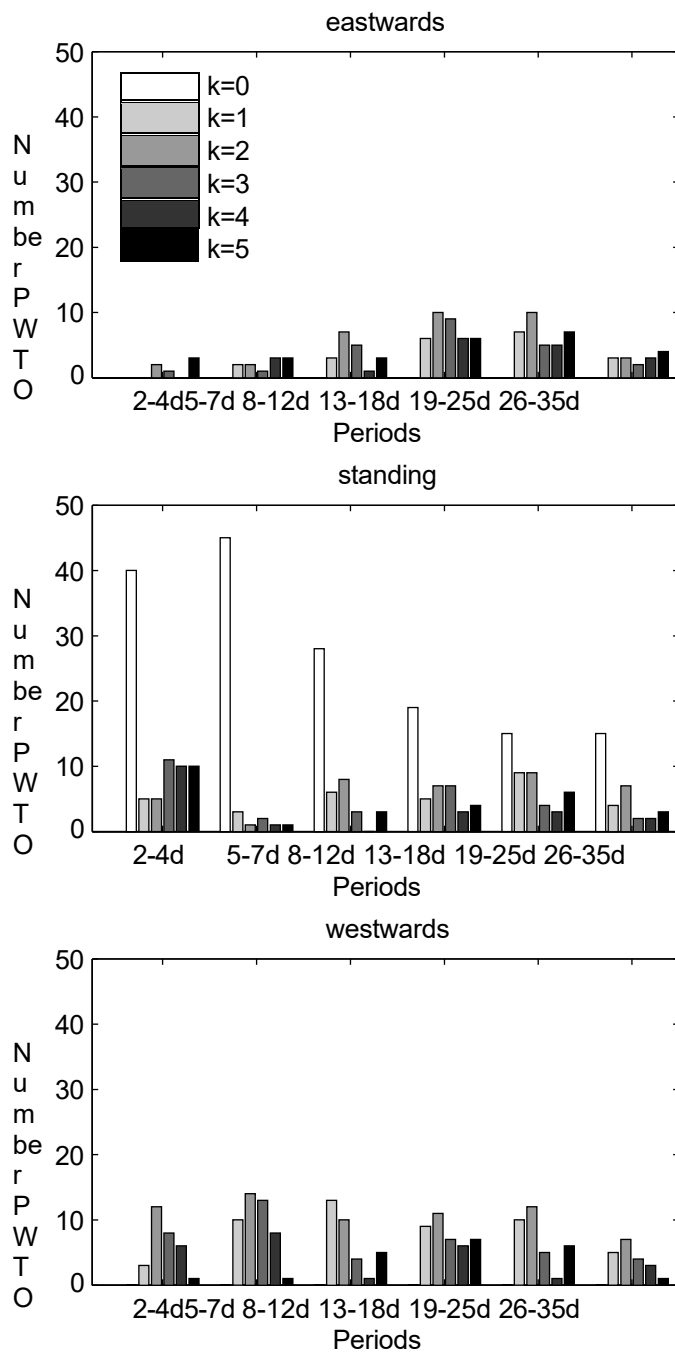


Figure B.3: Number of observed PWTO in IGS-fj, TEC_{rell} filter in 55° N, 2002-2008, differentiated by wave number and period class. Top: eastward migrating PWTO; middle: stationary PWTO; bottom: westward migrating PWTO. The grey values of the columns mark the wave number.

K

B. Analyses of the IGS-TEC maps

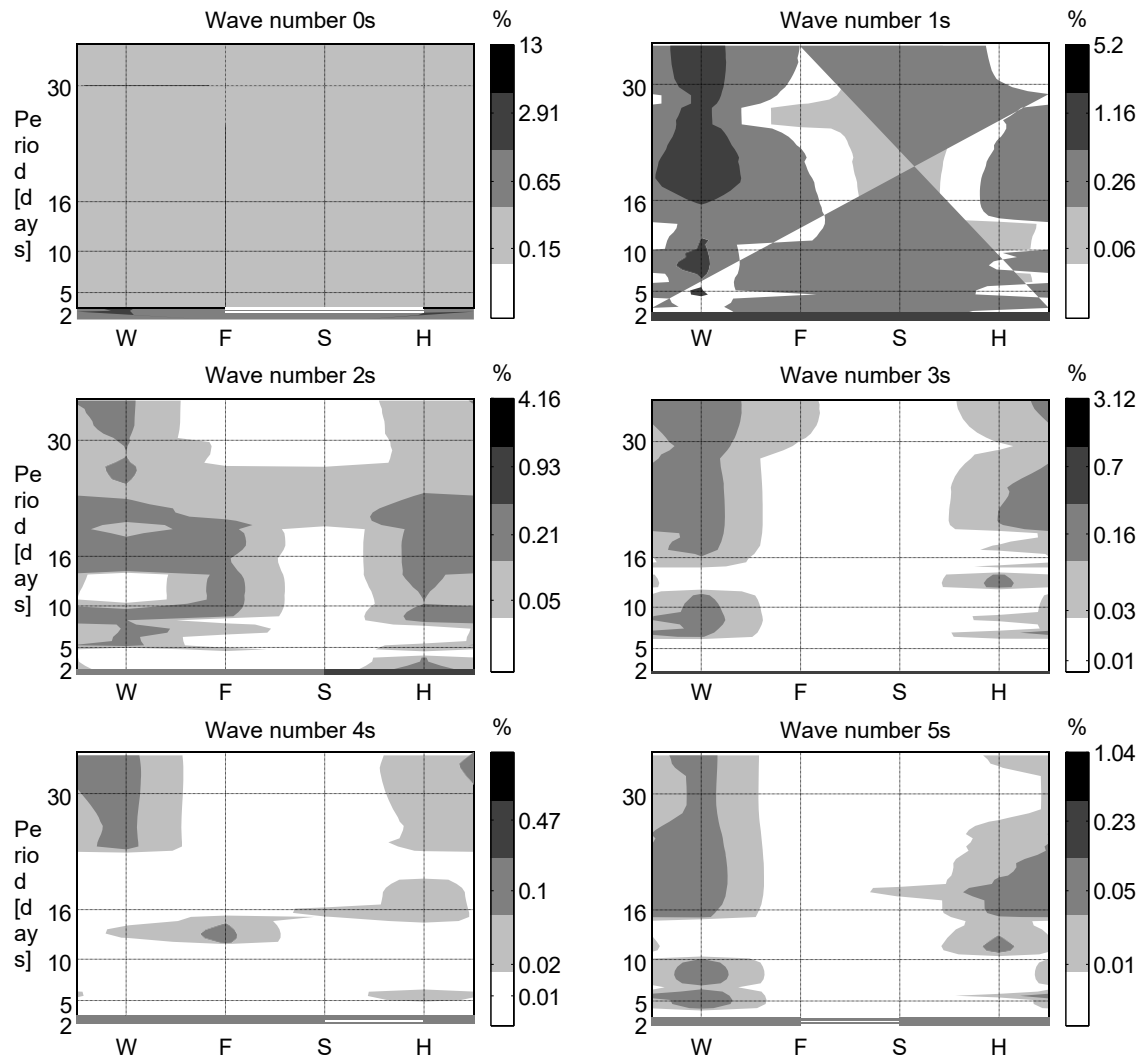


Figure B.4.: RMS of the amplitude of standing waves of different wave numbers on 55° N observed in the IGS-fj,TEC_{rell} filter (2002-2008) as a function of season (W: winter, F: spring, S: summer, H: autumn). The amplitude in % refers to the percentage deviation from the 27-day median.

B.2. properties of PWTO in the ionosphere

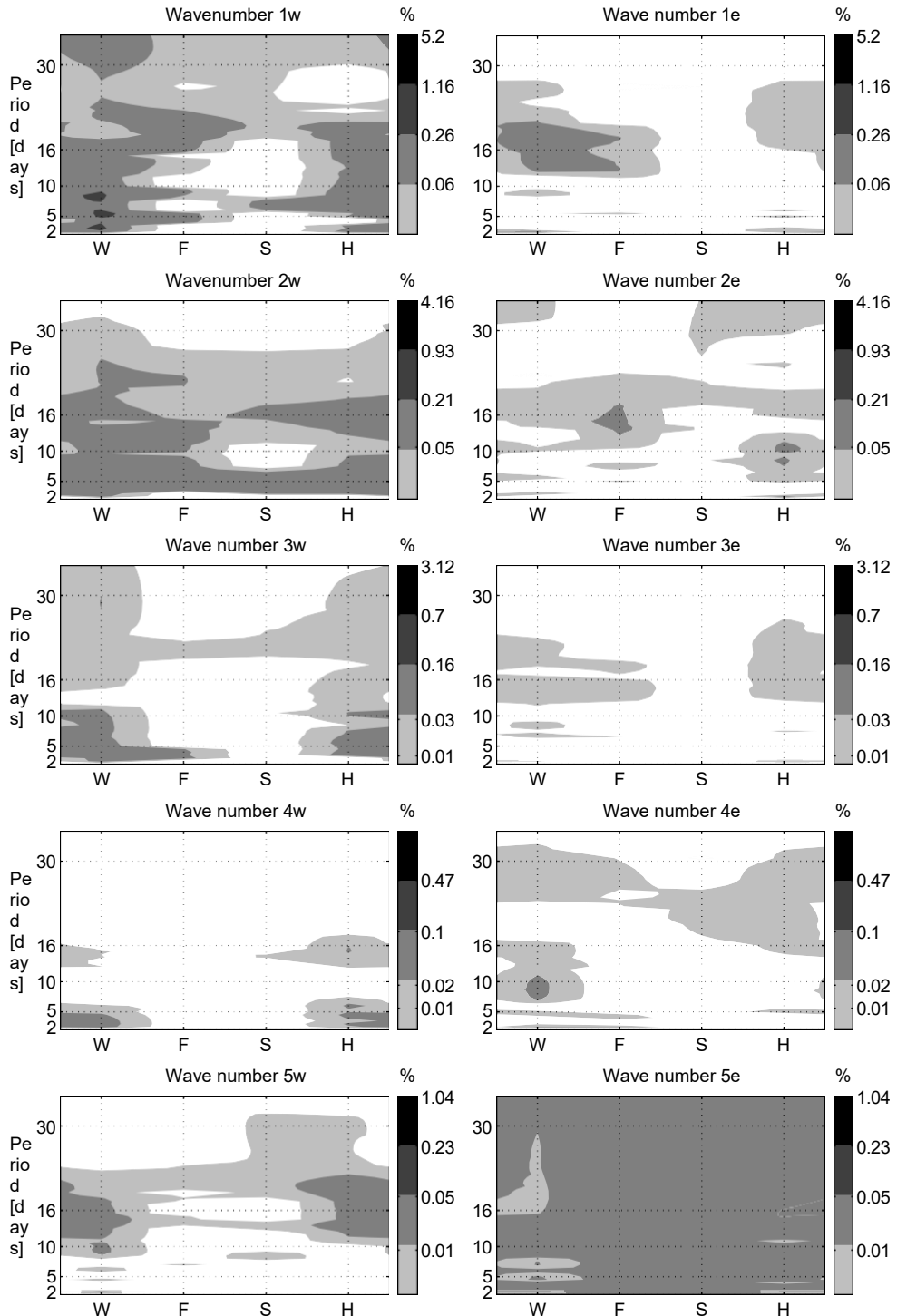


Figure B.5.: RMS of the amplitude of the travelling waves at 55° N observed in the IGS-fj,TEC_{rell} filter (2002-2008) during the different seasons.

M

B. Analyses of the IGS-TEC maps

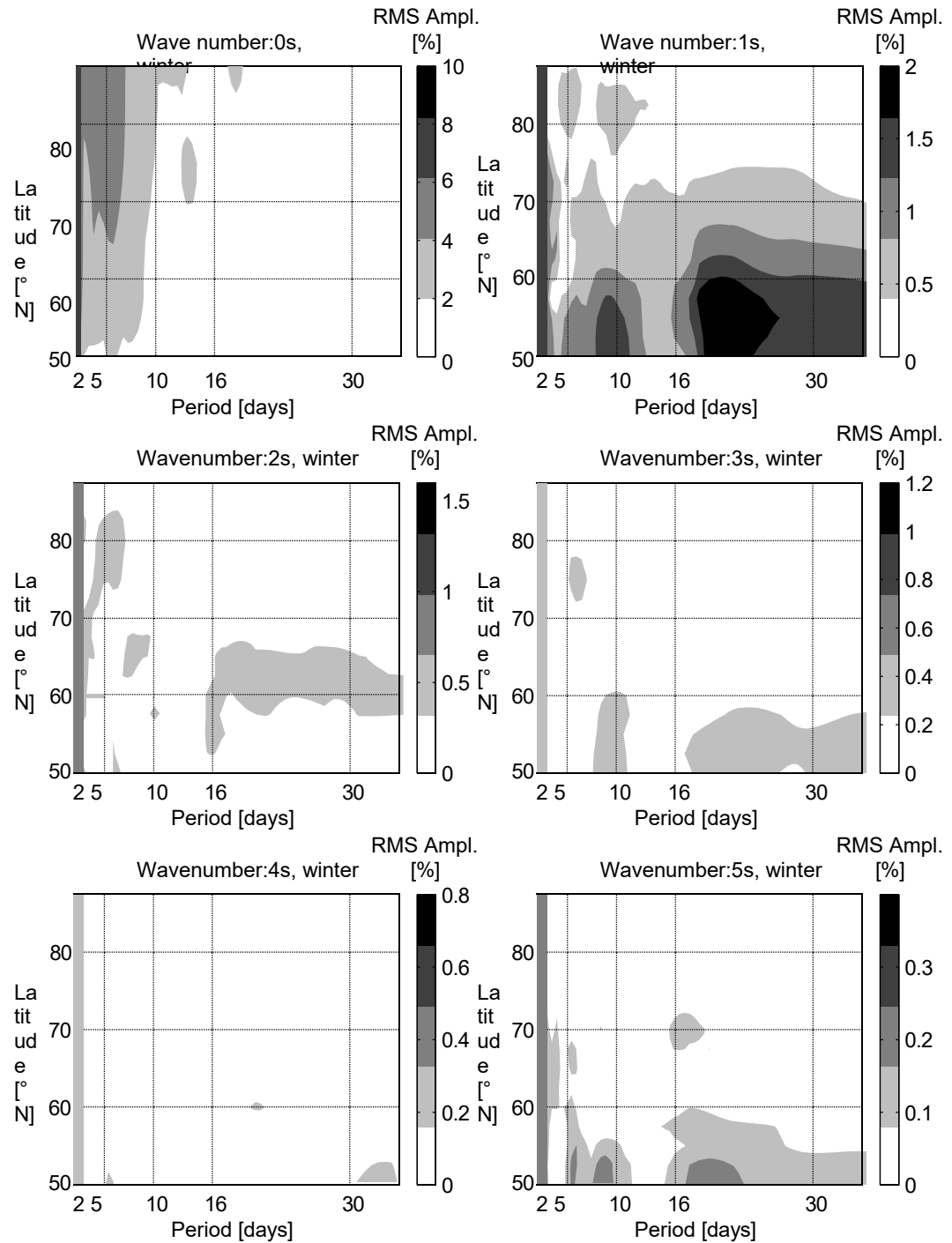


Figure B.6.: RMS amplitude of standing PWTO in the winter months December–February, 2002–2008, as a function of latitude.

N

B.2. connections to stratospheric PWs

B.3. Potential connections to stratospheric planetary waves

In this section, the number of simultaneously observed PWTO is shown in Fig. B.7, potential matches with type I secondary waves in Fig. B.8, with type III secondary waves in Fig. B.9 and with type IV secondary waves in Fig. B.10.

B. Analyses of the IGS-TEC maps

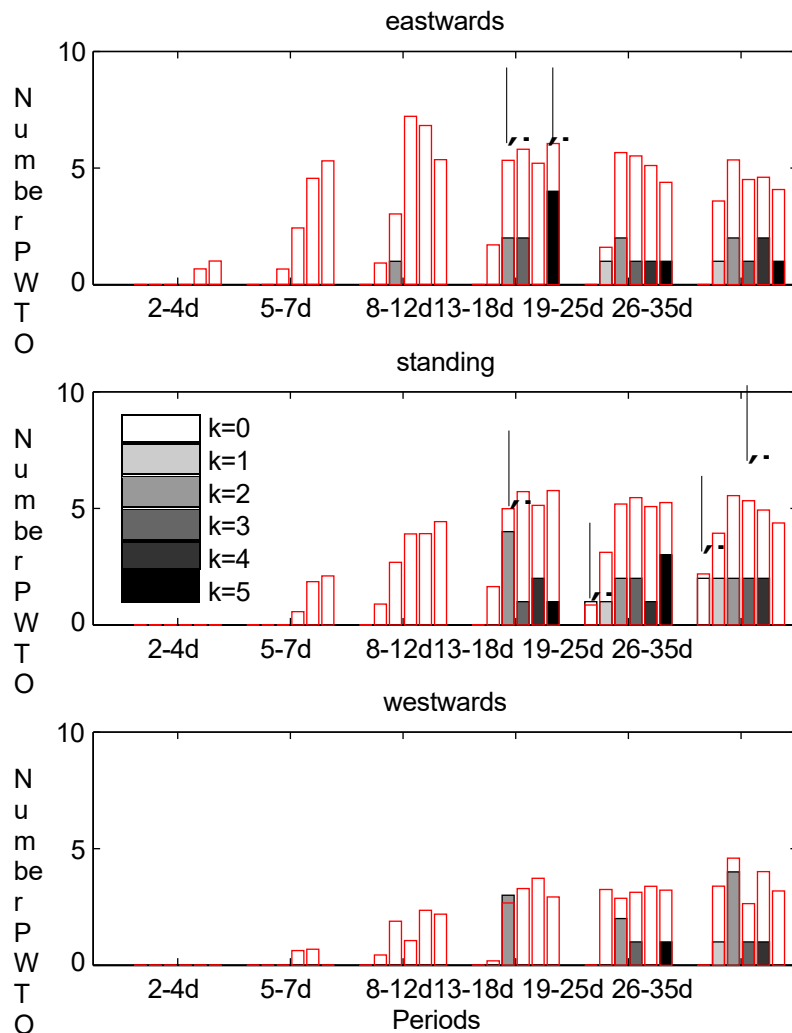


Figure B.7.: Number of simultaneously observed PW (NCEP zonal wind, 10hPa, 55° N) and PWTO (IGS-fj, TEC_{rell} filter 55° N). The grey shading of the bars indicates the wave number. Red bars indicate the 95% significance level. The arrows mark the significant wave classes of the DLR-fj, TEC_{rell} filter maps.

B.3. connections to stratospheric PWs

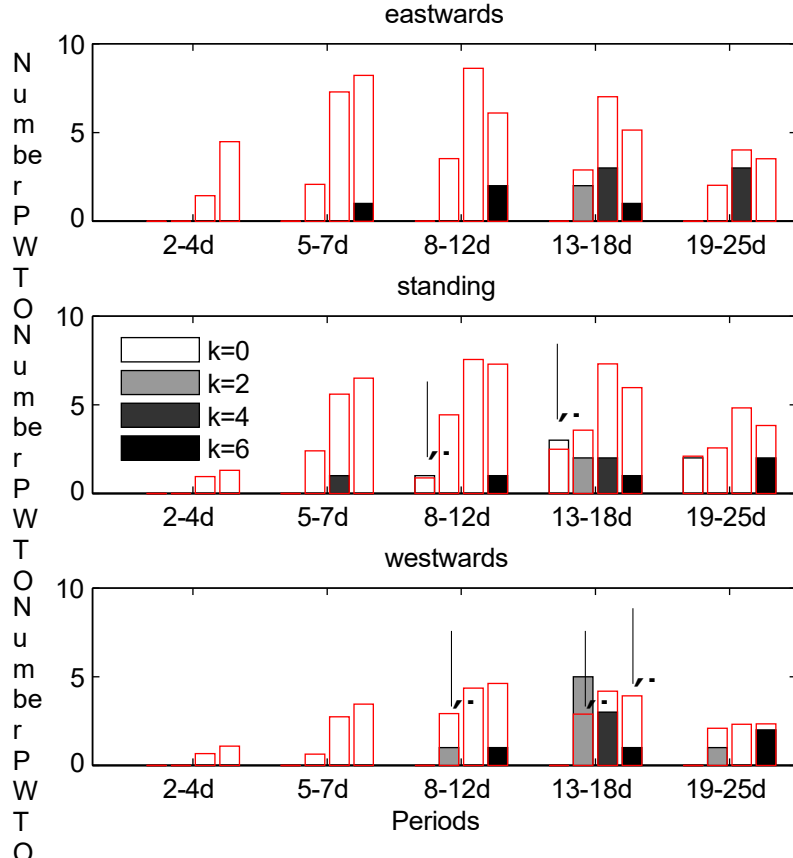


Figure B.8.: Number of simultaneously observed PWTO in IGS-fj,TEC_{rell} filter (55° N) and waves of secondary wave type I, which are theoretical result of non-linear interaction of PW and SPW (NCEP zonal wind, 10hPa, 55° N). The 95% significance level is marked with red bars. The arrows mark the significant wave classes of the DLR-fj,TEC_{rell} filter maps.

B. Analyses of the IGS-TEC maps

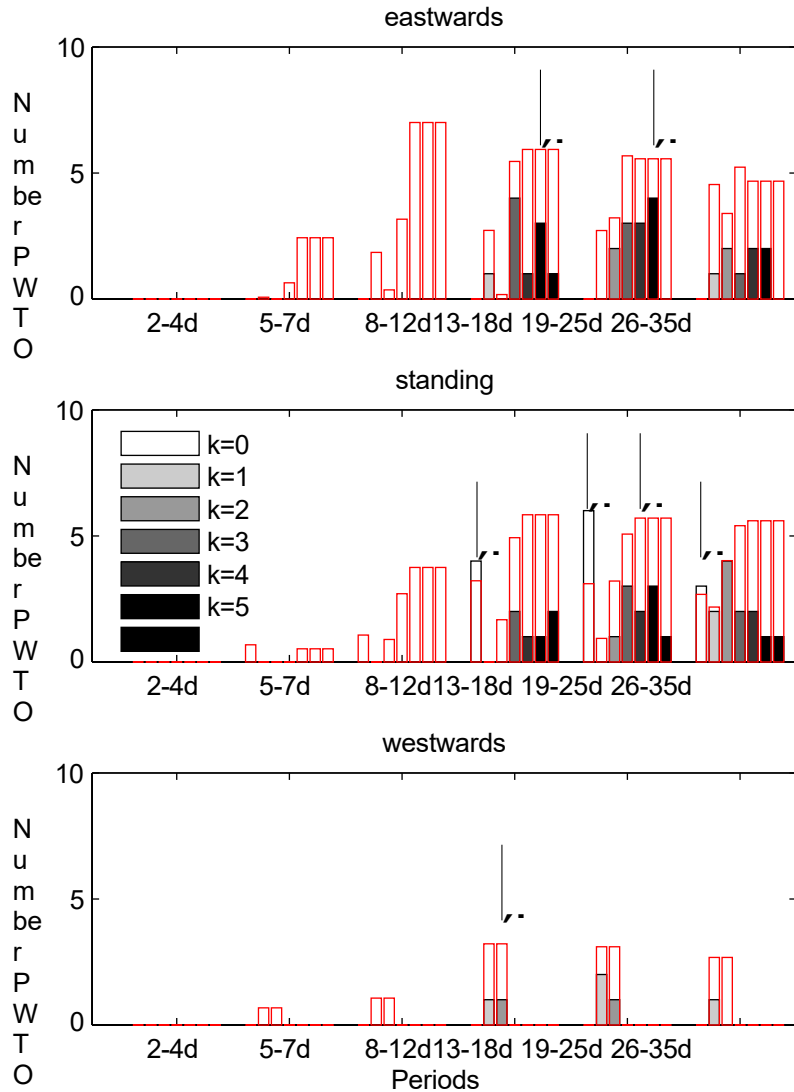


Figure B.9.: Number of simultaneously observed PWTO in IGS-fj,TEC_{rell} filter(55° N) and waves of secondary wave type III, which are theoretical result of non-linear interaction of PW and SPW (NCEP zonal wind, 10hPa, 55° N). The 95% significance level is marked with red bars. The arrows mark the significant wave classes of the DLR-fj,TEC_{rell} filter maps.

B.3. connections to stratospheric PWs

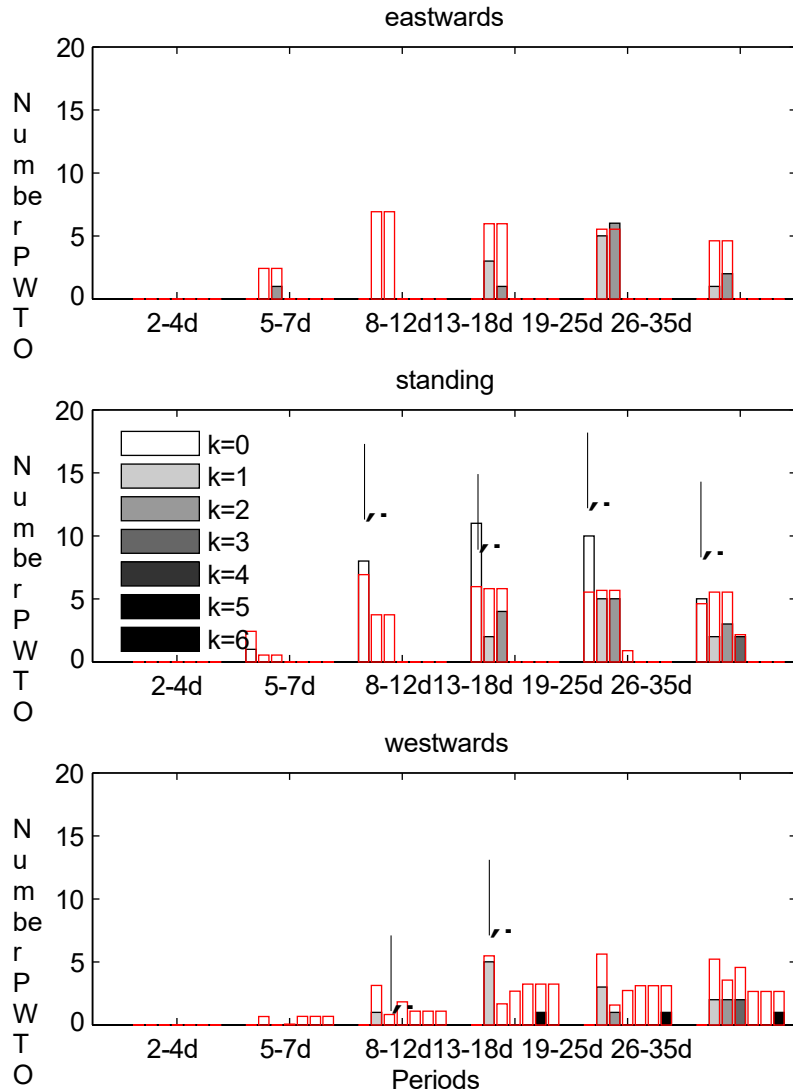


Figure B.10.: Number of simultaneously observed PWTO in IGS-fj,TEC_{rell} filter (55° N) and waves of secondary wave type IV, which are theoretical result of nonlinear interaction of PW and SPW (NCEP zonal wind, 10hPa, 55° N). The 95% significance level is marked with red bars. The arrows mark the significant world classes of the DLR-fj,TEC_{rell} filter maps.